Development and Application of Ferrihydrite-Modified Diatomite and Gypsum for Phosphorus Control in Lakes and Reservoirs

A Thesis Submitted to the

College of Graduate Studies and Research

In Partial Fulfillment of the Requirements

For the Degree of Doctor of Philosophy

In the Department of Civil and Geological Engineering

University of Saskatchewan

Saskatoon

By

Wenhui Xiong

Fall 2009

PERMISSION TO USE

In presenting this thesis in partial fulfillment of the requirements for a Postgraduate degree from the University of Saskatchewan, I agree that the Libraries of this University may make it freely available for inspection. I further agree that permission for copying of this thesis in any manner, in whole or in part, for scholarly purposes may be granted by the professor who supervised my thesis work or, in his absence, by the Head of the Department or the Dean of the College in which my thesis work was done. It is understood that any copying, publication, or use of this thesis or parts thereof for financial gain shall not be allowed without my written permission. It is also understood that due recognition shall be given to me and to the University of Saskatchewan in any scholarly use which may be made of any material in my thesis.

Requests for permission to copy or to make other use of material in this thesis in whole or part should be addressed to:

Head of the Department of Civil and Geological Engineering
University of Saskatchewan
Saskatoon, Saskatchewan

ABSTRACT

A novel phosphorus (P) adsorbent, ferrihydrite-modified diatomite (FHMD) was developed and characterized in this study. The FHMD was made through surface modification treatments, including NaOH treatment and ferrihydrite deposition on raw diatomite. In the NaOH treatment, surface SiO_2 was partially dissolved in the NaOH solution. The dissolved Si contributed to form stable 2-line ferrihydrite, which deposited into the larger mesopores and macropores of the diatomite. The 2-line ferrihydrite not only deposited into the pores of the diatomite but also aggregated on the surface. Filling the larger mesopores and macropores of the diatomite and aggregation on the diatomite surface with 0.24 g Fe/g of 2-line ferrihydrite resulted in a specific surface area of 211.1 m^2/g for the FHMD, which is an 8.5-fold increase over the raw diatomite (24.77 m^2/g). The surface modification also increased the point of zero charge (pH_{PZC}) values to 10 for the FHMD from 5.8 for the raw diatomite.

Effects of the formation process parameters such as concentrations of $FeCl_2$, NaOH, and drying temperature on the formation mechanism and crystalline characteristics of FHMD were studied by using X-ray absorption near-edge structure (XANES) spectroscopy. The spectra were recorded in both the total electron yield (TEY) and the fluorescence yield (FY) modes to investigate the chemical nature of Fe and Si on the surface and in the bulk of ferrihydrite-modified diatomite, respectively. It was found that only the surface SiO_2 was partially dissolved in the NaOH solution with stirring and heating, whereas the bulk of diatomite seemed to be preserved. The dissolved Si was incorporated into the structure of ferrihydrite to form the 2-line Si-containing ferrihydrite. The crystalline degree of ferrihydrite increased with the increasing $FeCl_2$ concentration and the Brunauer-Emmett-Teller (BET) specific surface area of FHMD decreased with the increasing $FeCl_2$ concentration. The NaOH solution of higher concentration partially dissolved more surface SiO_2 and the crystalline degree of ferrihydrite decreased with the increase in NaOH concentration. The dehydroxylation on the surface of FHMD occurred in the high temperature calcination, causing an

energy shift in the Si L-edge spectra to the high energy side and an increase in the crystalline degree of ferrihydrite. In this study, the optimal synthesis conditions for the FHMD with the least crystalline degree and the highest surface area were found to be as the follows: 100 mL of 0.5M $FeCl_2$ solution, 6M NaOH solution and the drying temperature of 50 ºC.

Phosphorus adsorption behavior and adsorption mechanism of FHMD were investigated in the research. The Langmuir model best described the P adsorption data for FHMD. Because of increased surface area and surface charge, the maximum adsorption capacity of FHMD at pH 4 and pH 8.5 was increased from 10.2 mg P/g and 1.7 mg P/g of raw diatomite to 37.3 mg P/g and 13.6 mg P/g, respectively. Phosphorus showed the best affinity of adsorption onto FHMD among common anions. K-edge P XANES spectra demonstrate that P is not precipitated with Fe (III) of FHMD, but adsorbed on the surface layer of FHMD.

Phosphorus removal from lake water and limiting phosphorus release from sediment by FHMD was examined. Phosphorus removal from lake water proceeded primarily through P adsorption onto the surface of FHMD. When a dose of FHMD of 250 mg/L was applied to lake water, a total phosphorus (TP) removal efficiency of 88% was achieved and a residual TP concentration was 17.0 µg/L which falls within the oligotrophic TP range (3.0-17.7 µg/L). FHMD settled down to the bottom of the 43 cm high cylinder within 6 hours, which suggested that retention time of FHMD in the 5.5 m of Jackfish lake water column was close to the equilibrium time of P adsorption onto FHMD (72 hours). During the 30-day anoxic incubation period, TP concentrations in lake water treated by 400, 500 and 600 mg/L of FHMD showed a slight decrease and maximum TP concentrations remained at levels lower than 15 µg/L. The addition of FHMD resulted in a marked increase in Fe-P fraction, a pronounced decrease in labile-P and organic-P fractions, and stable Al-P, Ca-P and residual-P fractions. The effect of FHMD on limiting P release was comparable with those of the combination of FHMD and alum solutions with logarithmic ratios of Al to mobile P of 0.5 and 0.8. FHMD not

only can effectively remove P from lake water but also keep a strong P-binding capacity under anoxic conditions and competition for P with alum at high amounts.

The role of gypsum on stabilizing sediment and the optimum dose of gypsum were investigated. The effectiveness of gypsum in stabilizing sediment was proved by the fact that at the same agitation speed, turbidities and soluble reactive P (SRP) concentrations of samples treated with gypsum were much lower than those of sample without gypsum. The optimal thickness of the gypsum layer was found to be 0.8 cm.

Combined application of FHMD and gypsum to P control was investigated in the research. It was found in the 30-day incubation of lake water and sediment treated by FHMD and gypsum that no P release seemed to occur regardless of oxic or anoxic conditions. In order to investigate the 120-day effects of FHMD and gypsum on the P control under anoxic and agitation conditions a lab-scale artificial aquarium was established in an environmental chamber. Daily oscillation of a metal grid did not yield the sediment resuspension due to the gypsum stabilization. The combined application of FHMD and gypsum resulted in a 1 g/L increase in the SO_4^{2-} concentration in the 120-day aquarium compared with that in the control aquarium; however it did not affect the total kjeldahl nitrogen (TKN) concentrations in both the control aquarium and the 120-day aquarium. The addition of FHMD and gypsum enhanced total alkalinity in the 120-day aquarium, thereby improving buffering capacity of lake water. Under anoxic conditions and sediment resuspension conditions, relative to a large increase in total P (TP) concentrations in the control aquarium, TP concentrations in the 120-day aquarium stayed relatively stable, fluctuating within the range of 9.1-13.3 µg/L. Relative to control sediment, Fe-P was significantly enhanced during the 60-day incubation; however, Fe-P did not appear to increase significantly in the second 60-day incubation. Labile-P and organic-P decreased with sediment depths in both control aquarium and test aquariums; however, Al-P, Ca-P and residue-P increased with sediment depth. Lower Al-P is observed in treatment aquariums than in control sediment.

As an effective P adsorbent, FHMD showed a high adsorption capacity as well as a significantly higher affinity for P than other anions. A combined application of FHMD and gypsum effectively reduced sediment resuspension and maintained TP levels within the oligotrophic range under anoxic conditions in the laboratory-scale artificial aquarium.

ACKNOWLEDGEMENTS

I am very grateful to my supervisor, Dr. Jian Peng, for his valuable guidance, support, and other assistance throughout the course of this research work and the completion of this thesis document.

I wish to thank my Advisory Committee members, Dr. Douglas Milne, Dr. Gordon Putz, Dr. Jim Kells, and Dr. Jeff Hudson for their suggestions and assistance during the research work. I also would like to thank the Environmental Engineering Laboratory technologist Mr. Doug Fisher who assisted me in collecting the water and sediment sample and assembling experimental apparatuses.

I also wish to acknowledge the financial support provided by the Natural Sciences and Engineering Research Council of Canada through my supervisor's NSERC grant, as well as the financial support provided by the Department of Civil and Geological Engineering at the University of Saskatchewan.

Finally, I thank my parents for their patience and support while I endeavoured to complete my Ph.D. program. I owe the most to my beloved wife, Yin Kuang and my lovely daughters, Suki Xiong and Sonia Xiong, who accompanied me through all the frustration and struggles of my research.

TABLE OF CONTENTS

LIST OF TABLES

LIST OF FIGURES

LIST OF ABBREVIATIONS AND SYMBOLS

ADP	Adenosine diphosphate
APA	Alkaline phosphatase activity
ATP	Adenosine triphosphate
BD	Bicarbonate dithionite
BET	Brunauer-Emmett-Teller
C_A	Concentrations of acid needed to reach a point on the titration curve
C_A	Concentrations of base needed to reach a point on the titration curve
CCP	Critical concentration of phosphorus required for maximum growth of algae
C_e	Unadsorbed phosphorus concentration at equilbrium
C_0	The initial phosphate concentrations
CLS	Canadian Light Source
DIP	Dissolved inorganic phosphorus
DNA	Deoxyribonucleic acid
DO	Dissolved oxygen
DOP	Dissolved organic phosphorus
$dV/d(\log D)$	Differential pore size distribution
Eh	Redox potential
EPBR	Enhanced biological phosphate removal
F	Faraday constant
FDA	Food and Drug Administration
$FeCl_2.4H_2O$	Ferrous chloride
Fe_2O_3	Anhydrous ferric oxide
$FePO_4.2H_2O$	Synthetic hydrate iron phosphate
FHMD	Ferrihydrite-modified diatomite
0.5-FHMD	Ferrihydrite-modified diatomite produced at 0.5 M $FeCl_2$ and 6 M NaOH and dried at 50 °C
1-FHMD	Ferrihydrite-modified diatomite produced at 1 M $FeCl_2$ and 6 M NaOH and dried at 50 °C

1FHMD-300	1-FHMD calcined at 300 °C
1FHMD-500	1-FHMD calcined at 500 °C
1FHMD-900	1-FHMD calcined at 900 °C
1.5-FHMD	Ferrihydrite-modified diatomite produced at 1.5 M $FeCl_2$ and 6 M NaOH and dried at 50 °C
2-FHMD	Ferrihydrite-modified diatomite produced at 2 M $FeCl_2$ and 6 M NaOH and dried at 50 °C
2.5-FHMD	Ferrihydrite-modified diatomite produced at 2.5 M $FeCl_2$ and 6 M NaOH and dried at 50 °C
FN6	Brand name of unprocessed diatomite
FTIR	Fourier transform infrared
FY	Fluorescence yield
H_2SiO_3	Silicic acid
H_4SiO_4	Silicic acid
IUPAC	International Union of Pure and Applied Chemistry
K_F	Freundlich constant
K_L	Langmuir equilibrium constant
K_2HPO_4	Potassium phosphate dibasic
l	Azimuthal quantum number
LUP	Luxury uptake phosphorus
MCP	Microchannel plate
Me	Metal cations
$MnCl_2$	Manganese (II) chloride
MnO_2	Manganese oxide
MO	Molecular orbital
MS	Multiple scattering
NRP	Non-reactive phosphorus
3NaOH-FHMD	Ferrihydrite-modified diatomite produced through 3 M NaOH and 1 M $FeCl_2$ and dried at 50°C
4NaOH-FHMD	Ferrihydrite-modified diatomite produced through 4 M NaOH and 1

	M $FeCl_2$ and dried at 50°C
5NaOH-FHMD	Ferrihydrite-modified diatomite produced through 5 M NaOH and 1 M $FeCl_2$ and dried at 50°C
6NaOH-FHMD	Ferrihydrite-modified diatomite produced through 6 M NaOH and 1 M $FeCl_2$ and dried at 50°C
pH_{PZC}	pH values at the point of zero charge
PGM	Plane grating monochromator
Q_0	Theoretical monolayer saturation capacity
q_e	The amount of adsorbed phosphate ions on the adsorbents at equilibrium
Q_e	The amount of adsorbed phosphorus per unit weight of adsorbent at equilibrium
R_L	Dimensional equilibrium parameter
RNA	Ribonucleic acid
SAV	Submerged aquatic vegetation
SEM	Scanning electron microscope
SGM	Spherical grating monochromator
SR	Sedimentation rate
SRP	Soluble reactive phosphorus
TDP	Total dissolved phosphorus
TEM	Transmission electron microscope
TEY	Total electron yield
TKN	Total kjeldahl nitrogen
TP	Total phosphorus
TPP	Total particulate phosphorus
TSS	Total suspended solids
VLS-PGM	Variable line spacing-plane grating monochromator
XANES	X-ray absorption near-edge structure spectroscopy
XRD	X-ray diffraction

Chapter 1 – Introduction

1.1 Background

Eutrophication is a process by which excessive addition of inorganic nutrients and organic matter to a lake leads to an increase in biological production. Blooms of large colony-forming cyanobacteria often dominate the plankton population in eutrophic lakes with characteristics such as limited shading, poor circulation, high nutrient loading, and low abundance of macrophytes and some zooplankton (Hart et al. 2003). Cyanobacterial blooms are a serious environmental problem because they can produce natural poisons, kill other aquatic species, make people and animals sick, impair the drinking water supply, and make recreational areas unpleasant (Thomann and Mueller 1987).

Phosphorus (P) is a major limiting nutrient for the growth of phytoplankton including cyanobacteria (Ring and Rast 1989). The composition of organic matter in the phytoplankton is approximated by $C_{106}H_{263}O_{110}N_{16}P_1$ (Wang et al. 2003). The carbon (C), hydrogen (H), and oxygen (O) are abundant and readily available, but nitrogen (N) and phosphorus (P) are generally limited in the environment (Scarlatos 1997). In most temperate lakes, phosphorus controls the process of eutrophication (Thomann and Mueller 1987). High P concentrations yield cloudy lakes and oxygen may be severely depleted or eliminated from the deep, cold hypolimnetic water in the summer months. Maintaining the P content of lakes at low levels can limit cyanobacterial blooms and control eutrophication.

Fundamentally, the P content of lakes can be controlled by reducing the mass flow of P from the drainage basin (Ring and Rast 1989). The isolation of lakes from external P

sources can result in a gradual decrease of in-lake P levels (Ring and Rast 1989). However, even in cases where measures to control external P sources have been successful, recovery of eutrophic lakes may still be delayed by high P concentrations in the lake waters and the continuous release of P from sediments (Hansen et al. 2003; Salonen and Varjo 2000). Moreover, the low P input necessary for recovery often cannot be achieved due to the high costs involved to reduce point sources and non-point sources of P. Under these circumstances, in-lake P control methods provide a possibility for eutrophication control (Ryding and Rast 1989). In-lake P control involves the removal of P from the water column and the inhibition of P release from lake sediments.

Precipitation of phosphorus with aluminium and ferric salts can effectively remove P from the water column and limit P release from lake sediments (Cooke et al. 2005). However, aluminium and ferric salts can be ecologically harmful to the aquatic species in lakes (Hullebusch et al. 2002). Thus, finding a material which is not only effective in removing P and limiting P release from sediment but is also ecologically safe and cost effective is the key for successful application of an in-lake P control process.

In the research, a novel, ecological safe and cost effective material, ferrihydrite-modified diatomite (FHMD) is developed to control eutrophication through removing P from lake water and limiting P release from sediment.

1.2 Research Objectives

The objectives of this research were:

- To develop an effective and ecologically safe material, specifically a ferrihydrite-modified diatomite (FHMD), to remove phosphorus from lake water and limit phosphorus release from sediments.

- To determine the optimum formation conditions for ferrihydrite-modified diatomite by using X-ray absorption near-edge structure spectroscopy (XANES).

- To study the phosphorus adsorption behaviour and phosphorus adsorption mechanism of ferrihydrite-modified diatomite.

- To investigate in batch scale the ability of (1) ferrihydrite-modified diatomite to bind phosphorus under anoxic conditions, and (2) the combined application of ferrihydrite-modified diatomite and gypsum to limit phosphorus release and inhibit sediment resuspension.

- To evaluate the short term (120 days) effects of the combined application of ferrihydrite-modified diatomite and gypsum on phosphorus removal from water and limiting phosphorus release from sediment in a laboratory-scale artificial aquarium.

1.3 Scope of Research

The scope of this research was limited as follows. Mechanisms of P removal from the water column and inactivation of P within lake sediments by ferrihydrite-modified diatomite (FHMD) and limiting sediment resuspension with gypsum were qualitatively investigated. *In situ* applications of FHMD and gypsum, such as enclosure experiments and whole-lake experiments, were not included.

An evaluation of the effectiveness of P removal and sediment sealing in a laboratory-scale artificial aquarium were conducted. To avoid the influence of changes in environmental conditions on growth of algae and aquatic plants, the ambient temperature and daily light period were held constant. Additionally, the aquariums had no inflow, and thus simulate environmental conditions in a lake where external nutrient sources have been eliminated.

A novel P adsorbent, FHMD, was developed and characterized. A new method to integrate P coprecipitation with biological diatom P uptake was used for removal of P from lake water. A new combination of FHMD and gypsum was employed to inactivate P in sediments and limit sediment resuspension.

1.4 Organization of Thesis

Chapter 2 presents a literature review of lake eutrophication and current eutrophication control processes, as well as chemical characteristics of phosphorus, diatomite, ferrihydrite, and gypsum. This chapter also provides insight into phosphorus adsorption behaviour and adsorption mechanisms, and briefly describes X-ray absorption near-edge structure (XANES) spectroscopy.

Chapter 3 presents the conceptual development of FHMD, including a theoretical formation mechanism.

Chapter 4 presents a detailed description of the preparation of FHMD and reference materials, experiments, and analytical methods used to fulfill the research objectives.

Chapter 5 presents and discusses the results of the experiments. The results principally include development and characterization of FHMD as an effective P adsorbent, optimized synthesis conditions for FHMD, the P adsorption behaviour of FHMD, P removal from lake water by FHMD, inactivation of P within sediments by FHMD, reduced sediment suspension by gypsum, and combined applications of FHMD and gypsum in a laboratory-scale artificial aquarium.

Chapter 6 presents conclusions derived from this study and some recommendations for future work.

Chapter 2 - Literature Review

2.1 Lakes

2.1.1 Lakes and Reservoirs

A lake is a natural body of water (usually freshwater) of considerable size contained within a land mass. In contrast, a reservoir is a man-made waterbody (even though many reservoirs are called lakes) (Ryding and Rast 1989). Reservoirs are usually formed by the construction of a dam across a river or stream, resulting in impoundment of the water behind the dam structure (Cooke et al. 2005). Reservoirs generally have larger drainage basins, surface areas, and drainage basin to surface area ratios than lakes (Wetzel 2001). The mean and maximum depths of reservoirs are usually greater than lakes (Ryding and Rast 1989). Reservoirs also have greater areal water loads (water flow through unit area of a lake) and shorter hydraulic residence times (Ryding and Rast 1989). With regard to developing an effective eutrophication control program, these differences are insignificant (Cooke et al. 1986). Lakes and reservoirs have many similarities in terms of basic biological and some physical processes. Thus, it is expected that aspects of the eutrophication process will be fundamentally the same in these two types of water bodies and that some basic understandings gained in one water body can be transferred to the other (Ryding and Rast 1989).

2.1.2 Deep and Shallow Lakes

In temperate regions, many deep lakes (mean depth > 10 m) exhibit thermal stratification (Horne and Goldman 1994). During summer months, the surface waters are heated by solar radiation into an upper warm, less dense, well-mixed water layer termed the epilimnion (Kalff 2002). Below the epilimnion is the metalimnion, a zone of rapidly changing water temperature and density with depth, followed by the

hypolimnion, a deep, colder, denser, and often dark bottom layer (Horne and Goldman 1994). The characteristics of the different stratification layers are shown in Figure 2.1.

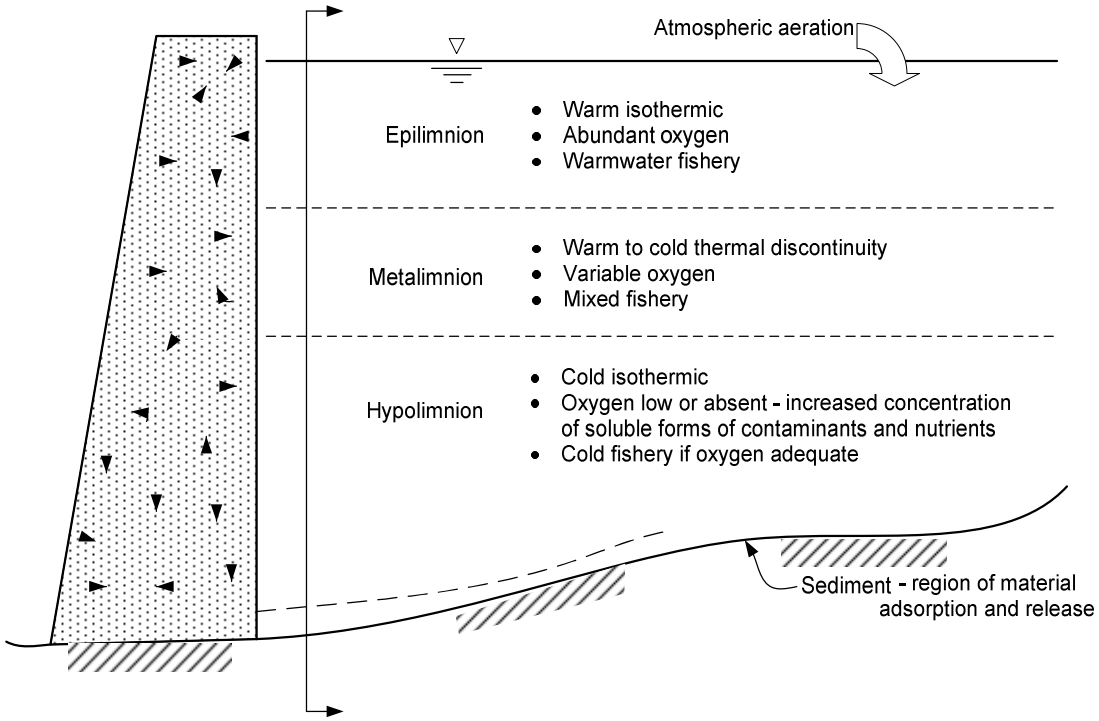

Figure 2.1 Location and characteristics of the epilimnion, metalimnion, and hypolimnion (from Cooke et al. 2005)

The hypolimnion typically has low dissolved oxygen content (Chang 1989). High microbial respiratory activity and decomposition of organic matter consume dissolved oxygen and create anoxic conditions. The anoxia in the hypolimnion results in intensive phosphorus (P) release from anoxic sediments. When the lake or reservoir is thermally stratified (summer/winter), the metalimnion acts as a barrier to the exchange of nutrients between the hypolimnion and epilimnion (Wetzel 2001). Thus, P released from sediments does not contribute greatly to primary production in the epilimnion. In contrast, P delivered from external sources generally enters via the epilimnion and stimulates primary production near the surface (Wetzel 2001).

In autumn when less solar radiation reaches the water and greater heat losses occur at night, convection and wind mixing begin to weaken the metalimnion (Kalff 2002). The epilimnion increases in depth as the temperature decreases. Eventually, the difference in temperature and density between the overlying water and that beneath diminishes to the point that a strong wind can overcome the remaining resistance to mixing and the lake undergoes fall overturn (Horne and Goldman 1994). In the winter, inverse stratification occurs when water is colder than 3.94 ºC—the temperature at which water reaches its maximum density—floats above a slightly warmer layer at depth (Horne and Goldman 1994). In spring, when lakes become ice-free and surface waters begin to warm, the water throughout the lake becomes of uniform temperature and density, resulting in the spring overturns (Kalff 2002).

Shallow lakes (mean depth < 3 m) are more common than larger, deeper ones (Kalff 2002). Shallow lakes display a number of characteristics that set them apart from the more often-studied deeper lakes. These include: (1) a low oxygen storage capacity (Ruloy and Rusch 2004); (2) a lack of stable long-term thermal stratification mainly due to frequent wind-driven advections (Cooke et al. 1986); (3) frequent mixing of the entire water column and resuspension of unconsolidated sediments (Cooke et al. 1986); (4) substantial internal loading of nutrients from the sediments affecting the entire water column (Nürnberg 1984); and (5) less sensitivity to significant reduction in external nutrient loading (Cooke et al. 2005). Due to these factors, many shallow lakes are eutrophic. Calm, warm weather conditions can produce short-lasting thermal stratification conditions that are easily disrupted by wind action. However, dissolved oxygen (DO) in shallow lakes with low oxygen storage capacity may be rapidly depleted by microbial activity during these short-term stratifications, and phosphorus (P) in the sediment can be released into the overlying water. The subsequent breakdown of stratification by wind action then circulates P to the upper water, thereby promoting primary production (Cooke et al. 1986).

2.1.3 Seasonal Succession of Diatom and Cyanobacteria

Deep lakes exhibit an annual minimum phytoplankton active biomass in the winter or early spring as only a small amount of solar radiation reaches the water surface and is further reduced by ice and snow cover (Wetzel 2001). In the spring, rising levels of solar energy and water temperature allow increased rates of photosynthesis and phytoplankton growth (Kalff 2002). Large diatoms are favoured under conditions of spring weather and are the dominant phytoplankton species (Wetzel 2001). In late spring and early summer, a combination of higher temperature and abundant food supply allows the increased growth rate of herbivorous macrozooplankton that graze on diatoms, bringing about a decline in the diatom population. Moreover, the onset of stable thermal stratification brings about increased losses of large diatoms through sedimentation and a reduction in diatom growth rate as silica (a key limiting macronutrient for diatom growth) in the epilimnion becomes exhausted (Kalff 2002). This period, when diatom sedimentation results in low nutrient concentrations and water turbidity decreases, is known as the clear-water phase (Horne and Goldman 1994).

Cyanobacteria start their growth in the summer in response to the low nutrient concentrations in the clear-water phase (Kalff 2002). Cyanobacteria are able to fix nitrogen, and are dominant in lakes with disproportionately low nitrogen concentrations (Kagalou et al. 2003). Filamentous cyanobacteria gain a competitive advantage through luxury P uptake at the nutrient-rich sediment/water interface (Ruloy and Rusch 2004). After luxury P uptake from sediment reserves, filamentous cyanobacteria migrate to the lake surface to photosynthesize (Ruloy and Rusch 2004). Zooplankton are unable to consume cyanobacteria due to the tiny size and toxicity of cyanobacteria. Thus, due to low losses to predators and a high growth rate, the summer months are accompanied by a shift in the dominant species from diatoms to cyanobacteria (Kagalou et al. 2003). In the autumn, diatoms become dominant in deep lakes because they are favoured under conditions of fall weather and fall overturn. In some eutrophic lakes, cyanobacteria can remain dominant in the autumn (Cooke et al 2005).

2.2 Eutrophication

All lakes and reservoirs have a finite life span, and eventually will be filled with sediment and replaced by swamp, meadow, and forests (Harper 1992). This progression normally takes thousands of years, depending on the initial conditions of the area. However, humans, through their various activities, have greatly accelerated this process in thousands of lakes around the globe (Peters and Meybeck 2000). Lake eutrophication is therefore both a natural and culturally-based phenomenon.

2.2.1 Natural Eutrophication

Natural eutrophication is the process by which lakes and reservoirs gradually age and become more productive (i.e., more production of biomass). Succession of natural eutrophication is a term used to describe the change as lakes age from young (oligotrophic) to middle aged (mesotrophic) to old (eutrophic). As shown in Table 2.1, oligotrophic lakes typically have low levels of nutrients and correspondingly low levels of biological activity; eutrophic lakes have high levels of nutrients and correspondingly high levels of biological activity (Wetzel 2001). The natural time scale for the aging of a lake from oligotrophic to eutrophic is on the order of thousands of years. Natural eutrophication is a slow, largely irreversible process associated with the gradual accumulation of organic matter and sediments in lake basins.

2.2.2 Cultural Eutrophication

Cultural eutrophication is the process that accelerates the natural eutrophication due to human activities. Approximately 3% of the land on the earth is currently covered with human dwellings and commercial structures (Peters and Meybeck 2000). Human settlement, associated land clearing, and the development of farms and cities often change the natural eutrophication process in a dramatic way (Ryding and Rast 1989). Human activities directly influence the eutrophication process by altering the physical, chemical, and biological characteristics of lakes (Peters and Meybeck 2000). Human activities such as urbanization, transportation, irrigated farming, deforestation and

forestation, land drainage, channelization and damming, and mining change the physical characteristics of lakes by modifying the materials with which the water interacts. Chemical alterations associated with human activity occur mainly through the addition of wastes, especially nutrients (primarily phosphorus, nitrogen, and carbon) and other substances to the lake (Peters and Meybeck 2000). Excessive input of nutrients to lakes can result from discharge of effluent as well as runoff and leaching from agricultural land use within the lake's catchment (Peters and Meybeck 2000). The trophic state of a lake is largely determined by the amount of nutrients entering from the catchment. Biological alterations associated with human activity include forest management, agriculture, and the import of exotic species.

Thus, cultural eutrophication is an often rapid, possibly reversible process of nutrient enrichment and high biomass production stimulated by human activities causing nutrient transport to lakes (Cooke et al. 2005). Eutrophication or hypereutrophication often causes an increase in the occurrence of cyanobacteria blooms, reduced abundance of submerged macrophytes, the dominance of plankti-benthivorous fish (i.e, perch), and low water clarity (Anderson et al. 2005). Cyanobacteria blooms are a serious environmental problem because they produce natural poisons, can kill other aquatic species, can make people and animals sick, impair the drinking water supply and make recreational areas unpleasant (Thomann and Mueller 1987).

2.2.3 Trophic States

The trophic classification of lakes results from the division of a trophic continuum into a series of categories called trophic states (Wetzel 2001). The principal trophic states are oligotrophy, mesotrophy, and eutrophy (Wetzel 2001). Oligotrophic lakes are typically deep with relatively high levels of dissolved oxygen throughout the year, bottom sediments that typically contain small amounts of organic matter, good water quality, and moderately productive and diverse aquatic populations. Mesotrophic lakes are characterized by intermediate levels of biological productivity and diversity, slightly reduced dissolved oxygen levels, and water quality that is generally adequate to support

designated uses. Lakes classified as eutrophic typically exhibit high levels of organic matter, both suspended in the water column and in the upper portions of sediments. Biological productivity is high, often indicated by seasonal algae blooms and excessive plant growth (Wetzel 2001). Dissolved oxygen concentrations are low, and may reach extreme levels during critical periods. In addition, water quality is often so poor that specific uses are restricted. The trophic state of some highly polluted lakes has been termed "hypereutrophic" (Barica and Mur 1980). Table 2.1 illustrates typical water quality parameters of the three major trophic designations.

Table 2.1 General trophic classification of lakes and reservoirs in relation to typical water quality parameters (adapted from Wetzel 2001)

Parameter	Oligotrophic	Mesotrophic	Eutrophic	Hypereutrophic
Total phosphorus (µg/L)				
Mean	8.0	26.7	84.4	-
Range	3.0-17.7	10.9-95.6	16-386	750-1200
Total nitrogen (µg/L)				
Mean	661	753	1875	-
Range	307-1630	361-1387	393-6100	-
Chlorophyll *a* (µg/L)				
Mean	1.7	4.7	14.3	-
Range	0.3-4.5	3-11	3-78	100-150
Secchi transparency depth (m)				
Mean	9.9	4.2	2.45	-
Range	5.4-28.3	1.5-8.1	0.8-7.0	0.4-0.5

Given that trophic state is primarily a description of the biological condition of a lake, eutrophication can be described as the transition from oligotrophy to eutrophy (Wetzel

2001). The reverse process is termed oligotrophication, i.e., the process of a lake moving in the alternate direction towards oligotrophy. In lake management practices, oligotrophication can be achieved by a reduction in nutrient loading (Van Der Molen et al. 1998). However, a hysteresis effect may be observed during the process of oligotrophication because several buffer mechanisms (i.e., increase in total phytoplankton biomass and complex response of species composition) protect eutrophic lakes against perturbation (Van Der Molen et al. 1998; Anderson et al. 2005).

2.3 Control of phosphorus

As mentioned above, some lake restoration/management practices demonstrate that oligotrophication can be achieved by nutrient control. As phosphorus is a macronutrient for phytoplankton growth, phosphorus control has been widely studied for purposes of lake restoration.

2.3.1 Limiting Nutrients

The composition of organic matter in phytoplankton is approximately $C_{106}H_{263}O_{110}N_{16}P_1$. The organic matter is principally formed through the process of photosynthesis, which can be represented by (Wang 2003):

$$HPO_4^{2-} + 106CO_2 + 16NO_3^- + 122H_2O + 18H^+ + (\text{trace elements, energy}) = C_{106}H_{263}O_{110}N_{16}P_1 + 138O_2 \quad [2.1]$$

Although carbon (C), hydrogen (H) and oxygen (O) are abundant, nitrogen (N) and phosphorus (P) are limited in the environment. As a result, low amounts of either N or P can restrict algal growth (Scarlatos 1997). Smith (1979) reports that an N:P mass ratio greater than 21 indicates P is the limiting nutrient, whereas N may become the limiting nutrient at ratios less than 13. Phosphorus acts as the limiting nutrient in most temperate lakes, controlling the growth of phytoplankton and the process of eutrophication (Thomann and Mueller 1987).

2.3.2 Fundamental Information on Phosphorus

Phosphorus (P), the 15th element on the periodic table with an atomic weight of 30.974, is an essential nutrient for all life forms (Griffith 1973). Phosphorus is a constituent of deoxyribonucleic acid (DNA), ribonucleic acid (RNA), adenosine diphosphate (ADP), and adenosine triphosphate (ATP) (Corbridge 1985). This element is widely distributed in both soluble and particulate forms in all living cells, lakes, rivers, oceans, soils, and rocks (Horne and Goldman 1994). Soluble P includes inorganic P (generally in the soluble orthophosphate form), organic P excreted by organisms, and colloidal macromolecular P. Particulate phosphorus commonly includes living and dead cells, P precipitates, and P adsorbed onto particles.

2.3.3 Different Phosphorus Forms in Lake Water

The main source of phosphorus to lakes is soil erosion (Horne and Goldman 1994). Most phosphorus in soil is in particulate form as phosphorus reacts easily with metal ions to form relatively insoluble minerals such as calcium (Ca), iron (Fe), and aluminium (Al) phosphates. Total phosphorus in lake water consists of two principal components: total dissolved phosphorus (TDP) and total particulate phosphorus (TPP) (Thomann and Mueller 1987). The dissolved form is composed of dissolved inorganic phosphorus (DIP or orthophosphate) and complex dissolved organic phosphorus (DOP) (Björkman and Karl 2003). Orthophosphate ($H_2PO_4^-$, HPO_4^{2-}, and PO_4^{3-}) seems to be the only directly available P source for algae and bacteria (Bostrom et al. 1988). Small molecular weight DOP such as phosphomonoesters can be hydrolyzed into orthophosphate by phosphatase in the presence of carbon sources such as acetate. Large molecular weight DOP can be photolyzed into orthophosphate through ultraviolet radiation (Hullebusch et al. 2002). The particulate form consists of inorganic phosphorus particulates that originate from soil runoff, and organic phosphorus particulates that include phosphorus components from phytoplankton and detritus (Thomann and Mueller 1987). Particulate phosphorus is not directly available for the growth of algae and bacteria (Matsunaga et al. 1998).

2.3.4 Different Phosphorus Fractions in Sediments

Relatively insoluble aluminium-, iron-, and calcium-bound phosphates formed in the water column sink to the bottom (Griffith et al. 1973). Phosphorus in the sediment can be divided into a number of different fractions such as labile P, Fe-P, Al-P, organic-P, Ca-P, and residue-P (Rydin and Welch 1998). Labile P is loosely sorbed P, mainly soluble reactive phosphorus (SRP) in porewater. Fe-P, a potentially mobile P similar to P which is adsorbed to iron and manganese, is sensitive to low redox potentials. Al-P is relatively inert and is not redox sensitive. Organic-P includes bacteria-incorporated P. Ca-P is a stable fraction of sedimentary P. Residue-P consists mainly of inert inorganic P fractions as well as refractory organic P. These fractions do not correspond exactly to chemically defined compounds but are characterized by elution medium and conditions of sequential P extraction. Organic-P is often liberated by strong acid or alkaline solutions in sedimentary P extraction (Petterson et al. 1988).

2.3.5 Optimum Phosphorus Concentrations for Algal Growth

P is a required macronutrient for algal growth, and the growth of algae depends on the amount of available P and the rate at which it is cycled. The critical concentration of P (CCP) is the concentration required for maximum growth under the prevailing growth conditions (Griffith 1973). Freshwater algae are primarily divided into three categories according to the CCP and their tolerance limits (Wetzel 2001). Species in the first category (e.g., chlorophyte) have both a CCP and upper tolerance limit below 20 µgP/L. Species in the second category (e.g., diatoms) have a CCP below 20 µgP/L but a tolerance limit well above that level. *Asterionella formosa* is a diatom that reaches maximum cell density at a P concentration as low as 1 µgP/L. Species in the third category (e.g. cyanobacteria) have both the CCP and the upper tolerance limit above 20 µgP/L. *Oscillatoria rubescens*, a cyanobacterium, does not reach its maximum cell density until P concentrations are about 3000 µgP/L.

Optimum algal growth is obtained through P uptake and even P luxury uptake. Any amount of P absorbed by algae cells above the CCP implies storage of unused nutrient;

this excess is designated as luxury uptake P (LUP) (Cooke et al 1986). Excess P can be accumulated in algal cells and used for growth when external P becomes scarce. Filamentous cyanobacteria absorb excess P at P-enriched upper sediment layers and then dominate the phytoplankton community in P limited lakes (Cooke et al 1986). However, P uptake by diatoms can be dominant at high Si:P ratios in the phytoplankton community (Wetzel 2001).

2.3.6 Phosphorus Sources for Lakes

Many sources inside or outside of the lake can contribute phosphorus to the waterbody. Potential external phosphorus sources include point sources such as industrial and domestic discharge and nonpoint sources such as stormwater runoff and tributary inflow. Characteristically, point sources are comprised primarily of dissolved phosphorus, discharge in roughly equal daily amounts, and are measured easily (Jeunesse et al. 2002). Nonpoint sources typically are comprised primarily of particulate phosphorus, are associated with runoff events, are relatively difficult to quantify, and vary from year to year (Jeunesse et al., 2002). Only 5 to 10 percent of P from external P sources is carried to lakes in the dissolved form; the rest is transported as particles (Horne and Goldman 1994). External P loading may leave a legacy of stored P in lake sediment (Cooke et al. 2005).

Important internal sources include phosphorus release from sediments, aquatic plants, and algae into the water column. Generally, when the lake is stratified and the sediments become anoxic, a substantial amount of P is released into the water column from the sediments (Hart et al. 2003).

2.3.7 Phosphorus Control

Reducing external phosphorus loading is a commonly accepted measure for effective, long-term lake eutrophication control. Diversion, total elimination of the anthropogenic source, and/or advanced wastewater treatment normally removes ~90% or more P from

wastewater, have been commonly employed to limit external P loading. Such external restoration measures result in an immediate decrease of in-lake P levels (Ruloy and Rusch, 2004). However, they cannot significantly lower internal phosphorus loading (amount of P diffusing across the sediment-water interface) (Wadpersdolf et al. 2004). Recent studies indicate internal P loading from sediments is substantial. In some cases, internal P loading contributes to P in the overlying water at levels higher than external sources (Ruban and Demare 1998). In Lake Vedsted (Denmark), internal P loading was found to be more than four times greater than the external P loading (Hansen et al. 2003). Thus, even in cases where measures to control the external P loading have been successful, recovery of eutrophic lakes may still be delayed by continuous P release from sediments.

The lake water phosphorus concentration also plays a role in the delay in the recovery of eutrophic lakes. The P contribution from internal loading to the epilimnion in deep lakes during the summer can be low; despite nutrients accumulating in the hypolimnion during anoxia, the metalimnion can effectively isolate much of the sediment area from the epilimnion (Kalff 2002). High P concentration and adequate solar irradiation of the epilimnion in deep eutrophic lakes can support and accelerate a high rate of primary production. Sedimentation of epilimnion phytoplankton forms a fresh sediment layer. Thus, new P releases can result from the uppermost fresh sediment layer even when internal P control is employed.

Therefore, after external phosphorus loading has been minimized, accelerating the recovery of eutrophic lakes requires an in-lake treatment to remove P from the water column and limit P release from sediments.

2.4 In-Lake Treatment

2.4.1 Phosphorus Removal from Lake Water

Four methods are commonly used to remove P from the water column of lakes: (1) dilution and flushing; (2) hypolimnetic withdrawal; (3) chemical precipitation; and (4) phosphorus coprecipitation (Cooke et al 2005).

Dilution and flushing: This method involves the transport of additional water (usually of low nutrient content) to a lake, which effectively reduces the P concentration and increases the water exchange rate (Cooke et al. 2005). Dilution and flushing can reduce the P concentration, result in destratification, and increase the rate of loss of planktonic algae from the lake by increasing the water exchange rate. Some drawbacks of the method are the need for large quantities of low nutrient content water, high flushing rates, great cost, and necessity for repeated applications (Ryding and Rast 1989). For example, algal blooms in Moses Lake, Washington, returned due to a lack of continuous dilution and flushing (Welch and Patmont 1980).

Hypolimnetic withdrawal: This method involves changing the depth at which water leaves the lake from the surface (low-nutrient) to near the maximum depth (nutrient rich) (Cooke et al. 2005). As a result of the withdrawal of the nutrient-rich water, P content in the water column is decreased, residence time of the hypolimnion is shortened, anoxic sediment conditions are less likely to develop, and the availability of nutrients to the epilimnion is lessened. However, effects of this technology have only been demonstrated in deep lakes with a residence time of 2-5 years (Ryding and Rast 1989). Importantly, this method can be unsafe due to the release of high content H_2S that is produced in the anoxic hypolimnion (Klapper 2003). Also, the released hypolimnetic water is often cold, which can adversely affect the fishery.

Chemical precipitation: This method involves direct addition of phosphorus-precipitating chemicals such as iron or aluminium salts to a deep lake (Ryding and Rast

1989). The purpose of this method is to decrease the P content to the growth-limiting level by removing P from the water column (P precipitation) and by limiting P release from sediments (P inactivation) (Cooke et al. 1986). However, this method is only a temporary solution to eutrophication and the chemicals added are potentially toxic to lake biota. Increased soluble Al^{3+} or $Al(OH)_2^+$ ions are toxic to fish and other aquatic organisms in lake water with pH values below 5.5, and soluble toxic $Al(OH)_4^-$ ions are produced in lake water with pH levels above 8. Also, Hullebusch et al. (2002) state that the aluminium entering the lakes is mainly in colloidal form and toxic to lake biota. The buffering capacity of lake water would be exhausted in a short time after using Fe(III) compounds (Deppe and Benndorf 2002).

Phosphorus coprecipitation: This method involves P adsorption onto the surface of a coprecipitant, followed by a slow incorporation of phosphate into the crystal structure of the coprecipitant effectively scavenging P from the water column (Hart et al. 2003). Since the 1970s, this method has been widely studied because of its ecological significance in the control of eutrophication (Hartley et al. 1997). Previous studies demonstrate a number of coprecipitants are ineffective for P removal. Higgins et al. (1976) found that fly ash had little effect on P removal and that gypsum was not effective in P removal when pH values were less than 10. Wadpersdolf et al. (2004) described that calcite-rich lake marl, a natural deposit in hardwater lakes, was not a suitable material for P coprecipitation because it had no significant sorption of P. They also reported that if the amount of lime added to lake water was greater than 100 mg/L, pH levels would increase rapidly to more than 10, consequently causing increased mortality in pH-sensitive aquatic flora and fauna. Although a considerable amount of research on P coprecipitation by calcite ($CaCO_3$) seeded crystal growth has been conducted (Hart et al. 2003; Hartley et al. 1997), Dittrich et al. (1997) found the precipitated calcite crystals partially dissolved in the hypolimnion where waters are under-saturated with respect to calcite.

2.4.2 Limiting Phosphorus Release from Sediments

Common methods used to limit P release from sediments include: (1) hypolimnetic oxygenation; (2) sediment removal; (3) sediment oxidation; and (4) sediment capping and sealing (Cooke et al. 2005; Ryding and Rast. 1989).

Hypolimnetic oxygenation: This method involves introduction of oxygen into anoxic hypolimnetic waters without destratifying the water column (Cooke et al., 2005). The effectiveness of this method has not yet been demonstrated (Ryding and Rast 1989). Gächter and Wehrli (1998) found that high P release rates were not reduced after 10 years of hypolimnetic oxygenation in Lake Baldegg and Lake Sempach, Switzerland. Hypolimnetic oxygenation for five summer periods in deep Lake Vedsted, Denmark, resulted in only a moderate improvement in water quality (Hansen et al. 2003). Gächter and Müller (2003) and Hansen et al. (2003) found the main reason for failure of hypolimnetic oxygenation in their experiments was a lack of reactive Fe in the sediments to achieve a sufficient P binding capacity even under oxic conditions.

Sediment removal: This method involves dredging nutrient-rich sediments from the lake bottom (Cooke et al. 2005). Major objectives of this method are deepening, nutrient control, toxic substance removal, and rooted macrophyte control. Major drawbacks of the method are liberation of nutrients and toxic substances, associated expense, potentially adverse biological effects on biota, problems of sediment disposal, and potential pollution to the overlying water column. Cooke et al. (2005) insist that in most cases the side effects of this method are short term and negligible relative to the long-term benefits. Ruley and Rusch (2004) described the restoration of City Park Lake (Louisiana, USA) through dredging sediments in 1983; however, the P content during the 1989-1990 and 2000-2001 period reached the same level observed during the pre-treated years.

Sediment oxidation: This method involves injection of $Ca(NO_3)_2$ into the sediment to achieve greater binding of P by ferric hydroxide complexes (Hansen *et al.*, 2003;

Ryding and Rast. 1989). Advantages of this method are that NO_3^- can penetrate deeper into sediment than O_2 due to its higher solubility, and NO_3^- can produce a larger pool of oxidized Fe than O_2 (Hansen et al. 2003). However, this method has some drawbacks. The addition of NO_3^- may accelerate eutrophication and promote growth of Fe-reducing bacteria; the Fe-reducing bacteria can result in accelerated decomposition of Fe-P once NO_3^- is depleted (Hansen et al. 2003).

Sediment capping and sealing: This method involves physically covering or chemically sealing nutrient-rich sediments (Salonen and Varjo 2000). Sediment capping involves placing a layer of material over sediments to isolate them from the water column (Sharma and Reddy 2004). Materials such as sand, clay, gravel, silt, and fly ash have been tested and used in the sediment capping (Dunst et al. 1974; Cooke 1980; Cooke et al. 2005; Baker et al. 1993). Sediment capping physically isolates contaminants and stabilizes sediments (Sharma and Reddy 2004). However, this method may accelerate lake aging by decreasing the lake volume; the long-term performance of sediment capping is also unknown (Cooke et al., 2005; Sharma and Reddy 2004).

Sediment sealing involves chemically treating nutrients in sediments to render them immobile; this is also defined as P inactivation (Cooke et al. 2005; Sharma and Reddy 2004). Materials such as calcite, lime, and alum and ferric salts have been tested and used to seal sediments (Berg et al. 2004; Hart et al. 2003; Zhang and Prepas 1996; Welch et al. 1982).

Hart et al. (2003) evaluated three calcite barrier materials—limestone, ESCal, and SoCal—for Lake Carramar (Australia) sediments and found the determinative mechanism of sealing sediment by calcite was P adsorption. Hart et al. did not evaluate the long-term effects of sealing sediment by calcite as the duration of their experiment was only 60 days. Furthermore, they did not consider in their experiments that the acidification of anoxic hypolimnion waters could lead to partial dissolution of calcite.

Zhang and Prepas (1996) used lime to limit P release from sediments; P release from sediments was observed in all three experimental lakes only after 10 days. Moreover, a rapid increase in pH values occurred when the dosage of lime was greater than 100 mg/L. A rapid increase in pH values can lead to mortality in pH-sensitive aquatic flora and fauna.

2.5 Diatomite

In addition to the common in-lake P treatment methods, Krivstov et al. (2000) proposed a new approach to lower P content and control cyanobacterial blooms. If the spring diatom bloom is promoted by artificial addition of Si, more P will be assimilated by the readily settlable diatoms. Sedimentation of diatoms removes P from the lake water column and thus reduces the magnitude of cyanobacteria blooms in the summer. However, Krivstov et al. (2000) did not specify which Si sources are suitable for this approach. The study described in this thesis follows the method proposed by Krivstov et al. (2000) and uses diatomite as an external Si source for stimulating diatom growth.

Diatomite is a very fine-grained siliceous sedimentary rock made from the accumulation and compaction of diatoms (Goren et al. 2002). Diatomite is regarded as a mineral of organic Si origin, where the silica from diatomite skeletons resembles opal or hydrous silica ($SiO_2 \cdot nH_2O$) (Khraisheh et al. 2005). Diatomite is available in large deposits around the world. The typical chemical composition of diatomite is 86% silica (Si), 5% sodium (Na), 3% magnesium (Mg), and 2% iron (Fe). Diatomite is mainly composed of diatom shells and may contain other sediments such as clay and quartz (Goren et al. 2002; Chaisena and Rangsriwatananon 2005). The compaction of many small hollow diatom frustules with varied surface structure results in high porosity (80-85% voids) (Göll et al. 1989). These voids form billions of microscopically fine interstices in which suspended particles can be trapped (Kogel et al. 2006). Due mainly to its high porosity, high permeability, low thermal conductivity, chemical inertness, and low cost, diatomite can be used in a number of industrial applications: as filtration media for various beverages; as an adsorbent for oil spills; as a mild abrasive; and as a mechanical insecticide.

2.6 Ferrihydrite

Not only can Si sources stimulate diatom growth, recent studies show the spring diatom bloom can be further promoted by iron enrichment in high-silicate conditions (Takeda 1998; Boyle 1998).

Principal forms of ferric (Fe(III)) oxide in nature are, in order of increasing crystallinity: ferrihydrite, maghemite (γ-Fe_2O_3), lepidocrocite (γ-FeOOH), hematite (α-Fe_2O_3), and goethite (α-FeOOH). As the structure of ferrihydrite is still the subject of controversy, several formulas for ferrihydrite have been proposed including $Fe_2O_3.0.5H_2O$, $5Fe_2O_3.9H_2O$, $Fe_5HO_8.4H_2O$, $Fe_2O_3.2FeOOH.2.6H_2O$, and $FeOOH.0.4H_2O$.

Ferrihydrite is a brown ferric oxide with the least crystallinity in nature. Due to its poor crystallinity, ferrihydrites yield a variety of X-ray diffraction patterns, ranging from two very broad resonances indicating very poorly crystalline material (defined as 2-line ferrihydrite) to six broad but distinct resonances indicating a more highly crystalline material (6-line ferrihydrite) (Gautier et al. 2006). A decrease in surface area is a characteristic of the transformation from 2-line ferrihydrite to 6-line ferrihydrite (Kukkadapu et al. 2003).

The high surface area of ferrihydrite of approximately 200-840 m^2/g makes it an important constituent for surface related processes such as adsorption (Weidler 1997; Zhao et al. 1994). Ferrihydrite is the most effective P adsorbent among soil minerals (Rhoton and Bigham 2005). However, ferrihydrite is recognized as a transient or metastable phase which with time transforms to more crystalline phases such as hematite and goethite (Rhoton and Bigham 2005; Glasauer et al. 2000). Under natural conditions, surfaces of ferrihydrite are contaminated by compounds such as phosphate, silicate, arsenate, and organic acids (Rhoton and Bigham 2005). These surface impurities inhibit the transformation of ferrihydrite to more crystalline oxides.

Ferrihydrite stabilized by impurities, especially Si-containing ferrihydrite, has been the subject of considerable attention. Regarding the mechanism of the inhibition of ferrihydrite transformation by Si, Parfitt et al. (1992) proposed a model in which silicate bridges the surface of ferrihydrite domains, which aggregate to form primary particles. The Si is coprecipitated into the ferrihydrite structure primarily through the Fe-O-Si bonds (Vempati and Loeppert 1989; Glasauer et al. 2000). Dissolved Si exerts a strong influence on the crystallinity of ferrihydrite (Ford et al. 2006). The degree of crystallinity of ferrihydrite decreases with increasing Si content (Seehra et al. 2004).

2.7 Gypsum

As previously described, sediment capping and/or sealing has been the subject of recent extensive study. Many of the materials tested resulted in a large decrease in lake volume, thereby accelerating the lake aging process. As such, a more effective sealing material is required to improve the success of *in situ* sediment capping technologies. In this thesis, gypsum was selected for the purposes of physically capping and/or chemically sealing sediment.

Gypsum is one of the most common minerals in sedimentary environments. It is a major mineral produced in massive beds, usually precipitating from highly saline waters. Gypsum is usually silky and fibrous, and can be anywhere from transparent to opaque. Gypsum can range widely in size from very fine-grained to granular, with a specific gravity from 2.31 to 2.33. Gypsum is predominantly composed of water-containing calcium sulphate, and is represented by the chemical formula $CaSO_4.2H_2O$. Gypsum is slightly soluble in water (13.78×10^{-3} mol/L at 25 °C and atmospheric pressure). Gypsum dissolves over time due to the incongruent dissolution of gypsum, as described by (Forti 1997):

$$CaSO_4.2H_2O + H_2O + CO_2 \leftrightarrow CaCO_3 + SO_4^{2-} + 2H^+ + 2H_2O \qquad [2.2]$$

Gypsum is non-toxic to humans and animals, and does not burn. It is also neutral, and therefore does not significantly change the pH of lake water or sediment. The US is the

world's leading producer of gypsum; other important producers are China, Iran, Thailand and Spain.

When calcined (roasted) at temperatures of 120-250°C, gypsum releases 75% of its water. When mixed with water, gypsum can be molded, shaped or spread, then dried or set to form hard plaster. The principal use for gypsum is wallboard. Crude gypsum is pulverized and heated to form stucco, which is mixed with water and aggregate (sand, vermiculite or expanded perlite) and applied over wood, metal, or gypsum lath to form interior wall finishes. Gypsum is also used as a filler in paint and paper manufacturing, as a substitute for salt cake in glass manufacture, and as a soil conditioner.

2.8 Phosphorus Adsorption

As described above, the determinative mechanism of P coprecipitation and P inactivation is P adsorption. Simulation of the adsorption process involves the study of adsorption properties and equilibrium data (Mondal and Lalvani 2000).

2.8.1 Adsorption Isotherms

Adsorption properties and equilibrium data, commonly known as adsorption isotherms, describe how adsorbates interact with adsorbent materials and are valuable for optimizing adsorbent use. In the case of P, adsorption equilibrium is established when the amount of adsorbed P is equal to the amount being desorbed from the adsorbent material (Crini and Peindy 2006). The Langmuir, Freundlich, and Temkin isotherm equations are most frequently used to represent adsorption from solution.

The widely used Langmuir isotherm has found successful application in many real adsorption processes and is expressed as:

$$Q_e = \frac{K_L C_e}{1 + a_L C_e} \qquad [2.3]$$

A linear form of this expression is:

$$\frac{C_e}{Q_e} = \frac{1}{K_L} + \frac{a_L}{K_L} C_e \qquad [2.4]$$

where Q_e is the amount of adsorbed P in mg per gram of adsorbent, and C_e is the unadsorbed P concentration in solution at equilibrium. The constant K_L is the Langmuir equilibrium constant and K_L/a_L gives the theoretical monolayer saturation capacity, Q_0. Therefore, a plot of C_e/Q_e versus C_e gives a straight line of slope a_L/K_L and intercept $1/K_L$.

The well-known Freundlich isotherm is often used for heterogeneous surface energy systems. The Freundlich equation is given as:

$$Q_e = K_F C_e^{1/n} \qquad [2.5]$$

A linear form of this expression is:

$$\ln(Q_e) = \ln(K_F) + \frac{1}{n}\ln(C_e) \qquad [2.6]$$

where K_F is the Freundlich constant and *n* is the Freundlich exponent. K_F and *n* can be determined from the linear plot of $\ln(Q_e)$ vs. $\ln(C_e)$.

The Temkin isotherm has been used in the following form:

$$Q_e = \frac{RT}{b}\ln(AC_e) \qquad [2.7]$$

where R is the gas constant (8.31 J/mol K) and T is the absolute temperature.
A linear form of the Temkin isotherm can be expressed as:

$$Q_e = \frac{RT}{b}\ln(A) + \frac{RT}{b}\ln(C_e) \qquad [2.8]$$

where

$$\frac{RT}{b} = B \qquad [2.9]$$

A plot of Q_e versus $\ln(C_e)$ enables one to determine the constants *A*, *B*, and *b*.

2.8.2 Characterization of Adsorbent Materials

Adsorption is the enrichment of one or more components in an interfacial layer, when an adsorbate comes in contact with the surface of an adsorbent. The exact nature of the adsorption depends on the characteristics of adsorbent materials. The relevant characteristics of the adsorbent are surface area, pore volume, pore structure, surface structure, surface charge, crystallinity, and electronic structure (Wachtman 1993). Correspondingly, common technologies for the characterization of adsorbent materials are the Brunauer, Emmett, and Teller (BET) method, scanning electron microscope (SEM), transmission electron microscope (TEM), X-ray diffraction (XRD), surface charge, and X-ray absorption near-edge structure (XANES) spectroscopy (Lynch 2003).

2.9 X-ray Absorption Near-Edge Structure (XANES) Spectroscopy

2.9.1 X-ray Absorption Spectroscopy (XAS) and Synchrotron Facility

X-ray absorption spectroscopy (XAS) is currently a widely used technique providing information on the local structure and chemical environment of condensed matter and gas-phase molecules. X-ray absorption occurs due to core electrons absorbing the X-ray and then being excited and ejected from the atom as photoelectrons. X-ray absorption spectra are obtained by tuning the photon electron energy in a range 0.1-100 keV where bound electrons can be excited. XAS is usually applied at synchrotron radiation facilities that can provide intense and tunable X-ray beams. A schematic of a synchrotron radiation facility is shown in Figure 2.2. A synchrotron produces extremely bright light by accelerating electrons to nearly the speed of light through a linear accelerator (Figure 2.2). The electrons are accelerated repeatedly in the booster ring until they are at a sufficient energy to be injected into the storage ring. In the storage ring, the electrons orbit continuously for approximately 20 hours and give off synchrotron radiation. Storage rings are essential facilities to create brilliant beamlines in the wide spectral range essential for XAS measurements. XAS experiments are conducted at an endstation using suitable beamlines, which consist of a sample holder and a detection system (Figures 2.2 and 2.3).

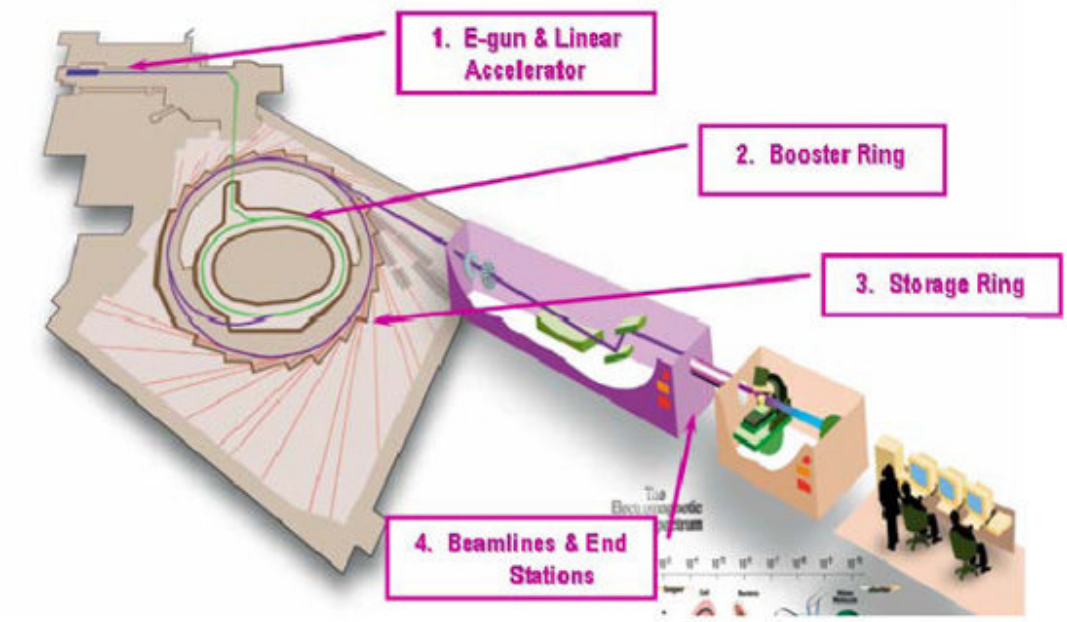

Figure 2.2 Synchrotron radiation facility schematic (Adapted from www.lightsource.ca)

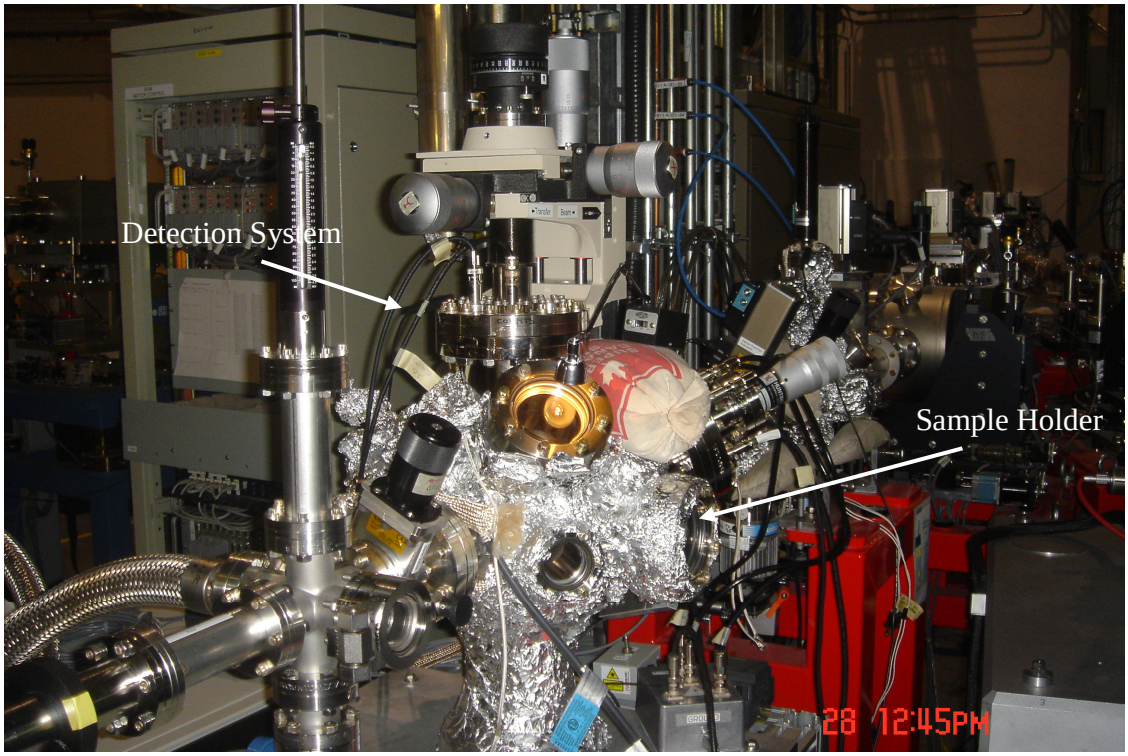

Figure 2.3 A typical end station from a synchrotron radiation facility

2.9.2 X-ray Absorption Near-Edge Spectroscopy (XANES)

2.9.2.1 XANES and electronic transition

Applications of XAS have primarily involved structural determination by extended X-ray absorption fine structure (EXAFS) and oxidation state characterization using chemical shifts in the XANES region (Cramer et al. 1998). The shifts in energy of core levels between free atoms and chemically bound atoms are called chemical shifts. X-ray absorption near-edge structure (XANES) spectroscopy is the study of electronic transition from atomic core levels to unoccupied molecular states (antibonding orbitals) below and above the continuum levels in the absorbing atom (Varlot et al. 2001) (seen in Figure 2.4). The XANES region extends over a range of about 100 eV, between the edge region and the EXAFS region.

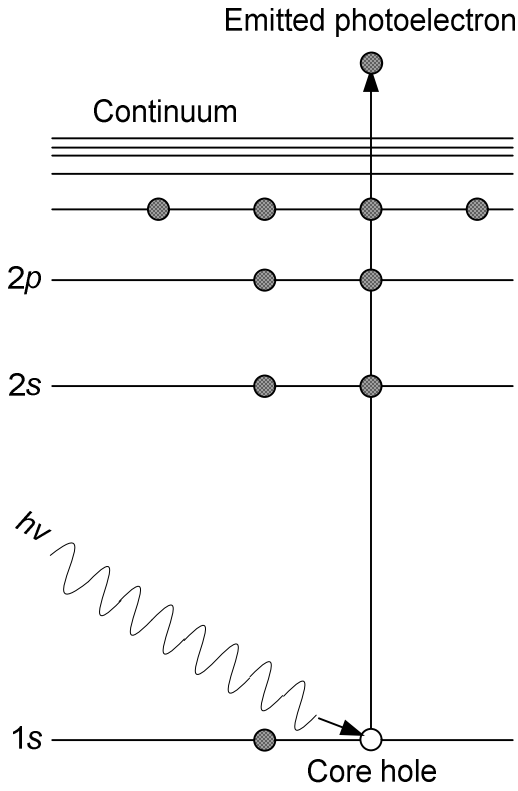

Figure 2.4 Electronic transition from atomic core level 1s to unoccupied molecular states

The atomic core levels are located near a nucleus and are not directly involved in the formation of chemical bonds. In order of increasing energy, the atomic core levels in a given atom are $1s < 2s < 2p < 3s < 3p < 3d < 4s$ (Sutton 1993) (Figure 2.5).

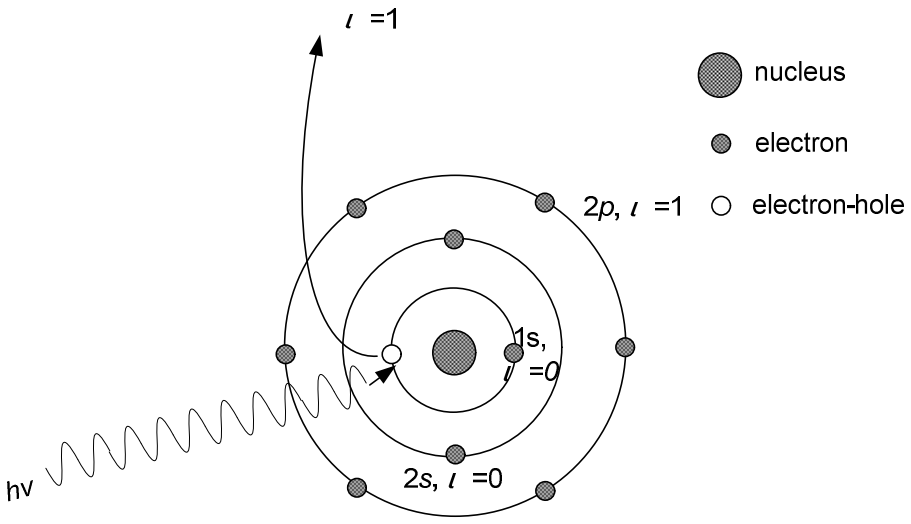

Figure 2.5 Core level position of an isolated atom

The continuum levels are high-energy unbound states, weakly influenced by the molecular field (Margeritondo 1988). An antibonding orbital is a form of molecular orbital (MO) that is located outside the region of two distinct nuclei. The energy change associated with this transition provides information on the structure of a molecule and can be used to determine chemical, physical, and structural properties. Thus, XANES is a powerful tool for chemical state analysis, by providing spectra features such as peak shifts and changes of line shapes and intensities (Kawai et al. 2000). More importantly, XANES spectroscopy has been currently used in the chemical and structure characterization of disordered systems like amorphous materials (Franke and Hormes 1995).

2.9.2.2 K-edge and L-edge absorption

Promotion of a 1*s* electron is termed K-edge absorption (seen in Figurs 2.4, 2.5, and 2.6); and similarly, L-edge absorption involves 2*s* or 2*p* electrons (seen in Figure 2.6). L-edge absorption is subdivided into L_3 and L_2 edges, which come from spin-orbit splitting of the 2*p* hole into $2p_{3/2}$ and $2p_{1/2}$ final states, respectively. L_1 edge absorption

results from promotion of the 2*s* electron (Figure 2.6). The resulting 2*p* core hole from the excited 2*p* electron means that the total spin angular momentum is no longer zero; this causes coupling between the orbital and spin angular momentum to split the 2*p* level into $2p_{3/2}$ and $2p_{1/2}$ levels. The spin is the angular momentum intrinsic to a body, which is the motion of its center of mass about an external point. Spin-orbit coupling is any interaction of a particle's spin with its motion. Spin-orbit splitting involves the removal of state degeneracy by spin-orbit coupling. K-edge and L-edge absorption is also described in Figure 2.6.

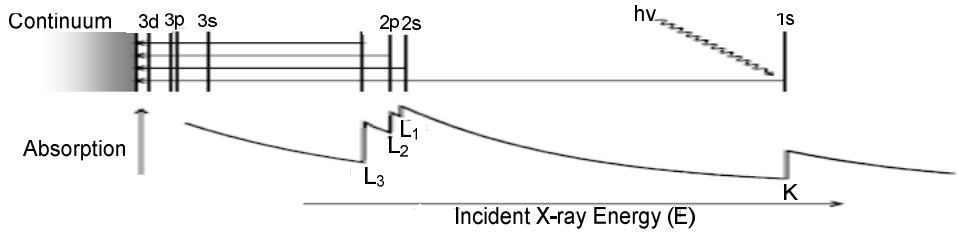

Figure 2.6 K-edge and L-edge X-ray absorption

2.9.2.3 Dipole selection rule

The electronic transition is guided by the dipole selection rule, $\Delta l = \pm 1$ (Behrens 1992). The quantum number l can change by ± 1 during a dipole-allowed transition; dipole-forbidden transitions occur at a low rate. Dipole-allowed transitions result in intense features in XANES spectra, whereas dipole-forbidden transitions create weak features. Table 2.2 describes the principal quantum number of core levels in an atom.

Table 2.2 Principal quantum numbers of core levels in an atom, where *n* is principal; *l* is azimuthmal, *l* = 0, 1, 2..., specifying *s*, *p*, *d* orbital, respectively.

Spin	*n*	*l* (Azimuthal quantum number)
1*s*	1	0
2*s*	2	0
2*p*	2	1
3*s*	3	0
3*p*	3	1
3*d*	3	2

For a K-edge, the excited 1*s* electron has no angular momentum (*l*=0), thus $\Delta l = +1$ and the resulting photoelectron has *l* =1. The final state of the outgoing 1s electron therefore has *p* symmetry. For an L_3 edge or an L_2 edge, the initial state electron is 2*p* with *l* =1 and the final state thus has either *l* =2 (*d* symmetry) or *l* =0 (*s* symmetry).

2.9.2.4 Detection methods

Direct measurement of a XANES spectrum involves recording the intensity both with (I) and without (I_0) a sample in place, and then deriving the absorbance ($\log(I_0/I)$) as a function of X-ray photon energy (*eV*). This measurement procedure is described in Figure 2.7.

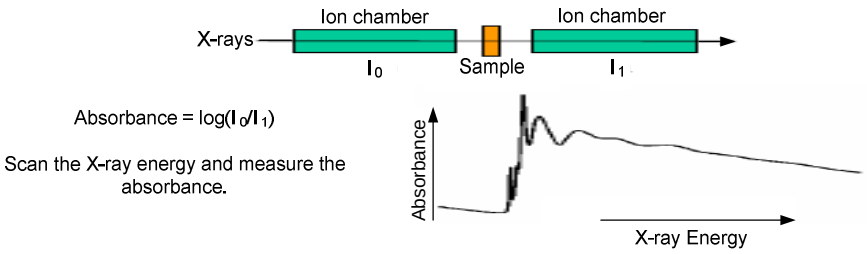

Figure 2.7 Direct measurement of the X-ray absorption spectrum

The most common detection methods of XANES are to either measure total electron yield (TEY) or to measure fluorescence yield (FY) (Kawai et al. 2000). As the total electron or fluorescence photon yield emitted from the sample is proportional to the absorption coefficient, both techniques are equivalent to a transmission measurement (Kasrai et al. 1996). Because the electron escape depth is short (<100 A), TEY is very surface sensitive. The FY method is the dominant technique for hard X-ray experiments. In the soft X-ray region, atoms relax after X-ray absorption primarily by emission of an Auger electron. One can measure a signal related to the absorption cross section by recording the Auger electron yield. The measurement of an absorption spectrum is illustrated in Figure 2.8.

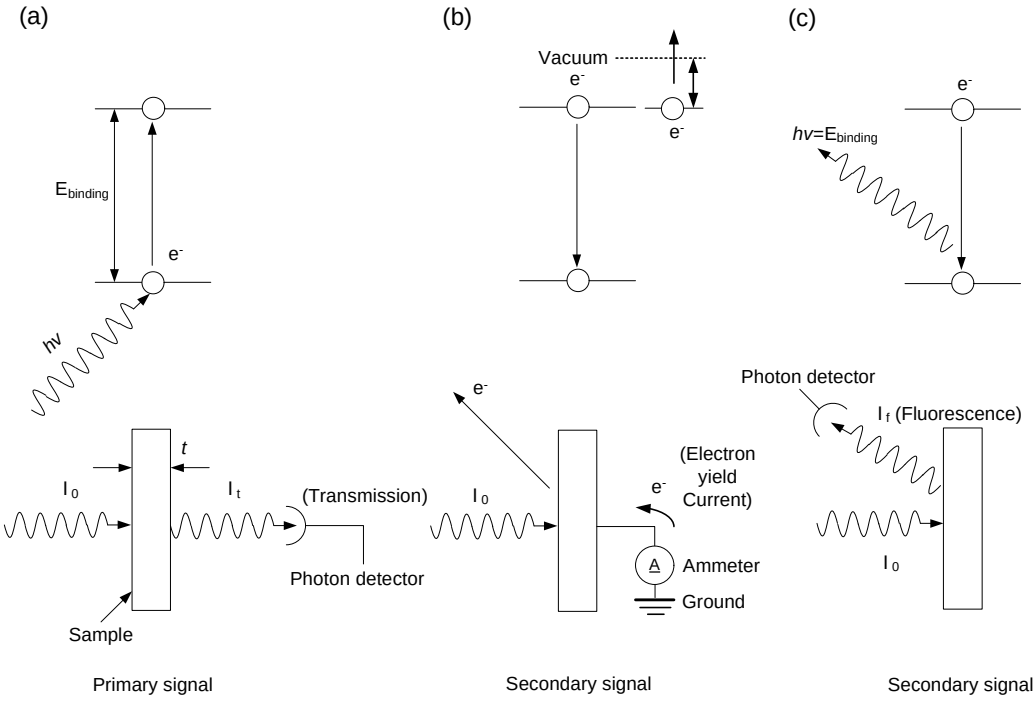

Figure 2.8 Schematic illustration of different detection modes (adapted from Cramer et al. 1998) (a) TEY mode; (b) FY mode; (c) Auger yield

The differences between TEY and FY modes are (Kawai et al. 2000):

(1) Probing depth difference. The FY method is bulk sensitive, and probes from the surface as deep as the X-ray attenuation. However, the TEY method is surface sensitive, as shallow as 0.5-10 nm from the surface.

(2) Self-absorption effect. The fluorescent X-ray photons omitted in the bulk are absorbed during transit within the solid. This is called the self-absorption effect, and smears the line shape of absorption spectra when the FY method is used.

(3) Decay channel difference. The emission of X-ray fluorescence should be from an electric dipole transition. Thus, the fluorescent decay channel depends on the orbital symmetry. On the other hand, the electrons detected by the TEY method are the Auger electrons, secondary electrons, and photoelectrons.

2.9.2.5 Data analysis

Data obtained from XANES experiments is processed to form XANES spectra (Koningsberger and Prins 1998). The data processing is carried out by computer programs. At first, individual sweeps and channels are averaged to form one set of data to improve the intensity-to-noise ratio. The averaged spectra can be calibrated by reference to standard compounds with known electronic structure. Averaged and calibrated data is often called the "raw" data. The pre-edge region of the raw data is fitted linearly and the so determined background is subtracted from the whole spectra. The spectra obtained are normalized to compare the intensity of the absorption features quantitatively through setting the absorption jump to 1. The intensities of absorption features correspond to their area. These data are obtained by means of the least-square fitting method (Figure 2.9).

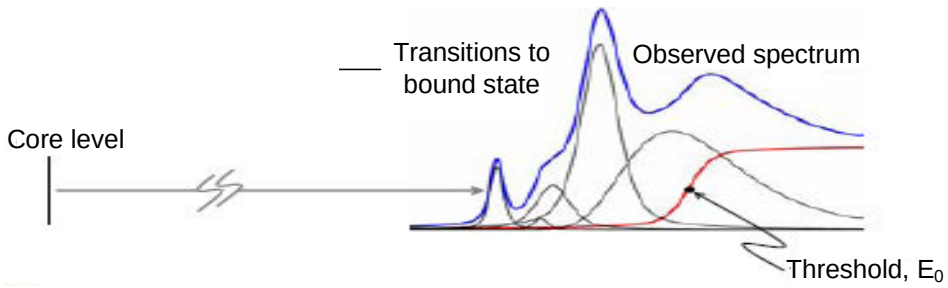

Figure 2.9 Peak-fitting analysis of an X-ray absorption spectrum

2.9.2.6 Applications of XANES in the research

The XANES region is dominated by different and more complicated processes, involving localized transition of the excited electron to unoccupied electron levels as well as multiple scattering events. Calculation of XANES spectra are performed using two approaches. One approach is the application of the multiple scattering (MS) theory, which requires some structural information in advance. Although the MS method is becoming increasingly elaborate, the tedious calculations are restricted to solids with an

uncomplicated structure (Behrens 1992). Another approach utilizes the XANES features as "fingerprints" and tries to reveal information by comparing XANES spectra of the compound investigated with a series of reference samples. This approach may yield important information even without detailed knowledge of the processes causing the XANES features. In this thesis research, the fingerprint approach was used. Important information can be obtained from so-called "shape resonances", dominating features in the XANES region that are related only to the nearest coordination environment, i.e. to the shape of the first coordination sphere. The two most important coordination types for inorganic compounds, i.e. tetrahedral and octahedral coordination, can also be identified by characteristically shaped resonances.

XANES is a powerful tool for element-specific characterization of local structure and chemistry (Bergmann et al. 2002). In this thesis research, Si, P, and Fe in diatomite (SiO_2), ferrihydrite ($Fe_2O_3.0.5H_2O$), and phosphate were characterized by XANES. The electronic configuration of Si, P, and Fe atoms are $1s^2 2s^2 2p^6 3s^2 3p^2$, $1s^2 2s^2 2p^6 3s^2 3p^3$, and $1s^2 2s^2 2p^6 3s^2 3p^6 4s^2 3d^6$, respectively (Sutton 1993).

The network structure of SiO_2 is tetrahedral, where each positive Si ion is surrounded by four oxygen atoms forming a SiO_4 unit (Bianconi 1979). The local structure of SiO_2 is determined by the similarity of the shapes of the surface and the bulk spectra. The strong similarity between the surface and the bulk spectra reveals that the oxide monolayer is formed by SiO_4 microscopic structure units. The Si-O bonds of the SiO_4 units are the hybridization of O 2*p* and Si 3*s* or 3*p* orbitals, respectively, depending on the energy loss. The Si K-edge XANES spectra reflect transitions from the Si 1*s* core level to the unoccupied Si 3*p*-derived states. This transition is allowed by the dipole selection rule, thereby forming a sharp main peak in the Si K-edge spectra of SiO_2. Si L-edge spectra of SiO_2 have drawn more attention from researchers because they are more complex and hence yield more information than their K-edge counterparts. Si L-edge spectra have spin-orbit splittings, which are assigned to the $2p_{3/2,\ 1/2} \rightarrow a_1^*$

transitions. The a_1^* is the molecular orbital with 3*s* characteristics. The distance of the spin-orbit splittings is ~0.8-0.9 eV.

All of the Fe^{3+} in ferrihydrite is in an octahedral coordination (Stoylar et al. 2007), where each positive Fe ion is surrounded by six oxygen atoms forming a FeO_6 unit. The 3*d* states of Fe couple mainly with the oxygen 2*p* states to form the Fe-O hybridization (deGroot 1993). Fe-O bonding, taking place in a distorted cubic crystalline surrounded by oxygen atoms, causes the Fe 3*d* states to split into the t_{2g} and e_g manifolds (Kendelewicz et al. 2000). For Fe^{3+} with an unfilled 3*d* level, L-edge spectra (2*p* X-ray absorption) reveal electronic transitions from an initial state $2p^6 3d^5$ to a $2p^5 3d^{5+1}$ final state (Kuiper et al. 1993).

Orthophosphates are composed of tetrahedral PO_4-groups with metal cations (Me) in the void spaces of the crystal structure. The ionic compounds with sum formulas Me_3PO_4 and $Me_3(PO_4)_2$ as well as covalent phosphates $MePO_4$ belong to these species, which are formed through the hybridization of Me 3*d*, O 2*p*, and P 3*p* valence orbitals (Franke and Hormes 1995). The P K-edge XANES spectra reflect transition from the P 1*s* core level to the unoccupied P 3*p*-derived states. A main sharp peak in present in the P K-edge spectra as this transition is allowed by the dipole selection rule. The P L-edge spectra are characterized by spin-orbit splitting of the P 2*p* electrons and transition to the antibonding orbitals (Li et al. 2007). Phosphate is usually adsorbed on surfaces of Ca-, Fe-, or Al- minerals. Distinguishing adsorbed from Ca-, Fe-, or Al- minerals is possible based on intensity and position of the white line (an intense resonance) energy as well as the absence or presence of pre-edge features in the P K-edge XANES region (Hesterberg et al. 1999).

Chapter 3 – Conceptual Development of Ferrihydrite-Modified Diatomite

Eutrophic lakes are typically characterized by shifts toward the dominance of phytoplankton by cyanobacteria (Smith et al. 1999). Cyanobacteria blooms can cause unsightly aesthetic and recreational interferences, foul odours, fish kills, and detrimental water quality (Thomann and Mueller 1987). The restoration of eutrophic lakes should fundamentally be managed by reducing the phosphorus (P) mass flow from the drainage basin. In many cases, however, the low P mass flow thresholds necessary for recovery cannot be effectively or efficiently achieved due to economic constraints in reducing P point sources and/or to a high proportion of P non-point sources (Xiong and Peng 2008a). Under these circumstances, in-lake eutrophication control methods can support or accelerate measures against eutrophication (Ryding and Rast 1989; Xiong and Peng 2008a). Among the large number of potential in-lake control measures (Cooke et al. 2005), P coprecipitation plays an important role. The selection and development of appropriate coprecipitants are key for the successful application of a P coprecipitation process. Materials such as lime, fly ash, alum, calcite, ferrous salts, and ferric salts have been tested (Higgins et al. 1976; Deppe and Benndorf 2002; Xiong and Peng 2008a; Sherwood and Qualls 2001; Hullebusch et al. 2002; Wadpersdolf et al. 2004).

In addition to the common in-lake P control methods, Krivstov et al. (2000) proposed a new approach to lower P content and control cyanobacteria blooms. If spring diatom blooms are promoted by the artificial addition of Si, more P will be assimilated by easily settlable diatoms and removed from the lake water column, thereby reducing the magnitude of nuisance cyanobacteria blooms in the summer. However, they did not specify which Si sources are suitable for this approach. Moreover, the spring diatom

bloom can be further promoted by iron enrichment in high-silicate conditions (Takeda 1998; Boyle 1998).

In the research in this thesis, a new method to integrate P coprecipitation with biological diatom P uptake is proposed to be capable of removing P with greater efficiency than either P coprecipitation or diatom P uptake alone.

Diatomite is a siliceous sedimentary rock formed from the accumulation and compaction of diatoms, and is available in large deposits around the world (Goren et al. 2002). The SiO_2 content of diatomite usually ranges between 80 and 90%. The solubility of SiO_2 is 0.012 g per 100 g of water. When a lake is dosed with diatomite, the diatomite can settle down to the sediment because the specific density of diatom frustules is nearly twice that of water (Harwood 1999). Moreover, diatomite has been approved as a food-grade material by the U.S. Food and Drug Administration (FDA). Thus, diatomite can be safely used as an external Si source for stimulating diatom growth. However, a low specific surface area (24.77 m^2/g; Table 5.1; discussed in Section 5.1.5) indicates that raw diatomite is not a suitable P coprecipitant although it is a good source of Si. Therefore, a surface modification technique is required to increase the surface area and improve the surface characteristics of the raw diatomite. The resulting modified diatomite can then act as an effective P coprecipitant while also providing an external Si source to stimulate diatom growth. Diatomite is amenable to surface modification due to its high porosity (80-85%), caused by the compaction of many small, hollow diatom frustules with various surface structures (Göll et al. 1989). The high porosity allows diatomite to be an appropriate carrier for materials utilized for its modification.

Several methods can be used to modify the surface characteristics of diatomite for various purposes. When diatomite is purified in HCl (Goren et al. 2002) or calcinated (Goren et al. 2002; Khraisheh et al. 2005), processes to make it more inert prior to use as filter support, OH groups on the surface disappear and the surface area is reduced.

Khraisheh et al. (2004) modified diatomite by NaOH treatment and manganese oxide (MnO_2) deposition to improve the adsorption capacity of the diatomite for removal of heavy metals such as Pb^{2+}, Cu^{2+}, and Cd^{2+} from wastewater. Their modified diatomite had a surface area of 80 m^2/g and demonstrated adsorption capacities of 99.00 mg Pb^{2+}/g, 55.56 mg Cu^{2+}/g, and 27.86 mg Cd^{2+}/g. Khraisheh et al. (2004) concluded that manganese oxide and its blockage of the diatomite pores played an important role in the adsorption of the heavy metals.

Proper selection of metal oxides for deposition in diatomite is crucial to effectively modify diatomite for P removal. Ferric oxide was chosen to block the diatomite pores in this study because iron is environmentally safe and diatom growth can be stimulated by iron enrichment in high-silicate conditions. Ferric oxide is present in nature in several principal forms: ferrihydrite, maghemite, lepidocrocite, hematite, and goethite. Ferrihydrite would be the ideal form of ferric oxide to modify diatomite due to its high specific surface area, ability to adsorb P, relatively high dissolution in water, and individual particle size. Ferrihydrite is the least crystalline iron (III) oxide. The colloidal-size ferrihydrite has a high specific surface area (approximately 200-840 m^2/g), which makes ferrihydrite an important constituent for surface-related processes, such as adsorption (Weidler 1997). Ferrihydrite is the most effective adsorbent among soil minerals for the retention of P from phosphate fertilizer (Rhoton and Bigham 2005). The theoretical solubility constant of ferrihydrite is higher than other ferric oxides ($\log K_s$=5.66) (Kirpichtchikova et al. 2006). Thus, if utilized in lake restoration, ferrihydrite would provide dissolved Fe for stimulating diatom growth.

The International Union of Pure and Applied Chemistry (IUPAC) classifies the pores of porous materials as follows: macropores have pore widths greater than 50 nm, mesopores have pore widths ranging from 2 to 50 nm, and micropores have pore widths less than 2 nm. Ferrihydrite can deposit into diatomite macropores and mesopores and partially block them. However, it cannot deposit into and completely block micropores because the size of an individual ferrihydrite particle is in the range of 2-5 nm (Tuhela et

al. 1992). Both the pore blockage and additional micropores introduced by microporous ferrihydrite are speculated to increase the overall volume of micropores, thereby increasing the surface area of the modified diatomite. However, pure ferrihydrite is recognized as a transient phase of an iron (III) oxide, and is not as stable as naturally occurring ferrihydrite possibly contaminated by Si, P, and As (Rhoton and Bigham 2005). Pure ferrihydrite can transform to more crystalline ferric oxides, such as lepidocrocite, hematite, or even goethite through aggregation and recrystallization (Banfield et al. 2000; Mayer and Jarrell 2000). A decrease in surface area and an increase in particle size are characteristics of the ferrihydrite transformation (Kukkadapu et al. 2003; Penn et al. 2006). In the process of ferrihydrite transformation, P adsorbed by ferrihydrite can be released back into solution with time (Mayer and Jarrell 2000; Crosby et al. 1981). Therefore, a stable ferrihydrite is preferred for modification of the diatomite.

Stable ferrihydrite can be formed from Fe(II) oxidation in the presence of dissolved silica (Si) because more Fe^{3+} vacancies caused by chemisorbed Si^{4+} loosen the crystalline lattice (Seehra et al. 2004) and Si^{4+} inhibits the ripening and agglomeration of Fe oxide particles (Crosby et al. 1981). Dissolved silica can be produced by NaOH treatment of raw diatomite because silicic acid (H_4SiO_4) and biogenic Si of diatom frustules are unstable at high pH (pK_a value of silicic acid is 9.7; Göll et al. 1989). Thus, the dissolved Si provided by the diatomite itself contributes to the formation of stable ferrihydrite from the Fe(II) oxidation. The role of NaOH in the Khraisheh modification of diatomite is only to react with manganese (II) chloride ($MnCl_2$) to form MnO_2. Dissolved Si does not contribute to the formation of Mn-modified diatomite. In the research presented in this thesis, NaOH can react with ferrous compounds including $FeCl_2$ to form $Fe(OH)_2$, and then in two stages can form the stable ferrihydrite: oxidation of $Fe(OH)_2$ incorporating Si^{4+} followed by formation of ferrihydrite. Hereafter, the product of the deposition of ferrihydrite into larger mesopores and macropores of diatomite is referred to as ferrihydrite-modified diatomite (FHMD).

Chapter 4 – Materials and Methods

4.1 Development and Characterization of Ferrihydrite-Modified Diatomite

4.1.1 Preparation of Ferrihydrite-Modified Diatomite

Unprocessed diatomite (FN6, brand name) was obtained from Eagle Picher Filtration & Minerals Inc, Nevada, USA. FN6 is composed of 89.2% SiO_2, 4% Al_2O_3, 1.5% Fe_2O_3, 0.5% CaO, 0.3% MgO, and 0.5% other oxides. FN6 samples (15 g) were immersed in 100 mL NaOH solution of differing concentrations at 85°C for 2 hours to partially dissolve Si (Al-Degs et al. 2001). The mixture was immediately added into 100 mL of $FeCl_2$ solutions of differing concentrations and stirred and oxidized in air at room temperature for 24 hours. The mixture was then centrifuged to remove the supernatant. The solid obtained through centrifugation was introduced into 100 mL of NaOH solution, then mixed and oxidized in air at room temperature overnight. The mixture was then centrifuged to remove excess NaOH. The solid obtained through centrifugation was washed with distilled water and oxidized in air to continue the $Fe(OH)_2$ oxidation and the removal of excess NaOH. The mixture was dried at one of three different temperatures for 24 hours and then stored in a desiccator at room temperature.

Experiments were conducted to investigate the effects of each of three formation conditions ($FeCl_2$ concentration, NaOH concentration, and drying temperature) on the crystallinity of Si-containing ferrihydrite. To investigate the effect of $FeCl_2$ concentration, ferrihydrite-modified diatomite was produced employing different $FeCl_2$ concentrations (0.5 M, 1 M, 1.5 M, 2 M, and 2.5 M) in the method described above, but with NaOH concentration (6 M) and drying temperature (50 °C) held constant. The products of this procedure were named 0.5-FHMD, 1-FHMD, 1.5-FHMD, 2-FHMD,

and 2.5-FHMD. To investigate the effects of NaOH concentration, ferrihydrite-modified diatomite was produced employing different NaOH concentrations (3 M, 4 M, 5 M, and 6 M), but with $FeCl_2$ concentration (1 M) and drying temperature (50 °C) held constant. The products of this procedure were named 3NaOH-FHMD, 4NaOH-FHMD, 5NaOH-FHMD, and 6NaOH-FHMD. Similarly, ferrihydrite-modified diatomite produced using constant $FeCl_2$ (1 M) and NaOH (6 M) concentrations was dried at different temperatures (50 °C, 300 °C, 500 °C, and 900 °C). The products of this procedure were named 1-FHMD, 1FHMD-300, 1FHMD-500, and 1FHMD-900.

4.1.2 Preparation of Reference Materials

Standard reference materials

Standard reference materials were purchased from chemical suppliers. Ferrous chloride tetrahydrate ($FeCl_2.4H_2O$) was purchased from EM Science, Germany. Ferric chloride 6-hydrate ($FeCl_3.6H_2O$) was purchased from Mallinckrodt Baker Inc., USA. Anhydrous crystalline ferric oxide (Fe_2O_3) was purchased from Fisher Scientific, USA. Potassium phosphate dibasic (K_2HPO_4) was purchased from EM Science, Germany. Silicic acid (H_2SiO_3) was purchased from Sigma Aldrich, USA.

Synthetic Si-containing ferrihydrite

Synthetic Si-containing ferrihydrites were prepared according to Seehra et al. (2004). Appropriate amounts of $Na_2SiO_3.9H_2O$ were added to 100 mL of 0.1 M $Fe(NO)_3.9H_2O$ solution to yield molar ratios pf 0.1 to 0.5 according to $x = Si/(Si + Fe)$. Ammonium hydroxide was then slowly added to this solution to bring the pH to 10. The precipitate was filtrated and washed using distilled water followed by oven drying at 50 °C. The product was then ground to a fine powder. These synthetic Si-containing ferrihydrites of differing molar ratios were named 0.1-FHYD, 0.2-FHYD, 0.3-FHYD, 0.4-FHYD, and 0.5-FHYD.

Synthetic hydrated iron phosphate

Synthetic hydrated iron phosphates ($FePO_4.2H_2O$) were prepared according to Reale et al. (2003). 100 mL of 0.027 M H_3PO_4 solution and 100 mL of 0.009 M $FeCl_3$ H_2O were added to a boiling flask and refluxed at boiling temperature with continuous stirring. The reaction mixture was refluxed at pH=3-4 for two days to produce $FePO_4.2H_2O$. The pH was adjusted by 0.04 M sodium hydroxide or 0.5 M hydrochloric acid solution, respectively. After two days of refluxing, a fine and well-crystalline yellowish powder ($FePO_4.2H_2O$) was obtained.

4.1.3 Characterization of Ferrihydrite-Modified Diatomite

Iron content of ferrihydrite-modified diatomite

The iron content of FHMD was determined by atomic absorption spectroscopy (AAS) by using Perkin-Elmer Model 5000 atomic absorption spectrophotometer (PerkinElmer Life And Analytical Sciences, Inc., USA). Prior to the AAS analysis, the FHMD was immersed in 6 M hydrochloric acid at 40 °C overnight to dissolve the deposited ferrihydrite.

X-ray diffraction (XRD) studies

Mineralogy of raw diatomite and FHMD was characterized by powder X-ray diffraction (XRD) analysis using a Model APD 3520 X-ray diffraction unit (Philips, Eindhoven, Netherlands), Cu Kα radiation (50 kV, 100 mA). The powdered samples were smeared on a glass slide with methanol and dried at room temperature, then scanned from 10° to 90° (2θ) with a step size of 0.05°.

Scanning electron microscope (SEM) studies

Samples of raw diatomite and FHMD were scanned with a JEOL JSM-840A scanning electron microscope. The samples were first mounted flat, using carbon tape, and then

modified with 30 nm of gold using a sputter coater. The working distance was set to 17 mm and the accelerating voltage was set at 20 kV.

Transmission electron microscope (TEM) studies

The microstructure of raw diatomite, synthetic Si-containing ferrihydrite, and FHMD was studied by TEM using a Philip CM10 instrument. TEM samples were dispersed in a few drops of high-purity water by ultrasonication, and a droplet of the sample was placed over a holey carbon coated copper grid and subjected to imaging.

Brunauer-Emmett-Teller (BET) analyses

Textural parameters of raw diatomite, 0.5-FHMD, 1-FHMD, 1.5-FHMD, 2-FHMD, and 2.5-FHMD such as BET surface area, pore volume, and pore size distribution were determined by using the BET method and assuming the cross-sectional area of nitrogen molecule to be 0.162 nm^2. Nitrogen adsorption isotherms of the adsorbents were determined at 77 K using Micromeritics adsorption equipment (Model ASAP 2000, manufactured by Micromeritics Instruments Inc., Norcross, GA, USA). The mass of the samples was around 0.2 g. Before nitrogen adsorption, all samples were degassed at 473 K for four hours in a vacuum of 5×10^{-4} atm to remove all adsorbed moisture from the sample surface and pores.

Surface charge

The surface charge of raw diatomite and FHMD was determined by a potentiometric titration method (Chen et al. 1996; Chen and Lin 2001). 10 g/L of diatomite and FHMD in a solution with an ionic strength of 0.05 M NaCl were first placed in the shaker for 24 hours at room temperature. Titrations were then carried out by using 0.1 M hydrochloride acid and then 0.1 M sodium hydroxide, and the pH was measured throughout the titration process. The volume (mL) of acid or base needed to change the pH from 3 to 12 was recorded. Titrations were conducted in duplicate and the results reported as an average.

X-ray Absorption Near-Edge Structure Spectroscopy (XANES)

XANES experiments were carried out at the Canadian Light Source (CLS) (Saskatoon, Canada) using the Spherical Grating Monochromator (SGM) and Variable Line Spacing-Plane Grating Monochromator (VLS-PGM) beamlines. The SGM covers a photon energy range of 250-2000 eV, and was used for the Si K-edge and Fe L-edge measurements; the Si L-edge and P L-edge spectra were recorded using the VLS-PGM beamline (5.5-250 eV) (Regier et al. 2007; Hu et al. 2007). The photon energy resolution at the Fe, Si, and P L-edge was set at 0.1 eV and at the Si K-edge was set at 0.2 eV. Powder samples were mounted on the stainless-steel sample holder using double-sided, electrically conductive, carbon adhesive tape.

The XANES data were recorded simultaneously in total-electron-yield (TEY) mode and fluorescence-yield (FY) mode at ambient temperature using a microchannel plate (MCP) based detector. Multiple scans were recorded for each sample to improve the signal-to-noise ratio. The XANES data were normalized using the absorption current that passed through a high transmission (90%) gold mesh (SGM) and Ni mesh (VLS-PGM) inserted into the X-ray path. The pre-edge background was subtracted from the complete data set by using the data analysis program BAN (version 4.84b) obtained from Tolmar Instruments (Hamilton, Canada). The intensities of peaks in the Si K-edge and Fe L-edge spectra are given in relative units and correspond to their areas. These data were obtained by means of a peak-fitting analysis using a data analysis program ATHENA (version 9). The spectra were fitted with an arctangent background step function, and peaks with convoluted Lorentzian and Gaussian profiles. An arctangent function is used to model the step function of the data and Gaussian or Lorentzian function is used to model the features of the XANES spectra. The step function is centered at the E_0 value for the data. To add peak functions, an energy value is specified for the centroid and a line shape chosen from the menu. As soon as lineshapes are selected, the fit is recalculated automatically, so the simulation of the XANES spectra evolves as new

lineshapes are added. The best fitting results were determined according to their chi-square values.

4.2 Water and Sediment Samples

Collection of water and sediment samples

Water samples were collected from Jackfish Lake near North Battleford, Saskatchewan, Canada, in October 2006 using an *in situ* subaqueous peristaltic pump with an extended silicone sampling tube lowered to the desired depth. The peristaltic pump was operated at a flow rate of 1 L/min and was powered by a battery. The sampling tube was flushed prior to sample collection by pumping water from the sampling depth for at least 5 minutes. The outflow of the pump was directed into tanks that had been pre-cleaned with hydrochloride acid then rinsed with lake water from the sampling depth a minimum of three times. All samples were stored at 4 ºC.

Surface sediment samples (0-10 cm) were collected from the center of Jackfish Lake with a 225 cm^2 Eckman grab, which performed well on the type of sediment present. The material was stored in polyethylene containers, which were filled completely to minimize air space, in the dark at 2°C until use in experiments and subsequent analyses.

Description of sampling site

Jackfish Lake is a popular recreational lake located approximately 40 km north of North Battleford (53º7’30’’N, 108º15’2’’W), providing swimming, boating, and fishing opportunities to cottage owners and visitors (Evans 2005). The Battlefords Provincial Park and Meota Regional Park are both located on Jackfish Lake. Jackfish Lake is moderately large (surface area 62 km^2) and shallow (5.5 m maximum depth) (Evans 2005). Jackfish Lake is located in the Jackfish River Basin, which drains an area of approximately 3730 km^2 (Evans 2005). This gives Jackfish Lake a watershed to lake area ratio of 60.1. Agriculture development predominates in the Jackfish River Basin (Evans 2005). The lake experiences increased productivity most likely because of the agricultural activity in the Jackfish River Basin (Evans 2005). Table 4.1 summarizes the

major water quality characteristics of Jackfish Lake based on the laboratory analysis data.

Table 4.1 Characteristics of water sample collected from Jackfish Lake

Parameter	Value
Na (mg/L)	277
K (mg/L)	37
Dissolved chloride (mg/L)	93
Total hardness (mg/L)	1047
Total nitrogen (mg/L)	2.42
Total phosphorus (μg/L)	113.4
pH	8.48
Alkalinity (mg as $CaCO_3$/L)	256.5
Dissolved Si (mg/L)	1.44
Dissolved Fe (mg/L)	0.16
Diatom population (cells/mL)	218750

Sediment water content

Sediment water content was determined by oven-drying ~3-5 g of wet sediment for 6 hours (or to constant weight) at 105 ºC (Håkanson and Jansson 1983). The sediment water content was calculated by the following equation:

$$W = \frac{(W_t - W_s)}{W_t} \times 100\% \qquad [4.1]$$

where *W is* the water content in %, W_t is the total wet weight in g, and W_s is the dry weight of sediment in g. This definition provides the sediment water content from close to 0 (rock) to 100% (pure water).

4.3 Phosphorus Adsorption

Adsorption isotherm

A mass of 0.05 g of adsorbent (raw diatomite and FHMD) and 100 mL of standard K_2HPO_4 solutions (0, 3, 6, 10, 15, 20, 25, 30, 35, 40 mgP/L) were added to 125 mL flasks and shaken at 200 rpm at initial pH values of either 4 ± 0.2 or 8.5 ± 0.2 for 72 hours at room temperature. The ionic strength was adjusted using 0.1 M NaCl. The pH 8.5 condition represented water from Jackfish Lake. The pH 4 condition represented an extreme situation should the lake pH drop to 4 or less due to acid rain. The pH of the solutions was adjusted with HCl or NaOH solution and using a pH meter. Preliminary experiments indicated that 72 hours were required for adsorption to reach the equilibrium. After 72 h, the solution was filtered through a 0.45 µm Whatman® cellculose nitrate sterile membrane filter and then the concentration of the residual phosphate, Ce, was measured by the ascorbic acid method (4500-P E, APHA). The amount of adsorbed phosphate ions at equilibrium, q_e (mg P/g), is computed as follows:

$$q_e = \frac{(C_0 - C_e) \times V}{m}, \qquad [4.2]$$

where C_0 and C_e are the initial and equilibrium phosphate concentrations (mgP/L), respectively; V is the volume of the solution (L); and m is the mass of adsorbent (g). Each experiment was performed three times under identical conditions.

Selective phosphate adsorption

A stock solution of 1 mM chloride (Cl^{-1}), 1 mM hydrogen phosphate (HPO_4^{2-}), 1 mM sulfate (SO_4^{2-}), 1 mM nitrate (NO_3^{-1}), and 1 mM hydrogen carbonate (HCO_3^{-1}) was made by dissolving 58.5 mg of sodium chloride (NaCl), 142 mg of sodium hydrogenphosphate (Na_2HPO_4), 142 mg of sodium sulfate (Na_2SO_4), 85 mg of sodium nitrate ($NaNO_3$), and 84 mg of sodium hydrogen carbonate ($NaHCO_3$), respectively, in deionized water. 50 mL of the stock solution and 0.1 g of FHMD were introduced into a 125 mL flask, and the solution stirred for two hours at room temperature. The solution was then suction filtered using a 0.45 µm Whatman® cellculose nitrate sterile membrane filter, and the adsorbent washed with 100 mL of deionized water. The phosphate ion

content of the filtrate was measured by the ascorbic acid method, and the amount of phosphate adsorbed onto the FHMD determined from the difference in phosphate ion concentration before and after adsorption. The amount of other anions adsorbed onto the diatomite was measured using standard methods that are described in Section 4.5.

X-ray Absorption Near-Edge Structure Spectroscopy (XANES)

K-edge XANES spectra of P adsorbed onto FHMDs (0.5- to 2.5- FHMD) and P adsorbed on synthetic ferrihydrites (0.1- to 0.5-FHYD) were obtained at the Canadian Synchrotron Radiation Facility (CSRF) situated at the 1 GeV Aladdin storage ring, University of Wisconsin-Madison. The P K-edge spectra were obtained on the double crystal monochromator (DCM) beamline, covering the region of 1500-4000 eV. Air-dried, ground samples were analyzed by placing a small amount of sample on a piece of graphite tape and transferring it into the ultra high vacuum (UHV) chamber. The photon resolution at the P K-edge was less than 0.8 eV. The CSRF DCM is a UHV beamline, so it was possible to collect both FY and TEY via a multichannel plate detector on powder samples. Multiple scans (3-5) were averaged to improve the signal to noise ratio. The pre-edge background was subtracted from the complete data set using the data analysis program BAN (version 4.84b) obtained from Tolmar Instruments (Hamilton, Canada).

4.4 Application of Ferrihydrite-Modified Diatomite for Phosphorus Control

4.4.1 Batch-Scale Experiments

Phosphorus removal from lake water

Batch experiments for measuring P removal were carried out in 1 L flasks, using 500 mL of the original lake water sampled. FHMD was mixed into the lake water at different concentrations (0, 50, 100, 150, 200, 250, 300, 350, 400, 450, and 500 mg/L), then mixed at 200 rpm for 30 min for particulate destabilization, then at 50 rpm for 30 min for particulate aggregation (HDR Engineering 2001). The mixture was set aside for 1 hour. The mixture was then mixed again at 200 rpm for 24 hours at 25 °C under a

light/dark rhythm of 16 hour light/8 hour dark which is a common light/dark regime for plant/algal growth (Bowsher et al 1991). The lighting was provided by fluorescent lights at a fluce rate of 200 µmol $m^{-2}s^{-1}$. The mixture was then filtered through a 0.45 µm Whatman® cellculose nitrate sterile membrane filter. Total phosphorus (TP) in the filtrate was determined by persulfate digestion (4500-P B, APHA) and ascorbic acid (4500-P E, APHA) methods. Si concentrations were measured by molybdo-silicate (D859 ASTM). Diatom concentrations in the unfiltered sample were determined by a phytoplankton counting technique (10200 F, APHA).

Sedimentation experiment

The sedimentation experiments were performed in glass cylinders (6 cm diameter, 43 cm height). After the addition of 400 mg/L of raw diatomite and FHMD into 1 L of lake water, respectively, the samples were mixed at room temperature for 24 hours using the same conditions as described above for P removal experiments. Subsequently (after the mixing period), water samples were taken at defined time intervals (0, 1, 2, 4, 6, 8, 12, 22, 48, 72, 94, 96, 120, and 144 hours) from 5 cm below the surface for photometric turbidity measurements. In order to make this experiment's results comparable to literature data, the water samples were collected at the 5 cm below the water surface, which followed the sampling procedure outlined by Deppe and Benndorf 2002. Experiments were performed twice under identical conditions.

Anoxic incubation of ferrihydrite-modified diatomite treated sediments

This experiment was performed to determine the optimum amount of FHMD for inactivation of sediment P. Sediment obtained from Jackfish Lake was transferred to a glass cylinder (6 cm diameter, 43 cm height) to form a 4 cm sediment layer. One litre of lake water was mixed at 200 rpm with FHMD at different concentrations (0, 300, 400, 500, and 600 mg/L) for 24 hours, then siphoned very slowly into the glass cylinders with sediments. Experiments were conducted in duplicate, for a total of 10 glass cylinders. The two cylinders without FHMD addition (0 mg/L) served as controls. After three days time for sedimentation, all 10 cylinders were sealed by stoppers and

incubated in the dark at room temperature under anoxic conditions for 30 days. To further exclude light, cylinders were wrapped with aluminium foil. Anoxic conditions were established by sparging the overlying water in each cylinder with high-purity nitrogen gas. Duplicate 50 mL water samples were collected from the cylinders on days 1, 5, 12, 17, 22, and 30 after the start of the experiment and analyzed for TP and SRP. The P composition of control and FHMD treated sediments was determined by sequential extraction on day 30. The sequential P extraction technique is described in Section 4.5 and presented in Table 4.2 and Figure 4.3.

Anoxic incubation of ferrihydrite-modified diatomite and alum treated sediment

This experiment was performed to investigate P inactivation by FHMD in the presence of alum. Sediment obtained from Jackfish Lake was transferred to a glass cylinder (6 cm diameter, 43 cm height) to form a 4 cm sediment layer. One litre of raw lake water was mixed with 400 mg/L of FHMD at 200 rpm for 24 hours, then siphoned very slowly into the glass cylinders with sediment. After three days time for sedimentation, alum solutions with logarithmic ratios of Al to mobile P + coprecipitated P of 0.5, 0.8, 1.1, 1.4 and 1.7 were directly introduced to the top of the sediments. The alum solution was buffered with 1 M $NaHCO_3$ to reach a pH of 6. Each of the five alum conditions were conducted in duplicate, and two cylinders did not receive the alum solution and acted as controls, for a total of 12 glass cylinders in this experiment. All 12 cylinders were sealed and incubated in the dark at room temperature under anoxic conditions for 30 days. The cylinders were wrapped with aluminium foil to further exclude light. Anoxic conditions were established by sparging the overlying water in each cylinder with high-purity nitrogen gas. Duplicate 50 mL water samples were collected on days 1, 5, 12, 22, and 30 after the start of the experiment and analyzed for TP and SRP. Sequential extraction of sedimentary P was performed on day 30.

Oxic and anoxic agitation experiment

The purpose of this experiment was to determine the optimum amount of gypsum and investigate P release in the agitation procedure. Sediment samples obtained from

Jackfish Lake were transferred to a 1 L flask to form a 3 cm sediment layer. One litre of lake water was mixed at 200 rpm with 400 mg/L of FHMD for 24 hrs, then this treated lake water was slowly siphoned to the 1 L flask to avoid disturbing the sediment. After a settling period of three days, gypsum was spread into the 1 L flasks to form layers of 0.5 cm, 0.8 cm, 1 cm, and 1.2 cm depth. Each gypsum depth was conducted in duplicate. Gypsum was not added to two flasks that acted as controls. Ten flasks were agitated under oxic condition and 10 flasks were agitated under anoxic conditions, respectively. Oxic conditions were maintained by introduction of air; anoxic conditions were established by introduction of pure nitrogen. The flasks were wrapped with the aluminium foil to exclude light. The flasks were sealed by stoppers and intermittently agitated in the dark at 30ºC. Samples were agitated at 60 rpm from 0-12 hours, at 100 rpm from 24-36 hours, and 130 rpm from 48-60 hours. The samples were allowed to settle in the intervals between (12-24 hours, 36-48 hours) and after (60-72 hours). Samples (10 mL) were taken every 3 hours during agitation and less frequently during settling intervals. After 72 hours, the SRP and turbidity of the lake water were analyzed. Water samples for SRP analysis were taken from a depth of 2 cm below the water surface; water samples for turbidity analysis were taken from a depth of 2 cm above the sediment. The agitation procedure is described in Figure 4.1.

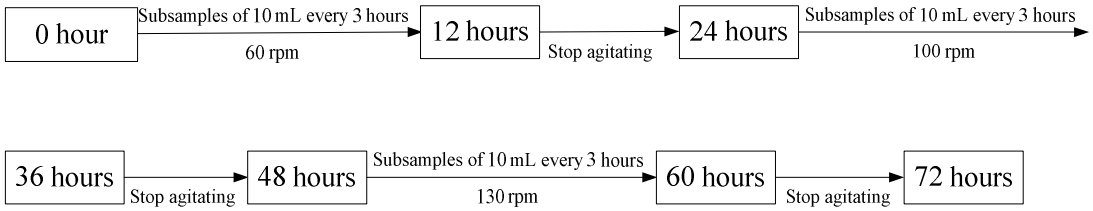

Figure 4.1 Agitation procedure to test phosphorus release and sediment resuspension

Oxic and anoxic incubation of ferrihydrite-modified diatomite and gypsum treated sediment

Sediment obtained from Jackfish Lake was transferred to four glass cylinders (6 cm diameter, 43 cm height) to form a 4 cm sediment layer. One litre of raw lake water was

mixed with 400 mg/L of FHMD at 200 rpm for 24 hours, and then the mixture very slowly siphoned into the glass cylinders so as not to disturb the sediment. After three days sedimentation time, gypsum was added to form a 0.8 cm layer. The cylinders were sealed by stoppers. Two pairs of cylinders were wrapped in aluminum foil and incubated in the dark at 30ºC under oxic and anoxic conditions, respectively, for 30 days. Water samples were collected in 50 mL aliquots from the overlying water in the cylinders on days 0, 6, 10, 16, 21, and 30 and analyzed for TP and SRP. Sequential P extraction was performed on day 30 to determine the sedimentary P composition.

4.4.2 Bench-Scale Experiments

Phosphorus control in an artificial aquarium

The purpose of these experiments was to test the effects of two techniques—P coprecipitation by FHMD and sediment sealing by FHMD and gypsum—on controlling P in an artificial aquarium over a 120 day time period. Conditions in the aquarium were designed to favour P release, with DO levels less than 1 mg/L and frequent vertical mixing in the entire water column. Three artificial aquariums were established in the Environmental Laboratory. One was used as a control to which no FHMD and gypsum were added. FHMD and gypsum were added to two test aquariums to control P. Artificial aquariums ran for at least 120 days in an environmental chamber in the Environmental Laboratory.

The three tanks used in this experiment were 45 cm in diameter and 100 cm tall. Three holes were drilled into the tanks at depths of 20, 55 and 80 cm. These holes were fitted with male pipe adapters, connected with tubing, and primarily used as sampling ports. Sediment from Jackfish Lake was transferred to the three aquariums to a depth of ~15 cm. Two hundred and forty litres of Jackfish Lake water was mixed at 200 rpm with 400 mg/L of FHMD for 24 hours in an auxiliary tank. Water was slowly siphoned to the aquariums to avoid disturbing the sediment to a final depth of ~80 cm. The control aquarium received 120 L of untreated lake water; the remaining two aquariums received 120 L of FHMD treated lake water. The aquariums were left for three days

during which time particulates such as FHMD, living particles, and detritus particles settled onto the sediment. A 0.8 cm deep gypsum layer was then evenly spread in the two test aquariums.

The temperature in the environmental chamber was 11°C, to simulate the average daily temperature between April 1 and June 30 of the Saskatoon airport from 1980 to 2000. This temperature was also in the optimum temperature range of 7 to 12°C for carbon fixation by diatoms. A light/dark rhythm of 16 hour light/8 hour dark was established with a light intensity of 220 µmol m^{-2} s^{-1}. Light penetrated the aquariums from the top opening only, not from the aquarium sides. Relative humidity was kept at 85-95% in the chamber to avoid the effects of evaporation. To simulate anoxic conditions caused by temporary thermal stratification, pure nitrogen was introduced to 1 cm above the sediment to maintain DO levels of less than 1 mg/L. To simulate sediment resuspension induced by wind and wind-generated gravity waves, a metal grid oscillating vertically for 15 minutes per day within the water column was introduced into all three aquariums. The grid was made of a steel 7×7 cm mesh and was driven by a motor to attain a settling velocity of 9.2 cm/s. The oscillation frequency of the grid was 90 rpm. In its resting position, the top of the grid was 5.5 cm above the top of the sediment and the lower edge of the grid was 2 cm above the top of the sediment. The stroke amplitude of the oscillation was 7 cm. The setup of an artificial aquarium is shown in Figure 4.2.

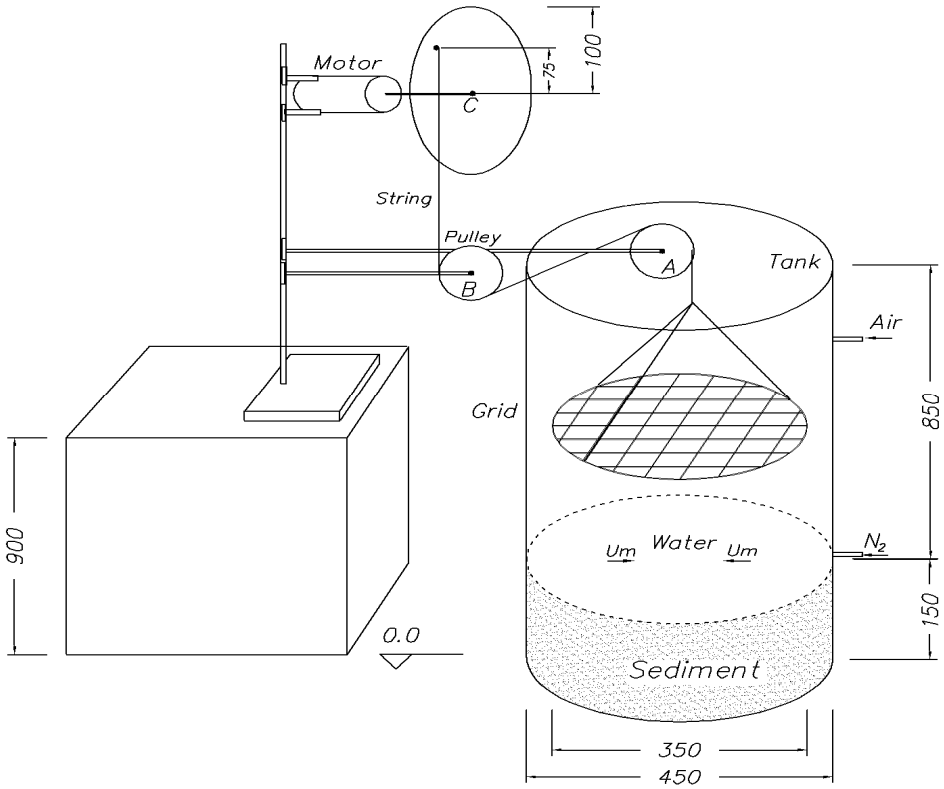

Figure 4.2 An artificial aquarium used to study phosphorus control by FHMD and gypsum (All length units in dimensions of mm)

The dissolved oxygen (DO) concentration of the water was measured each day prior to vertical oscillation. Water samples (150 mL) were taken immediately after vertical oscillation every four days from the top and bottom sampling ports, respectively. Water quality parameters such as pH, total alkalinity, total suspended solids (TSS), total phosphorus (TP), soluble reactive phosphorus (SRP), total kjeldahl nitrogen (TKN), and silicate (SiO_4^{-4}), sulfate (SO_4^{2-}), and diatom count were determined in duplicate for each water sample. The depth profile of P in sediment samples was tested by sequential P extraction.

4.5 Analytical Methods

Measurements of turbidity, dissolved oxygen (DO), pH and total alkalinity

The turbidity of the water samples was measured using a 2100 P Turbidimeter (Hach, USA). Dissolved oxygen (DO) concentration was measured with a SensION156 Portable pH/Dissolved Oxygen Meter (Hach, USA). pH measurements were carried out using a VWR Scientific Instruments, model 8000 pH-meter. Total alkalinity of water samples was measured following the titration method (2320 B., APHA 1992) and by using a pH-meter E512, Impulsomat E473 and Dosimat (Metrohm Herisau, Switzerland).

Measurements of phosphorus (SRP and TP), Silicate (SiO_4^{4-}), Fe, sulfate (SO_4^{2-}), Total Kjeldahl Nitrogen (TKN), nitrate (NO_3^{-1}), chloride (Cl^{-1}) and diatom

Soluble reactive phosphorus (SRP) in the overlying water was analyzed by the ascorbic acid method (4500-P E., APHA 1992); total phosphorus (TP) in the overlying water was measured with the ascorbic acid method after persulfate digestion (4500-P B., APHA 1992). Silicate was measured with the molybdosilicate method (4500-Si D., APHA 1992). SRP, TP, and Si were measured with the DR/4000U spectrophotometer (Hach, USA). Fe was measured by atomic adsorption as described in 3500-Fe B, Standard Methods (APHA 1992). Fe measurements were conducted with a Perkin-Elmer Model 5000 atomic absorption spectrophotometer (PerkinElmer Life and Analytical Sciences, Inc., USA). Sulfate (SO_4^{2-}) was measured by the automated methylthymol blue method (4500- SO_4^{2-} F., APHA 1992). Nitrate (NO_3^{-1}) was measured by the automated cadmium reduction method (4500- NO_3^{-1} F., APHA 1992). Chloride (Cl^{-1}) was measured by the potentiometric method (4500 – Cl^{-1} D., APHA 1992). Diatoms were quantified with the phytoplankton counting technique (10200 F., APHA 1992) by a Zeiss Axioskop microscope associated with Axiocam color digital camera (Carl Zeiss, Germany) whose resolution is sufficient to separate clearly FHMD from diatom.

Sequential phosphorus extraction

Sequential P extraction is widely used to determine different fractions of P in sediments (Petterson et al. 1988). The best example of early extraction schemes is presented by Chang and Jackson in 1957, who partitioned sediment P into labile P, aluminium-bound P, iron-bound P, calcium-bound P, reductant soluble P, occluded P, and organic P. The method of Chang and Jackson (1957) was further developed by several researchers. More recently, the need for better chemical characterization has been stressed to improve understanding of P exchange processes between sediment and water as well as the effects of environmental conditions such as pH, redox potential, and ionic strength on these processes. In the work of Hieltjes and Lijklema (1980), they separated sediment P into labile P (NH_4Cl-P), iron- and aluminium-bound P (NaOH-rP), calcium-bound P (HCl-P), and a residue P fraction. However, iron-bound P and aluminium-bound P were not separated in this sequential P extraction scheme, and organic P was not identified but rather included within NaOH-RP and/or the residue P fraction. In 1988, Psenner et al. presented a P fractionation scheme designed to separate water-soluble P (H_2O-P), P bound to iron and manganese hydroxide or reductant soluble P (BD-P), iron- and aluminium-bound P (NaOH-rP), calcium-bound P (HCl-P), and refractory P ($NaOH_{85}$-P). Rydin and Welch (1998) and Rydin (2000) developed Hieltjes and Lijklema's (1980) method with two modifications: an anoxic bicarbonate dithionite (BD) step and a digestion step added to the NaOH extraction. Thus, Rydin and Welch (1998) and Rydin (2000) separated sediment P into labile P(NH_4Cl-P), iron-bound P (BD-P), aluminium-bound P (NaOH-rP), organic P (NaOH-nrP), calcium-bound P (HCl-P), and a residue P fraction. Hansen et al. (2003) developed the P fractionation scheme presented by Psenner et al. (1988) with two modifications: 1.5 mL 2 M H_2SO_4 added to the NaOH extraction step to determine humic acid-bound P and a sediment combustion step to determine the residue P fraction. These sequential P extraction schemes are summarized in Table 4.2.

After reviewing the modifications of the sequential P fractionation by Hieltjes and Lijklema (1980), Psenner et al. (1988), Jensen and Thamdrup (1993), Rydin & Welch (1998), Rydin (2000), and Hansen et al. (2003), the P extraction scheme proposed by Jensen and Thamdrup (1993) was used in the research in this thesis. Approximately 1 g of wet sediment was subsampled and placed into a 40 mL polyethylene centrifuge tube. Different fractions of P in the sediment were extracted according to the scheme described in Figure 4.3. Samples of the extracts were centrifuged for 10 min at 3000 rpm after which the supernatants were filtered through a 0.45 µm membrane filter. Phosphorus was measured following the methods described above. In step 1, 25 mL of 0.46 M N_2-purged NaCl solution was added under N_2-atmosphere and 1 mL of 1 M H_2SO_4 was added into tubes to prevent coprecipitation of phosphate with iron (Fe) and manganese (Mn) and to preserve the sample. Step 1 was intended to extract the pool of loosely adsorbed P (labile P). The bicarbonate dithionite solution (BD-reagent) was made by adding 0.11 M $Na_2S_2O_4$ into a stock solution of 0.11 M $NaHCO_3$. In step 2, one hour aeration was conducted to oxidize the remaining dithionite. The addition of 1 M H_2SO_4 and one hour aeration led to the formation of elemental sulphur, which turned the solution milky. However, the sulfur precipitates within a few days and then the clear solution was tested for SRP. Step 2 was intended to extract Fe-bound P. Steps 3 and 4 were handled under aerobic conditions. Step 3 was intended to extract primarily relatively stable P (Al-bound P) and organic P. Step 4 was used to extract Ca-bound P such as apatite. In the last step the sediment pellet was ignited at 520 °C for two hours and subsequently boiled for 10 minutes in 1 M HCI. The residual phosphorus left in the sediment was extracted. Residue P represented the more refractory P pool.

Table 4.2 Sequential extraction schemes for determining the fractional composition of sediment phosphorus

	Extraction	Proposed fraction
Chang and Jackson (1957)	NH_4Cl 1 M	Labile P
	NH_4F 0.5 M pH 8.2	Al-bound P
	NaOH 0.1 M	Fe-bound P
	HCl 0.5 M	Ca-bound P
	CDB	Reductant-soluble P
	NaOH	Refractory P
Hieltjes and Lijklema (1980)	NH_4Cl 1 M pH 7	Labile P
	NaOH 0.1 M	Fe- and Al-bound P
	HCl 0.5 M	Ca-bound P
Psenner et al. (1985)	H_2O	Water-soluble P
	DB 0.11 M 40 ºC	Reductant-soluble P
	NaOH 1 M	Fe-and Al-bound P
	HCl 0.5 M	Ca-bound P
	NaOH 1 M 85 ºC	Refractory P
Rydin and Welch (1998)	NH_4Cl 1 M pH 7	Labile P
	DB 0.11 M	Fe-bound P
Rydin (2000)	NaOH 0.1 M	Al-bound P
	After digestion and minus "Al-P"	Organic P
	HCl 0.5 M	Ca-bound P
Hansen et al. (2003)	H_2O	Water-soluble P
	DB 0.11 M	Fe-bound P
	NaOH 0.1 M	Al-bound and humic acid-bound P
	H_2SO_4 2 M	Humic acid-bound P
	HCl 0.5 M	Ca-bound P
	Sediment combustion 520 ºC	Residue P
Jensen and Thamdrup (1993)	NaCl 0.46 M	Labile P
	DB 0.11 M and 1 hour aeration	Fe-bound P
	NaOH 0.1 M	Al-bound P
	After digestion and minus "Al-P"	Organic P
	HCl 0.5 M	Ca-bound P
	Drying 105 ºC, ignition 520 ºC, 1 M HCl and boiling 10 min	Residue P

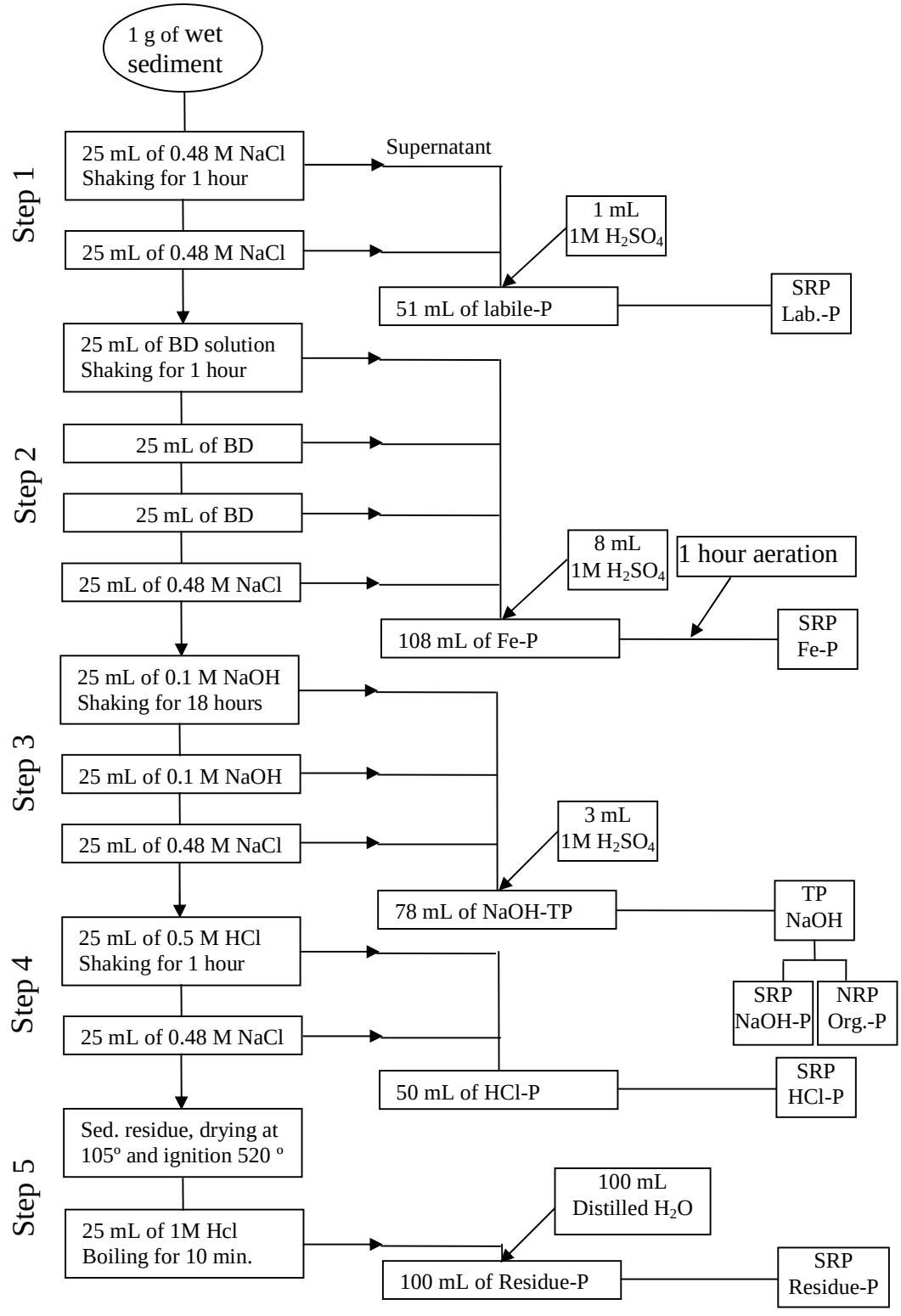

Figure 4.3 Sequential extraction scheme for phosphorus fractions in sediment

Chapter 5 – Results and Discussions

5.1 Characterization of Ferrihydrite-Modified Diatomite

5.1.1 X-Ray Diffraction

Powder X-ray diffraction (XRD) phase analysis is a method which can directly identify ferrihydrite in amorphous materials (Loan et al. 2002). Ferrihydrite displays a range of XRD patterns; the least crystalline ferrihydrite exhibits two broad peaks, defined as 2-line ferrihydrite, and the more crystalline ferrihydrite exhibits six broad peaks, defined as 6-line ferrihydrite. The transformation from 2-line ferrihydrite to 6-line ferrihydrite is characterized by decreases in surface area and density of hydroxylated surface sites (Kukkadapu et al 2003). As shown in Figure 5.1, the two reflections at 35.55°2θ (0.252 nm) and 64.3°2θ (0.145 nm) found in the XRD pattern of FHMD indicate that the ferrihydrite deposited into the diatomite is the least crystalline (2-line) ferrihydrite, which has a higher surface area and site density than other iron (III) oxides. This result agrees with previous work on the 2-line ferrihydrite identification (Janney et al. 2000; Pan et al. 2006). The same sample was analyzed by the AAS method, and the diatomite surface was found to be loaded with 0.24 g Fe/g of 2-line ferrihydrite.

In the XRD pattern of raw diatomite shown in Figure 5.1, a broad band is centered at 22.8°2θ (0.39 nm), which is the characteristic peak for amorphous SiO_2. This solo peak suggests that SiO_2 is the principal constituent of diatomite.

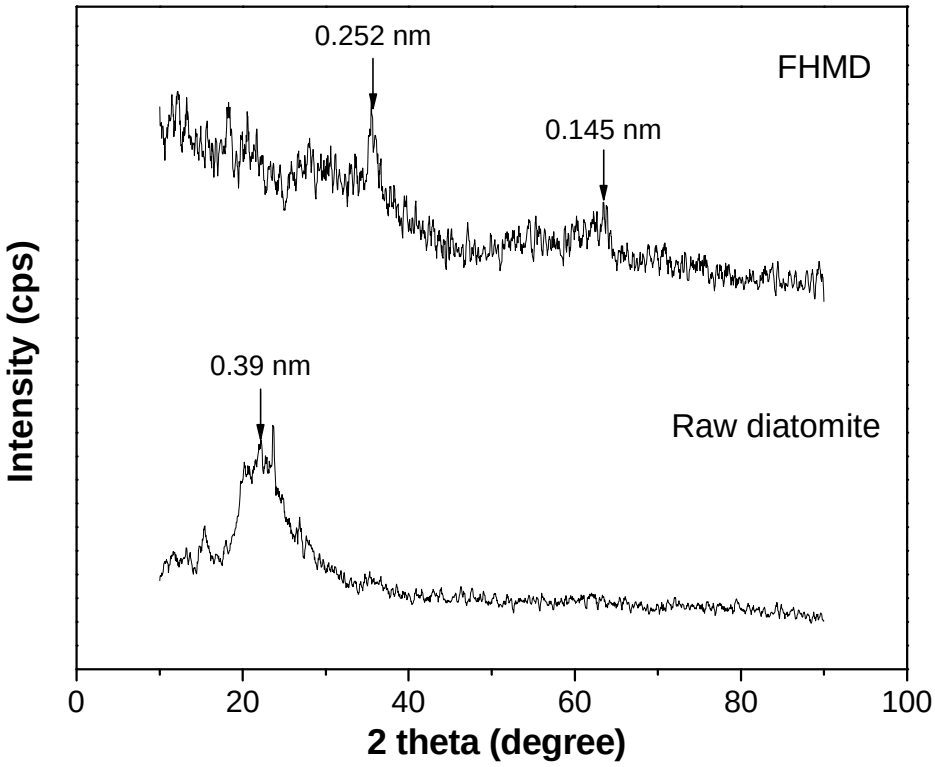

Figure 5.1 XRD patterns of raw diatomite and FHMD

5.1.2 Scanning Electron Microscopy

The surface of the diatomite was modified by the NaOH treatment and ferrihydrite deposition. Scanning electron microscopy (SEM) was employed to determine the differences in surface structure between raw diatomite and FHMD. Figure 5.2a shows an electronic micrograph of raw diatomite with 1800× magnification. There are two principal types of patterns in diatoms: (1) centric, with ribs radiating from a ring; and (2) pennate, with ribs extending out from both sides of a longitudinal element (Round et al. 1990). The raw diatomite obtained from Nevada mainly consists of the centric diatom particles, with only a small number of the pennate diatom particles. The centric diatom particles have a diameter of approximately 5-20 μm and a thickness of several microns. The pennate diatom particles have a length of about 12 μm. The micrograph shows the diatomite has a porous structure and a large void volume. It can be inferred from the SEM micrograph in Figure 5.2a that the high porosity is mainly caused by numerous

skeletal pores in the diatom particles and the interparticle pores between the diatom particles.

The SEM micrograph of FHMD at 1800× magnification reveals that raw diatomite frustules are surface modified and the original geometry of the pores is destroyed by the NaOH treatment and ferrihydrite deposition (Figure 5.2b). Initially, colloidal-size ferrihydrite (2-5 nm) is deposited into the macropores (>50 nm) and larger mesopores (7-50 nm) of the diatomite. Thereafter, additional ferrihydrite aggregates on the surface of the diatomite particles (Figure 5.2b).

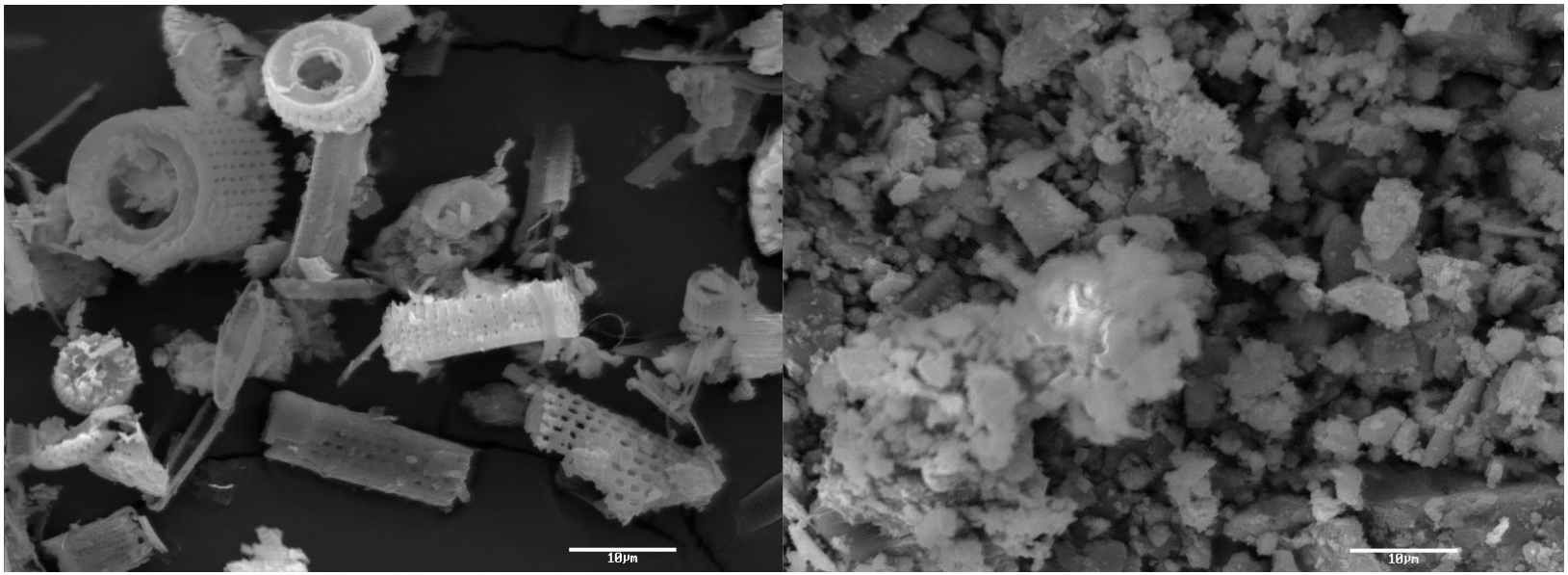

(a) (b)

Figure 5.2 Typical scanning electron micrographs for (a) raw diatomite and (b) FHMD (magnification 1800×)

5.1.3 Transmission Electron Microscopy

The TEM images of raw diatomite, synthetic ferrihydrite, and FHMD are shown in Figure 5.3, where raw diatomite and synthetic ferrihydrite serve as reference materials for the TEM analysis of FHMD. The TEM images of raw diatomite (Figure 5.3a), synthetic ferrihydrite (Figure 5.3b), and FHMD (Figure 5.3c) indicate that the structure of diatomite particles is destroyed by NaOH treatment and that ferrihydrite nanoparticles are deposited into the diatomite. Figure 5.3c and 5.3d are TEM images of FHMD. Figure 5.3d is representative of the majority of TEM findings of the same sample, and suggests that ferrihydrite not only deposits into the diatomite but also aggregates on the surface.

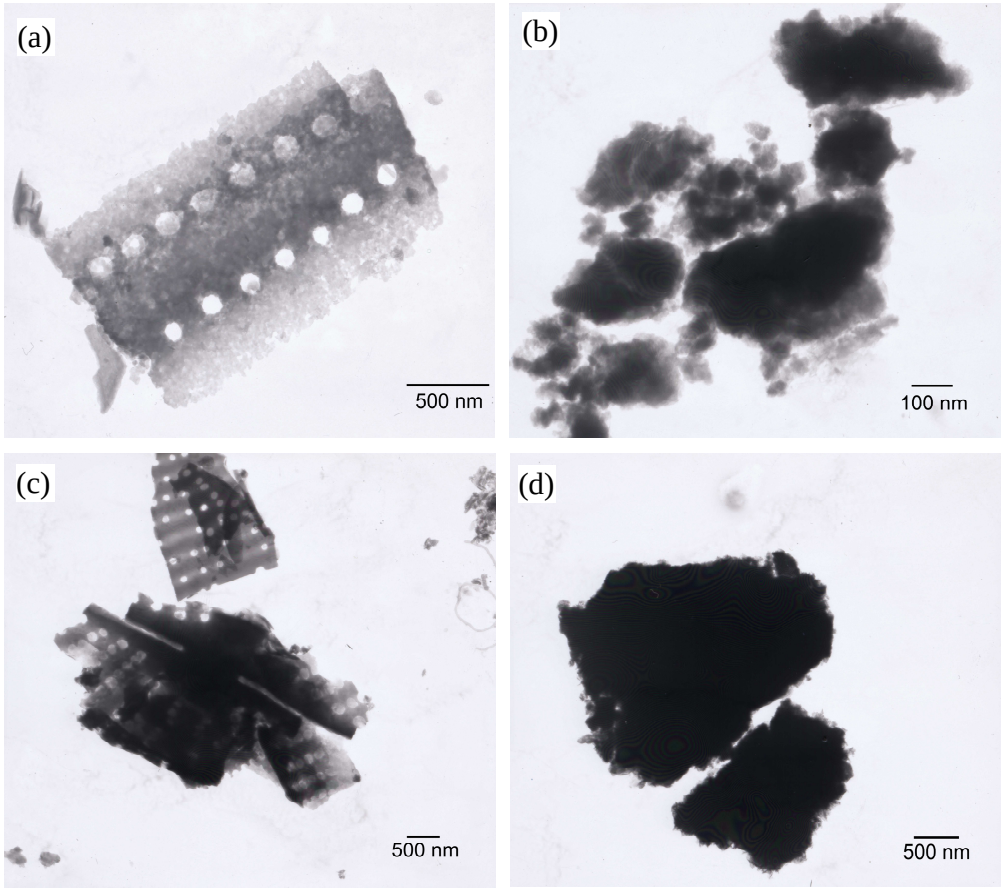

Figure 5.3 Typical TEM images of raw diatomite (a), pure ferrihydrite (b), and FHMD (c and d)

5.1.4 Si L-Edge XANES Spectroscopy

In the research conducted in this thesis, the surface SiO_2 of diatomite is altered by dissolution of Si^{4+} during the NaOH treatment; the dissolved Si^{4+} subsequently contributes to the formation of the ferrihydrite shell. The change in the chemical nature of Si can be estimated by Si $L_{3,2}$-edge XANES spectra. The common detection methods for XANES are to either measure the total electron yield (TEY) or the fluorescence yield (FY). The TEY method is surface sensitive with an effective sampling depth of ~5 nm; the FY method is bulk sensitive with an effective sampling depth of ~50-100 nm (Kawai et al. 2000; Hu et al. 2004; Cramer et al. 1998; Kasrai et al. 1993; Varlot et al. 2001). When the bulk and surface composition are the same, TEY and FY methods provide equivalent results. However, when bulk and surface composition are different, as in the case of FHMD, comparing the data from the two modes (TEY and FY) can provide very useful information.

Si $L_{3,2}$-edge XANES spectra from TEY and FY measurements of raw diatomite and FHMD after a pre-edge background removal are shown in Figure 5.4. These photon spectra recorded in the energy range from 102-115 eV are associated with the Si^{4+}oxidation state (in the form of SiO_2 or Si^{4+} ions). As shown in Figure 5.4, pre-edge peaks (*a* and *b*) come from spin-orbit splitting of the Si 2*p* level and can be assigned to $2p_{3/2} \rightarrow a_1$ (3*s*) and $2p_{1/2} \rightarrow a_1$ (3*s*) transitions, where a_1 (3*s*) is the antibonding orbital of high Si 3*s* characteristic. The splitting distance is calculated to be 0.6 eV, and is the same as the reported value for pure SiO_2 (Kasrai et al. 1993). The pre-edge peaks (*a* and *b*) in the TEY spectrum of raw diatomite correspond to those in the FY spectrum of raw diatomite, indicating that the Si chemical composition of both surface and bulk raw diatomite is SiO_2. However, in the TEY spectrum of FHMD, only one pre-edge peak (*d*) is observed though this peak is not quite resolved. Furthermore, this peak position is located at the low energy side compared with the spin-orbit doublets (*a* and *b*). The pre-edge peak and its position indicate that the Fe-Si bonding in the shell of ferrihydrite might be formed. The Si^{4+} is incorporated into the structure of ferrihydrite to form a stable 2-line ferrihydrite. The presence of the spin-orbit doublets (*a* and *b*) in the FY

spectrum of FHMD suggests that the bulk Si compound of FHMD remains as SiO_2. Thus, only SiO_2 on the surface of diatomite is dissolved in the NaOH solution and the bulk of the diatomite is preserved.

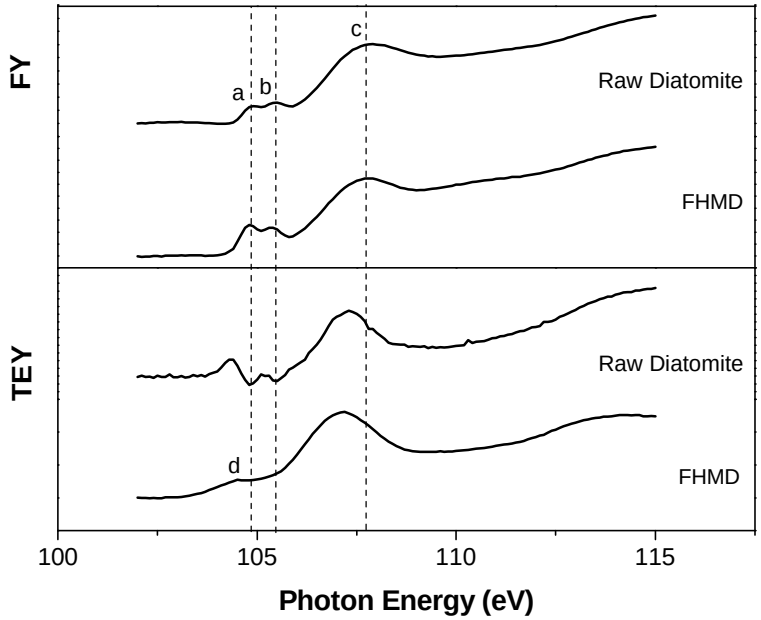

Figure 5.4 Si $L_{3,2}$-edge XANES TEY and FY spectra of raw diatomite and FHMD

5.1.5 BET Pore Size Distribution and Nitrogen Adsorption-Desorption Isotherm

The BET test was conducted to determine textural parameters, such as BET surface area, pore volume, pore area, and average pore diameter, of raw diatomite and FHMD. Results are tabulated in Table 5.1. As shown in Table 5.1, the BET surface area of FHMD is 211.1 m^2/g, which is 8.5-fold greater than diatomite. The surface area of the mesopore and micropore regions of diatomite was 22.11 and 1.78 m^2/g, respectively. These increased to 192.02 and 18.81 m^2/g, respectively, in the FHMD. However, the surface area of the macropore regions decreased from 0.89 m^2/g in the diatomite to 0.27 m^2/g in the FHMD. The total surface area increased, primarily due to increases in the mesopore and micropore regions. The increase of the mesopore area is due to the partial blockage of macropores (>50 nm) and larger mesopores (>7 nm) by colloidal-size (2-5 nm) ferrihydrite particles. Similarly, the increase of micropore area can be attributed to

pore blockage by colloidal-size ferrihydrite as well as additional micropores provided by microporous ferrihydrite. As shown in Figure 5.5, the increase in the mesopore and micropore regions is also demonstrated by differential pore size distributions in diatomite vs. FHMD. The differential pore size distribution is defined as $dV / d(\log D)$. The term V represents a cumulative pore volume at a specific average pore diameter. The distribution of FHMD pores exhibits only one maxima in the range from 2 to 4 nm, showing the dominance of the smaller pores. However, the raw diatomite has a much broader and flattened pore size distribution, which smoothly shifts toward large pore diameters without any significant peak. Calculated from the pore size distribution, the average pore diameter of FHMD is estimated to be 3.79 nm, while that of raw diatomite is 9.19 nm, as shown in Table 5.1. The average pore size (3.79 nm) of FHMD is just above the micropore size range, which can be also attributed to the blockage of macropores and mesopores by ferrihydrite nanoparticles.

Table 5.1 Summary of BET Data for Raw Diatomite and FHMD

Materials	BET surface area (m^2/g)	Macropore area (m^2/g)	Mesopore area (m^2/g)	Micropore area (m^2/g)	Total pore volume (cm^3/g)	Macropore volume (cm^3/g)	Mesopore volume (cm^3/g)	Micropore volume (cm^3/g)	Average pore diameter (nm)
Raw diatomite	24.77	0.89	22.11	1.78	0.062	0.0200	0.042	0.000564	9.19
FHMD	211.1	0.27	192.02	18.81	0.203	0.0057	0.190	0.00680	3.79

Nitrogen adsorption-desorption isotherm plots for raw diatomite and FHMD are provided as an inset in Figure 5.5. These plots show a hysteresis loop between the adsorption and desorption branches. Generally speaking, desorption branch cannot be superimposed over the adsorption branch (Lynch 2003). All the nitrogen adsorption-desorption isotherms are considered to be a typical type IV isotherms (IUPAC classification), which suggests that raw diatomite and FHMD are mesoporous materials. The plot of raw diatomite exhibits an H3 hysteresis loop, which is characteristic of aggregates of plate-like particles, while the plot of FHMD is considered to be a typical H2 hysteresis loop. The H2-type hysteresis corresponds to porous solids where the pore size distribution is not uniform and blockage of pores plays a significant role.

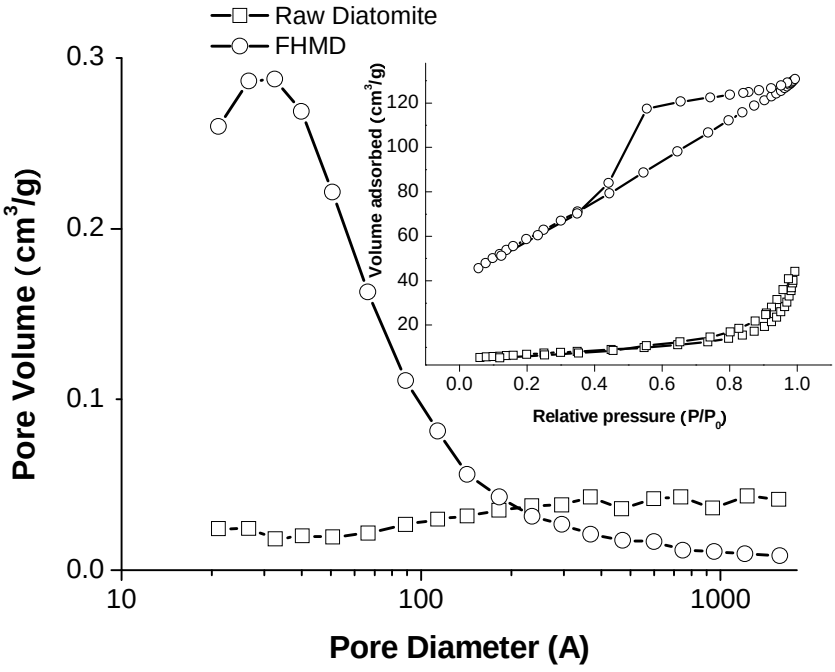

Figure 5.5 Differential pore size distribution and nitrogen adsorption-desorption isotherm plots of raw diatomite and FHMD

5.1.6 Surface Charge

Surface charge density σ (C/m^2) is determined by (Khraisheh et al 2004):

$$\sigma = \frac{(C_A - C_B + [OH^-] - [H^+])F}{Am} \quad [5.1]$$

where C_A and C_B are the concentrations of acid and base needed to reach a point on the titration curve in mol/L, $[H^+]$ and $[OH^-]$ are the concentrations of H^+ and OH^-, respectively, converted from pH to mol/L, F is the Faraday constant (96490 C/mol), *A* is the specific surface area in m^2/g, and *m* is the concentration of raw diatomite and FHMD in g/L.

The surface charge as a function of solution pH is shown in Figure 5.6. The titration curves illustrate that the surface charge decreases as the pH is increased. The intersection of the two curves with the x-axis gives the point of zero charge (pH_{PZC}), which was determined in this study to be at a pH of 5.8 for raw diatomite and 10 for FHMD. At pH_{PZC}, the total charge from cations and anions at the sample surface is equal to zero (Xiong and Peng 2008b). The pH_{PZC} of FHMD is greater relative to raw diatomite due to the the hydroxyl ligand bound to ferrihydrite. The surface charge is negative when the solution pH is above pH_{PZC} and becomes positive when pH is below pH_{PZC}. In this study, the pH of the lake water treated by FHMD was about 8.48 (Table 4.1). In the lake water, the surface charge of raw diatomite was negative, while that of FHMD was positive. As a result, a negatively charged surface of raw diatomite repels negative phosphate ions but the positively charged surface of the FHMD attracts phosphate ions.

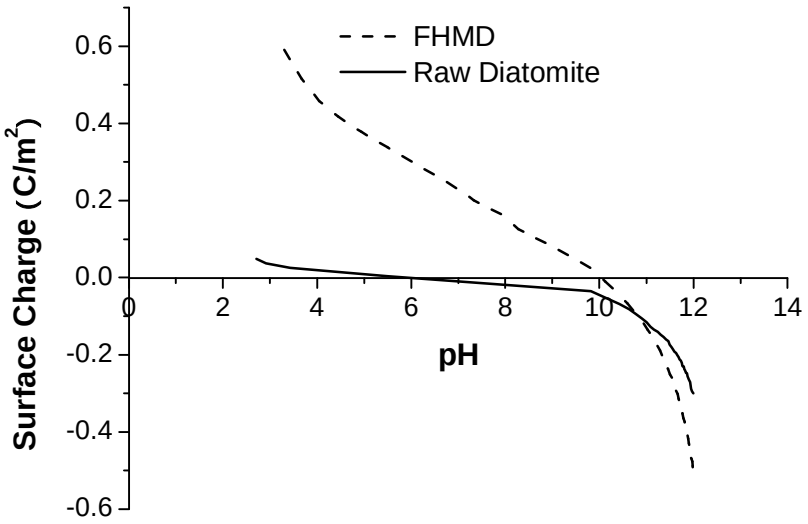

Figure 5.6 Surface charge density curves for raw diatomite and FHMD

5. 2 Optimum Synthesis of Ferrihydrite-Modified Diatomite

5.2.1 Effects of $FeCl_2$ Concentrations

Si-stabilized ferrihydrite is formed from Fe^{2+} oxidation in the presence of dissolved Si (Mayer and Jarrell 1996; Karim 1984). In the research, 100 mL of $FeCl_2$ solution at concentrations of 0.5, 1, 1.5, 2, and 2.5M were used to synthesize Si-containing ferrihydrite that deposits into the pores of diatomite. The Si/Fe molar ratio of the Si-containing ferrihydrite is expected to decrease with increasing iron amount from 0.5 to 2.5 M of $FeCl_2$ because the amount of dissolved Si is fixed when the same amount of NaOH is used (Xiong et al 2009). FHMD formed in different $FeCl_2$ concentrations were named 0.5-FHMD, 1-FHMD, 1.5-FHMD, 2-FHMD and 2.5-FHMD.

5.2.1.1 Si L3,2-edge XANES spectra

Si $L_{3,2}$-edge XANES FY and TEY spectra of pure amorphous SiO_2, raw diatomite (FN6), and ferrihydrite-modified diatomite (0.5- to 2.5-FHMD) are shown in Figures 5.7a and 5.7b. These XANES spectra are recorded in the energy range from 102-115 eV, which is associated with the Si^{4+}oxidation state in the form of SiO_2 or Si^{4+} ions (Li et al. 1996).

As shown in the FN6 spectrum (Figure 5.7a), pre-edge peaks (a_1 and a_2) located at 104.9 and 105.5 eV, respectively, come from spin-orbit splitting of the Si 2*p* level and can be assigned to $2p_{3/2} \rightarrow a_1$ (3*s*) and $2p_{1/2} \rightarrow a_1$ (3*s*) transitions, where a_1 (3*s*) is the antibonding orbital of high Si 3*s* characters. The broad and strong feature (*b* peak) located at 107.7 eV can be assigned to the $2p \rightarrow 3p$ transition. Although the $2p \rightarrow 3p$ transition is forbidden by the dipole selection rule, in the case of bulk SiO_2 the tetrahedral coordination and strongly electronegative oxygen atoms change the symmetry of the crystal field enough so that this transition becomes possible (Harp et al. 1989, Wu et al. 1998). Peak *b* has been designated as a dipole-allowed transition to the hybridized orbitals with Si 3s or 3d and O 2p characters in the spectrum of SiO_2 (Tsai et al. 2008, Mo and Ching 2001). Notably, strong orbital mixing is necessary for both assignments. Further theoretical work is required to determine the orbital characters and the degree of the mixing in these hybridized orbitals; Soldatov et al. (2000) reported the conduction band of stishovite (SiO_2) consisted of unoccupied Si *s*, *p*, *d* and O *p* electronic states. Peak *b* can also be assigned to the $2p \rightarrow 3p$ transition, as it follows the atomic energy order of 3*s*, 3*p*, and 3*d* orbitals (for example, the $1s \rightarrow 3p$ transition is at ~17 eV lower than the $1s \rightarrow 3d$ transition in the Si K-edge spectrum of SiO_2 (Wu et al. 1998). Figure 5.7d shows the intensity of peak *b* decreases with increasing $FeCl_2$ concentration.

The positions of peaks a_1 and a_2 and the 0.6 eV spin-orbit separation in the FY spectrum of ferrihydrite-modified diatomite are the same as those in the FY spectrum of pure SiO_2 (Figure 5.7a), suggesting that the bulk Si component of ferrihydrite-modified diatomite largely remains as SiO_2. A slight energy shift in the peak positions (particularly peak a_2) to the lower energy side in the spectra of 0.5 to 2.5-FHMD samples is noted when compared with those of FN6 and SiO_2 (Figure 5.7a), as the bridging oxygen in the Si-O-Si bond is replaced by the OH group on the surface. The absence of an oxygen atom in the Si-O-Si bond results in the decrease in the Si 2*p* binding energy (Xiong et al 2009).

In the TEY spectra of SiO_2 and FN6 (Figure 5.7b), peaks a_1, a_2, and b are located at 104.8, 105.4, and 107.3 eV, respectively. In combination with the Si $L_{3,2}$-edge FY spectra of SiO_2 and FN6, the TEY spectra of SiO_2 and FN6 indicates that raw diatomite primarily contains amorphous SiO_2. As indicated in the TEY spectra of 0.5- to 2.5-FHMD, the Si 2*p* spin-orbit splitting transitions could not be resolved in peak *a* located at 104.5 eV. Close-up regions (peaks *a* and *b*) of TEY spectra of ferrihydrite-modified diatomite are shown in Figure 5.7e. The decrease in the relative height of peak *a* with increasing $FeCl_2$ amount and decreasing Si/Fe molar ratios is evident in Figure 5.7d.

To demonstrate the formation of Si-containing ferrihydrite on the surface of diatomite and investigate the relationship between the crystallinity of Si-containing ferrihydrite and the amount of $FeCl_2$, synthetic Si-containing ferrihydrites (FHYD) in different Si/Fe ratios were measured by the TEY method. As shown in Figure 5.7e, no splitting can be resolved in peak *a* in the TEY spectra of synthetic Si-containing ferrihydrites in different Si/Fe molar ratios (0.2- to 0.5-FHYD). The spectrum of 0.1-FHYD is not shown in Figure 5.7e because the spectrum still contains too much noise although the repetitive scanning did increase the signal to noise ratio. The low Si content of 0.1-FHYD is probably below the detection limit of the XANES analysis method in this instance. The *a* peaks of ferrihydrite-modified diatomites and synthetic Si-containing ferrihydrites are at the same position and all spectra have a similar shape, which demonstrates that Si-containing ferrihydrite is formed on the surface of diatomite and dissolved Si provided by raw diatomite is incorporated into the ferrihydrite structure. The degree of crystallinity of Si-containing ferrihydrite increases as the ratio of Si/Fe decreases from 0.5 to 0.1 (Seehra et al. 2004). In Figure 5.7e, the height of the pre-edge *a* peak decreases with decreasing Si/Fe molar ratio, indicating that the degree of crystallinity of Si-containing ferrihydrite increases with the decreasing height of pre-edge peak *a*. The decreasing height of peak *a* with increasing $FeCl_2$ concentration (Figure 5.7d) confirms that the degree of crystallinity of Si-containing ferrihydrite of ferrihydrite-modified diatomite increases with increasing $FeCl_2$ concentration.

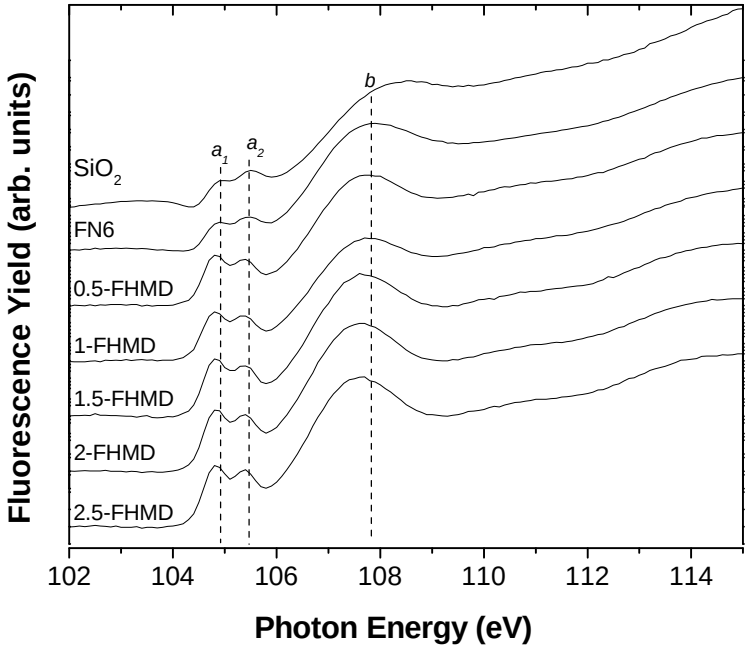
Fluorescence Yield (arb. units)
Photon Energy (eV)
102
104
106
108
110
112
114
a1
a2
b
SiO2
FN6
0.5-FHMD
1-FHMD
1.5-FHMD
2-FHMD
2.5-FHMD

(a)

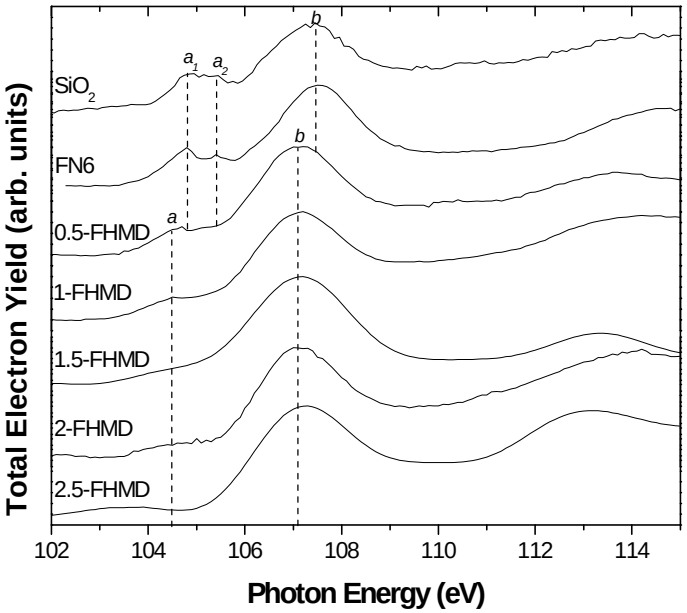
Total Electron Yield (arb. units)
Photon Energy (eV)
SiO2
FN6
0.5-FHMD
1-FHMD
1.5-FHMD
2-FHMD
2.5-FHMD
a1
a2
a
b
102
104
106
108
110
112
114

(b)

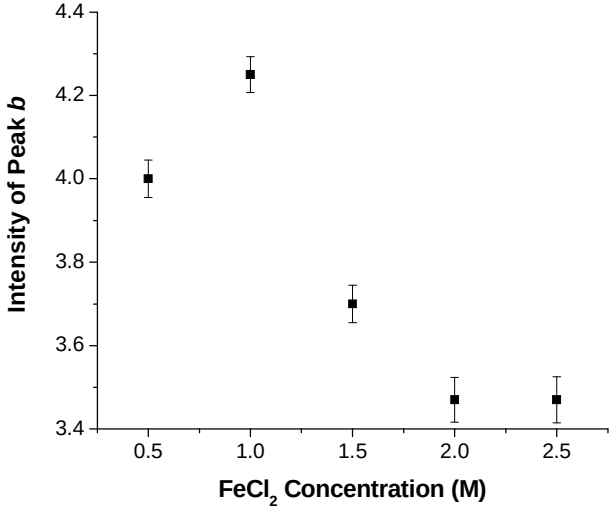
Intensity of Peak b
FeCl2 Concentration (M)
4.4
4.2
4.0
3.8
3.6
3.4
0.5
1.0
1.5
2.0
2.5

(c)

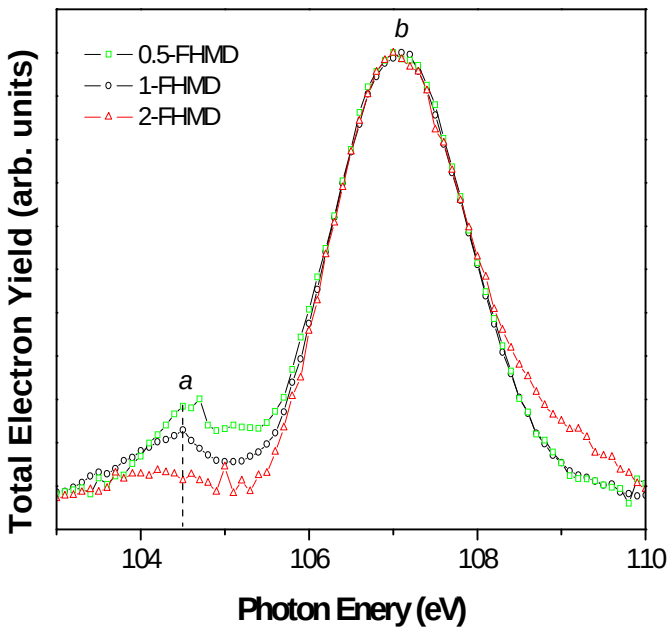

(d)

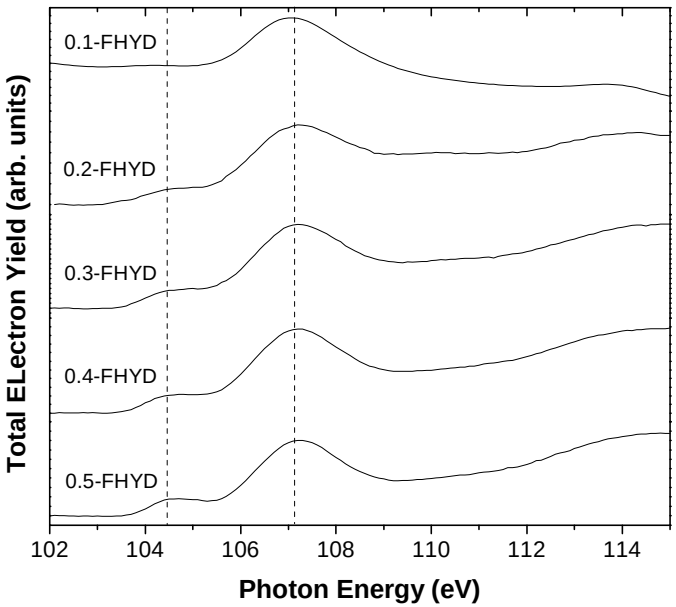

(e)

Figure 5.7 Si $L_{3,2}$-edge XANES spectra of raw diatomite and FHMDs: (a) FY mode; (b) TEY mode; (c) TEY spectra of synthetic Si containing ferrihydrite; (d) changes in peak *b* intensity with $FeCl_2$ concentration; and (e) close-up region of TEY spectra of ferrihydrite-modified diatomite

5.2.1.2 Fe $L_{3,2}$-edge XANES spectra

Fe $L_{3,2}$-edge TEY spectra of FHMD are shown in Figure 5.8a. Four peaks are observed in the spectra. The Fe 3*d* states couple mainly with the O 2*p* states. This bonding, taking place in a distorted cubic crystalline surrounded by oxygen atoms, causes the 3*d* states to split into the t_{2g} and e_g manifolds (Xiong et al 2009). Peaks *a* and *b* located at 708.5 and 710 eV, respectively, are produced by transitions from the Fe $2p_{3/2}$ levels into the e_g orbitals; the *c* and *d* peaks located at 722 and 723.4 eV, respectively, are associated with transitions from the Fe $2p_{1/2}$ levels into the t_{2g} orbitals (Wilks et al. 2006). The spectrum of reference compound Fe_2O_3 is shown in Figure 5.8a, and agrees well with previous reports (Kumar et al. 2007; Kuiper et al. 1993). Provided the oxygen is the nearest-neighbour anion, the Fe $L_{3,2}$-edges have spectral shapes that are sensitive to the oxidation state of iron (Garvie and Buseck 1998). Although the spectrum of FeO is not shown here, other research has demonstrated that the main difference between FeO and Fe_2O_3 is readily found at the L_3 features (Kumar et al. 2007). Kumar et al. (2007) reported that the first peak of the L_3 feature in the spectrum of FeO even became a shoulder of the second peak, while the L_3 feature of Fe_2O_3 is characterized by a well-resolved doublet, a weak peak marked as *a*, and a main peak marked as *b* (Figure 5.8a). The difference between Fe_2O_3 and Fe^{2+} compounds is attributed to the variation of 3*d* electron configuration of Fe ions and the indication of local symmetry (tetrahedral or octahedral) (Kumar et al. 2007). The spectra of 0.5- to 2.5-FHMD exhibit no energy shift compared with the Fe_2O_3 spectrum and a fairly developed first peak *a*, indicating that the complete oxidation of $FeCl_2$ occurs during the synthesis of ferrihydrite-modified diatomite and then a ferric ion-containing iron oxide (e.g. ferrihydrite, goethite, or hematite) is formed on the diatomite.

As per the discussion in the Si L-edge Section, not only Fe_2O_3 but also Si-containing ferrihydrite is produced. However, the crystallinity of ferrihydrite cannot be determined by the Fe $L_{3,2}$ shape because Fe^{3+} spectra are dominated by quasiatomic transition, with only minor modification from the solid state environment (Garvie and Buseck 1998). Besides that, Si-containing ferrihydrite is proved to be formed on the surface and be

deposited into pores of diatomite, the relationship between the amount of ferrihydrite and the concentration of $FeCl_2$ is illustrated in Figure 5.8b. It can be seen in Figure 5.8b that intensity of L_3 features (sum of intensities of peaks *a* and *b*) obtained through peak-fitting analysis increases with the $FeCl_2$ concentration, which suggests that more $FeCl_2$ produces more ferrihydrite and then more ferrihydrite are deposited into pores of diatomite. As shown in Figure 5.8c, the Fe L-edge spectrum of 1-FHMD is fitted with two arctangent step functions (centered at 709.6 eV and 723.5 eV, respectively), two Lorentzian functions (centered at 708.4 eV and 710 eV, respectively), and two Gaussian functions (centered at 721.9 eV and 723.6 eV).

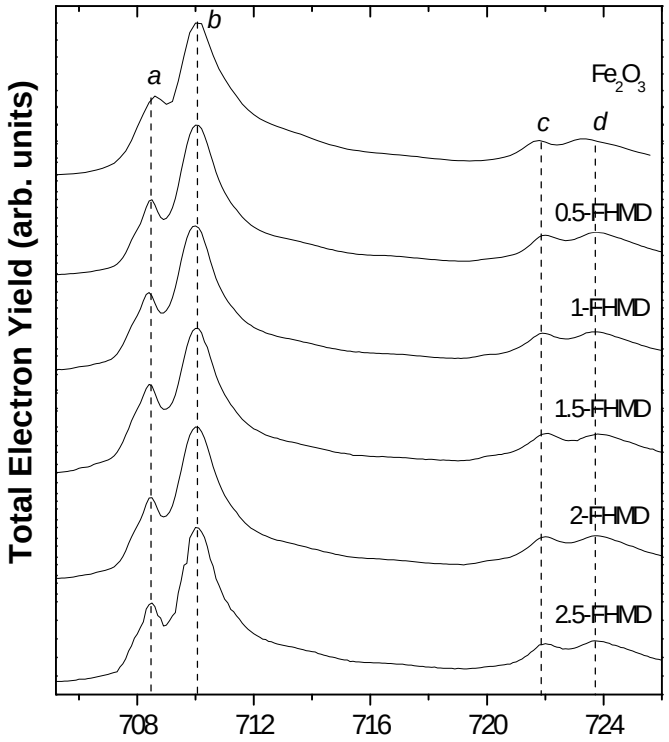
Total Electron Yield (arb. units)
a
b
c
d
Fe2O3
0.5-FHMD
1-FHMD
1.5-FHMD
2-FHMD
2.5-FHMD
708
712
716
720
724

(a)

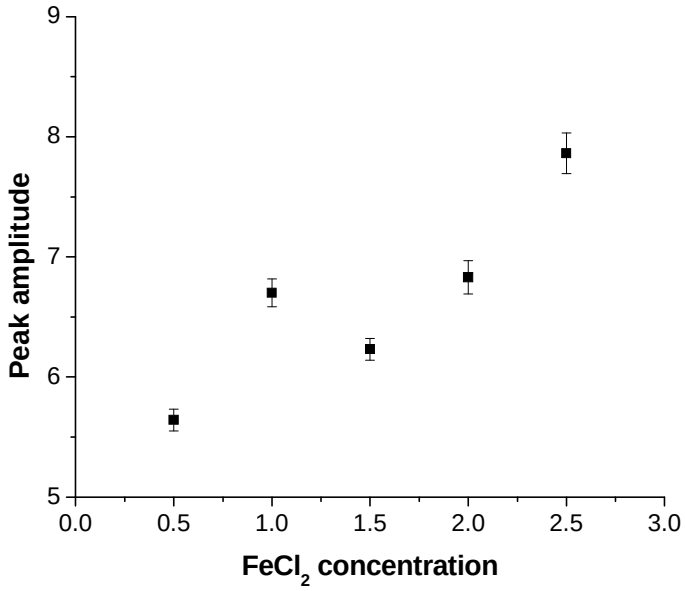
Peak amplitude
FeCl2 concentration
5
6
7
8
9
0.0
0.5
1.0
1.5
2.0
2.5
3.0

(b)

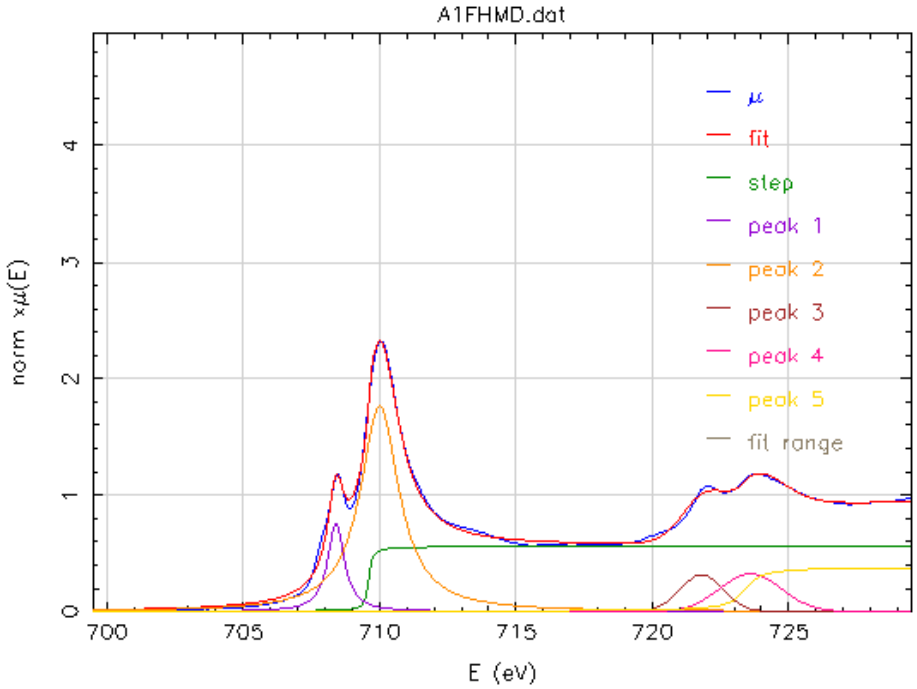

(c)

Figure 5.8 (a) Fe TEY $L_{3,2}$-edge XANES spectra of FHMDs, (b) changes in peak amplitude with $FeCl_2$ concentration, and (c) peak fitting of Fe TEY $L_{3,2}$-edge spectrum of 1-FHMD

5.2.1.3 Si K-edge XANES spectra

Si K-edge TEY spectra of FN6 and 0.5- to 2.5-FHMD are provided in Figure 5.9a, along with the spectrum of reference compound SiO_2. These spectra are recorded in the photon energy range 1842-1856 eV. A major peak *a* located at 1848 eV is assigned to a $1s \rightarrow 3p$ transition in tetrahedral SiO_4 molecules (Li et al. 1996). As described previously, the Si K-edge TEY method can be considered bulk sensitive. Si K-edge spectra of FN6 and 0.5- to 2.5-FHMD closely resemble the spectrum of SiO_2 and do not show any significant energy shift, which is consistent with the findings from Si L-edge spectra that the bulk of ferrihydrite-modified diatomite is present as SiO_2. Figure 5.9b shows changes in intensities of peak *a* with increasing $FeCl_2$ concentration. The peak intensity decreases with increasing $FeCl_2$ concentration. The decrease in peak intensity can be attributed to the formation of more ferric oxide as discussed in the previous Section. More ferric oxides are produced when $FeCl_2$ is present at higher concentrations, thereby decreasing the amount of SiO_2 in the sampling region of Si K-edge XANES. Changes in the intensity of peak *a* in Figure 5.9b are similar to changes in the intensity of peak *b* in Figure 5.7c, as the final state of both transitions ($1s \rightarrow 3p$ and $2p \rightarrow 3p$) is the Si 3*p* state (Xiong et al 2009). However, they cannot be exactly the same because of different mechanisms of electronic transition; one is allowed by the dipole selection rule while the other is forbidden (Xiong et al 2009). An example of peak fitting to determine the relative intensity (i.e., 1-FHMD) is shown in Figure 5.9c. The Si K-edge spectrum of 1-FHMD is fitted with three arctangent step functions (centered at 1840.6 eV, 1841.8 eV, and 1851.8 eV, respectively) and three Lorentzian functions (centered at 1842.2 eV, 1848 eV, and 1852.3 eV, respectively).

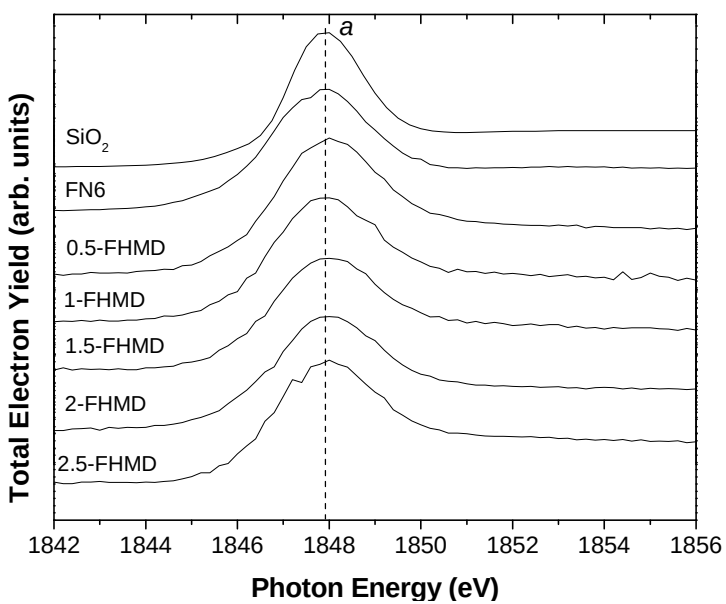
a
SiO2
FN6
0.5-FHMD
1-FHMD
1.5-FHMD
2-FHMD
2.5-FHMD
Total Electron Yield (arb. units)
1842
1844
1846
1848
1850
1852
1854
1856
Photon Energy (eV)

(a)

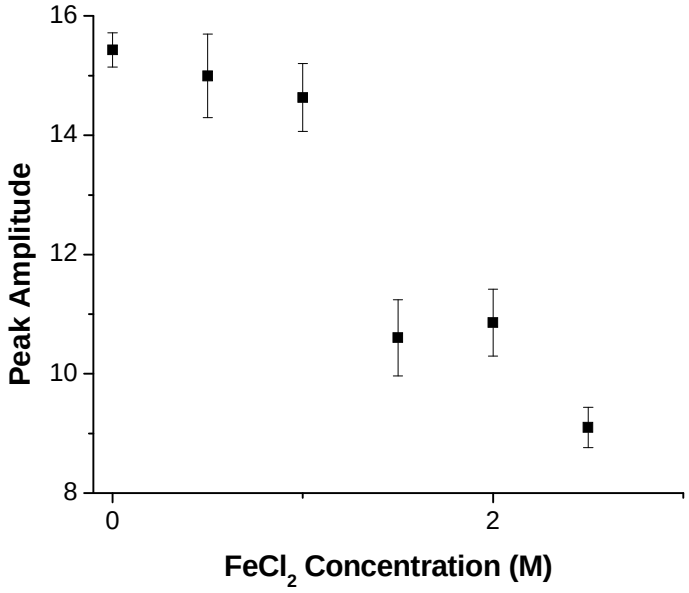
16
14
12
10
8
Peak Amplitude
0
2
FeCl2 Concentration (M)

(b)

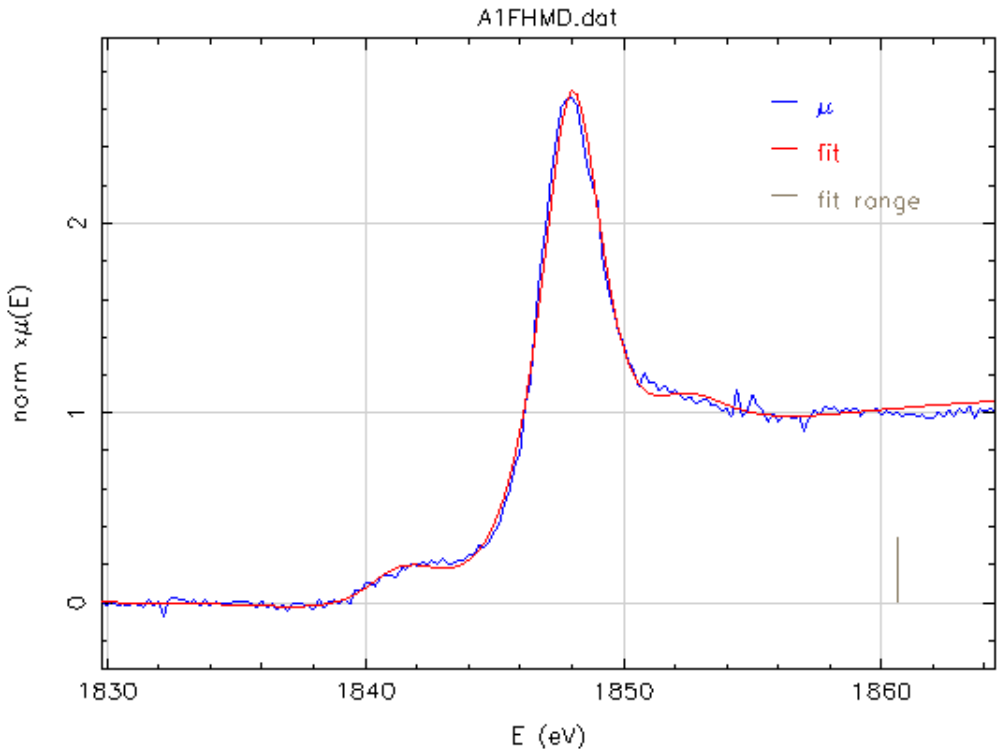

(c)

Figure 5.9 (a) Si K-edge XANES spectra of raw diatomite and FHMDs, (b) changes in peak amplitude with $FeCl_2$ concentration, and (c) peak fitting of Si K-edge XANES spectrum of 1-FHMD

5.2.1.4 BET analysis

The textural parameters of FHMDs (from 0.5-FHMD to 2.5-FHMD) such as BET specific surface area S_{BET}, total pore volume V_p, and average pore diameter D_P, are tabulated in Table 5.2. The BET specific surface area of FHMDs (from 0.5-FHMD to 2.5-FHMD) decreases with $FeCl_2$ amount from 221 to 163.6 m^2/g although the S_{BET} of 2.5-FHMD (169.6 m^2/g) is slightly higher than those of 1.5-FHMD (163.9 m^2/g) and 2-FHMD (163.6 m^2/g). The decrease of surface area of FHMDs can be explained by observations from the XANES study described previously, which indicate the degree of crystallinity of ferrihydrite increases with $FeCl_2$ concentration. This result is also in agreement with the findings of Vempati and Loeppert (1989), where the degree of crystallinity of Si-containing ferrihydrite is inversely related to the Si/Fe molar ratio; the specific surface area also decreases with an increasing degree of crystallinity. The average pore diameter increases with the $FeCl_2$ amount from 3.6 nm (0.5-FHMD) to 5.3 nm (2.5-FHMD). Similarly, the increase in average pore diameter is attributed to the increasing degree of crystallinity.

Table 5.2 Specific surface area S_{BET}, total pore volume V_P, and average pore diameter D_P of FHMD

Sample	S_{BET} (m^2 g^{-1})	V_P (cc g^{-1})	D_P (nm)
0.5-FHMD	221.0	0.198	3.60
1-FHMD	211.1	0.200	3.79
1.5-FHMD	163.9	0.163	4.00
2-FHMD	163.6	0.200	4.90
2.5-FHMD	169.6	0.220	5.30

The differential pore size distribution of diatomite treated with different $FeCl_2$ concentrations (0.5- to 2.5-FHMD) is shown in Figure 5.10. As discussed before, although ferrihydrite of 0.5-FHMD exhibits the least crystalline degree, the ferrihydrite

of 1-FHMD also exhibits a low crystalline degree. An insignificant shift in peak maxima to lower pore sizes in the differential pore size distribution of 0.5-FHMD vs. 1-FHMD (Figure 5.10) indicates that the low crystalline ferrihydrite of 1-FHMD still can cause a high percent of macropores and larger mesopores to be blocked. The pore size distributions of 0.5-FHMD and 1-FHMD show a sharp shift from the large pore size to a lower pore size.

A very similar shift to those of 0.5- and 1-FHMD was observed in the pore size distribution of 1.5-FHMD; however, the volume of small pores of 1.5-FHMD is much lower than in 0.5- and 1-FHMD (Figure 5.10). The lower volume of small pores is attributed to the deposition of lepidocrocite, which has a larger average pore diameter and particle size. A weak pre-edge peak *a* is observed in the Si L-edge TEY spectrum of 1.5-FHMD (Figure 5.7b), which implies a small amount of Si is incorporated into the ferrihydrite structure of 1.5-FHMD. Compared with the relative height of peak *a* in the spectrum of 0.1-FHYD, the *Si*/*Fe* molar ratio of ferrihydrite in 1.5-FHMD can be estimated at 0.1. At an Si/Fe molar ratio of 0-0.1, the oxidation of Fe(II) results in the formation of lepidocrocite, a moderately crystalline ferric oxide (Mayer and Jarrell 1996). The average pore diameter and particle size increase during the transformation of ferrihydrite to lepidocrocite.

Figure 5.10 illustrates the gradual shift towards the lower pore diameter in the pore size distribution of 2- and 2.5-FHMD. The gradual shift can be assigned to the formation of hematite on 2- and 2.5-FHMD. Notably, peak *a* in the TEY spectra of 2-FHMD and 2.5-FHMD is not readily observed, which implies the Si content of 2-FHMD and 2.5-FHMD is almost zero. Without Si inhibiting the ripening and agglomeration of ferrihydrite, ferrihydrite is transformed to hematite (α-Fe_2O_3) during the synthesis of 2-FHMD and 2.5-FHMD. Schwertmann et al. (1999) report that 2-line ferrihydrite without Si is transformed to hematite at temperatures of 15-30°C and at pH values of 2-12. The temperature and pH required for the synthesis of FHMD favour the transformation of ferrihydrite to hematite in the absence of Si. The average pore

diameter of hematite particles is 10.4 nm (Herrera et al. 2001) and particle size of hematite nanoparticles ranges from 30 to 50 nm (Schwertmann and Cornell 2000). 30-50 nm hematite particles are not able to be deposited into mesopores. An increase in micropore volume and micropore surface area through the partial blockage of mesopores is unlikely to occur. However, 30-50 nm hematite particles can be deposited into macropores, thereby increasing mesopore volume. An additional increase in the volume of larger mesopores can be obtained through the introduction of mesoporous hematite (average pore diameter 10.4 nm).

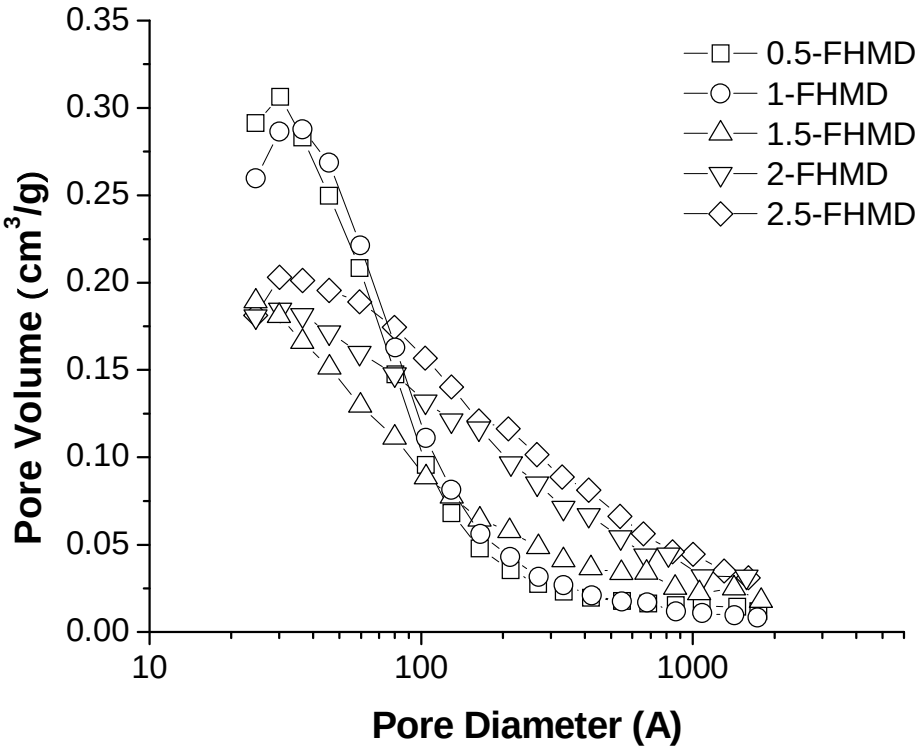

Figure 5.10 Pore size distribution of FHMDs with different $FeCl_2$ concentrations (0.5-2.5 M)

Figure 5.11 shows nitrogen adsorption-desorption isotherm plots recorded for 0.5- to 2.5-FHMD. All nitrogen adsorption-desorption isotherms are classified as type IV,

which indicates that 0.5- to 2.5-FHMD are mesoporous materials. The nitrogen adsorption and desorption isotherms of 0.5- to 1.5-FHMD show a H2-type hysteresis loop (IUPAC classification); the nitrogen adsorption and desorption isotherms of 2- and 2.5-FHMD show a H3-type hysteresis loop (Figure 5.11). The H2-type hysteresis loop demonstrates that the pore size distribution is not uniform and that pore blockage plays an important role in the synthesis of FHMD. The H3-type hysteresis loop was observed with aggregates of plate-like particles, and was consistent with the fact that hematite can form platelets (Matijevic and Borkovec 2004). The more crystalline hematite of 2-FHMD and 2.5-FHMD aggregates to form the hematite platelets (Matijevic and Borkovec 2004).

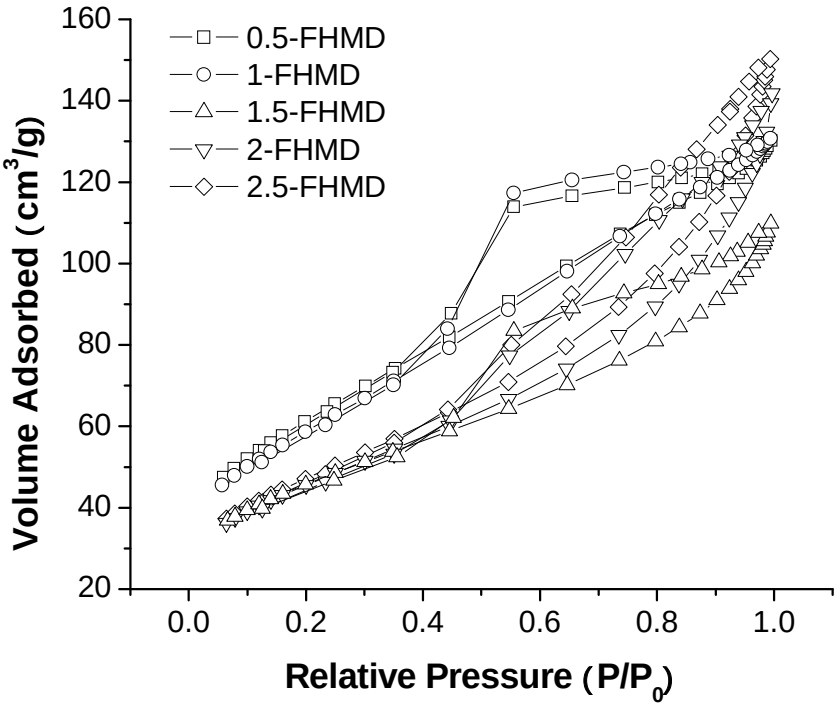

Figure 5.11 BET isotherm plots of FHMDs with different $FeCl_2$ concentrations (0.5-2.5 M)

5.2.2 Effects of NaOH Concentrations

Diatomite is slightly unstable in higher pH conditions, and the SiO_2 of raw diatomite is partially dissolved in the NaOH solution with stirring and heating (Khraisheh et al. 2004). The amount of dissolved Si is a function of the NaOH concentration (Xiong et al 2009). In the research conducted for this thesis, NaOH in concentrations of 3, 4, 5 and 6 M was used to treat raw diatomite, with other synthesis conditions of 100 mL of 1 M $FeCl_2$ solution and a drying temperature of 50°C held constant. The FHMDs produced through NaOH treatment were named as 3NaOH-FHMD, 4NaOH-FHMD, 5NaOH-FHMD and 6NaOH-FHMD.

5.2.2.1 Si $L_{3,2}$-edge XANES spectra

Si $L_{3,2}$-edge FY spectra and TEY spectra of NaOH-FHMDs are shown in Figures 5.12a and 5.12b, respectively. Similar to Figure 5.7d, close-ups of peaks *a* and *b* in the TEY spectra of NaOH-FHMDs are shown in Figure 5.12c. In the FY spectra of NaOH-FHMDs (Figure 5.12a), the line shapes, the spin-orbit splittings, and their distances have a strong resemblance to those of the FN6 FY spectrum. The exceptions are the positions of pre-edge peaks that indicate the bulk SiO_2 of diatomite is preserved relative to the partial dissolution of the surface SiO_2; NaOH concentration does not appear to have a remarkable effect on the chemical characteristics of the bulk diatomite. Furthermore, the NaOH-FHMD peaks shift to lower energy, as did the $FeCl_2$-FHMD peaks (Figure 5.7a); the reasoning for this energy shift was described above in Section 5.2.1.1.

In the TEY spectra of the NaOH-FHMDs (Figure 5.12b), the spin-orbit doublets have completely disappeared and only peak *a* exists in the pre-edge region, indicating that the surface SiO_2 of diatomite is partially dissolved in the NaOH solution and then dissolved Si is incorporated into the structure of ferrihydrite. Figure 5.12c shows the height of peak *a* in the NaOH-FHMD spectra increases as NaOH concentrations rise from 3 to 6 M. As observed in the synthetic ferrihydrites (0.1- to 0.5-FHYD) (Figure 5.7e), the height of peak *a* increases with increasing Si content of Si-containing ferrihydrite. This indicates the Si content of the Si-containing ferrihydrite on the surface of the NaOH-

FHMDs increases with NaOH concentration. Furthermore, the degree of crystallinity of Si-containing ferrihydrite in ferrihydrite-modified diatomite decreases with increasing NaOH concentration.

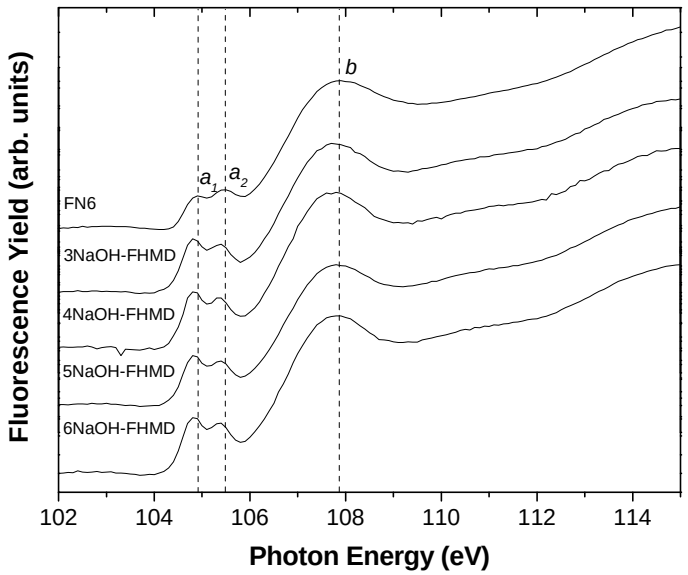
Fluorescence Yield (arb. units)
Photon Energy (eV)
102
104
106
108
110
112
114
a1
a2
b
FN6
3NaOH-FHMD
4NaOH-FHMD
5NaOH-FHMD
6NaOH-FHMD

(a)

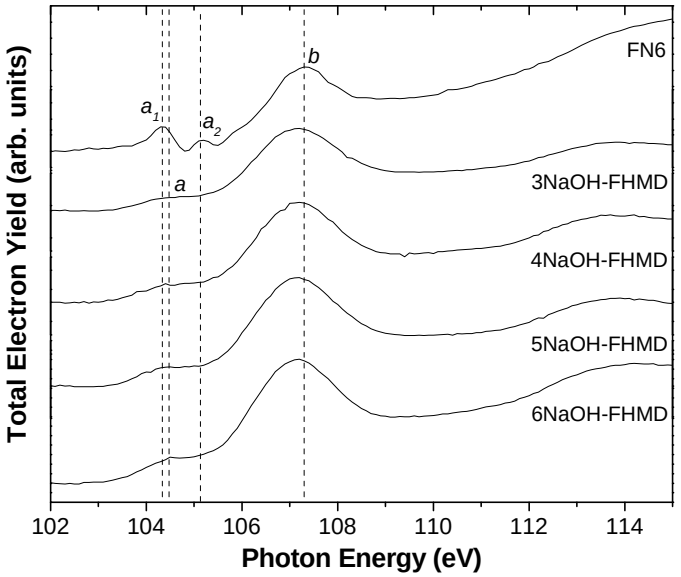
Total Electron Yield (arb. units)
Photon Energy (eV)
102
104
106
108
110
112
114
a1
a2
a
b
FN6
3NaOH-FHMD
4NaOH-FHMD
5NaOH-FHMD
6NaOH-FHMD

(b)

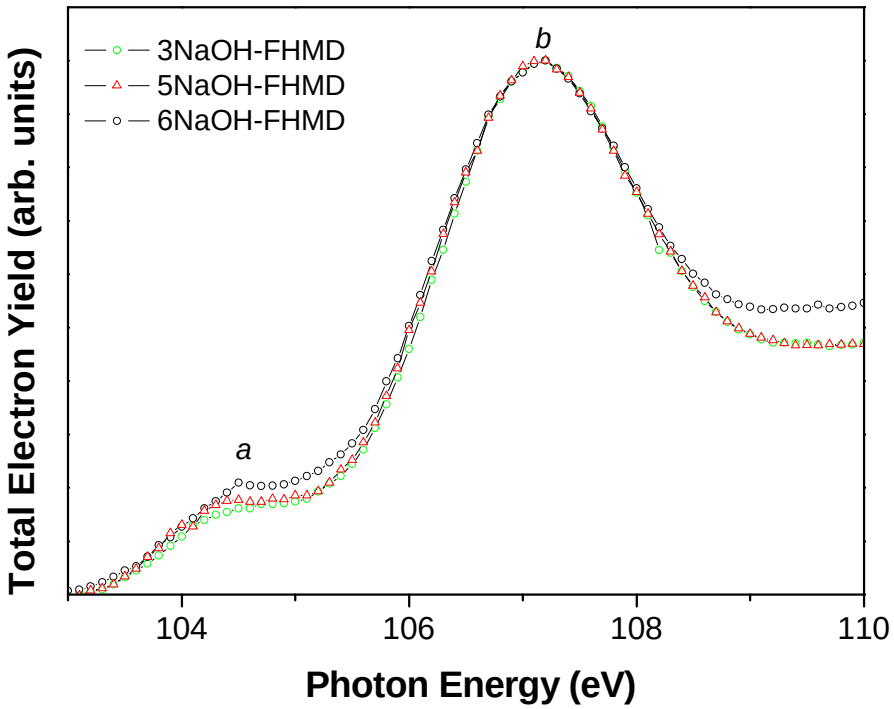

(c)

Figure 5.12 Si $L_{3,2}$-edge XANES spectra of FHMDs treated with different NaOH concentrations: (a) FY mode; (b) TEY mode; and (c) close-up region of TEY spectra of NaOH-FHMDs

5.2.2.2 Fe L3,2-edge XANES spectra

Fe TEY $L_{3,2}$-edge spectra of FN6 and NaOH-FHMDs are shown in Figure 5.13a. Resemblance between the Fe_2O_3 $L_{3,2}$ shape and NaOH-FN6s $L_{3,2}$ shapes suggests that ferric oxide is formed on the ferrihydrite-modified diatomite. In combination with Figure 5.12b, Figure 5.13a futher indicates that Si-containing ferrihydrite is formed on the surface of ferrihydrite-modified diatomite. As shown in Figure 5.13b, the sum of the amplitudes of the L_3 features, including peaks a and b in the NaOH-FHMD spectra, increases with NaOH concentration, indicating more ferrihydrite is formed as NaOH concentration increases. As shown in Figure 5.13c, the Fe L-edge spectrum of 6NaOH-FHMD is fitted with two arctangent step functions (centered at 709.6 eV and 723.5 eV, respectively), two Lorentzian functions (centered at 708.4 eV and 710 eV, respectively), and two Gaussian functions (centered at 721.9 eV and 723.6 eV).

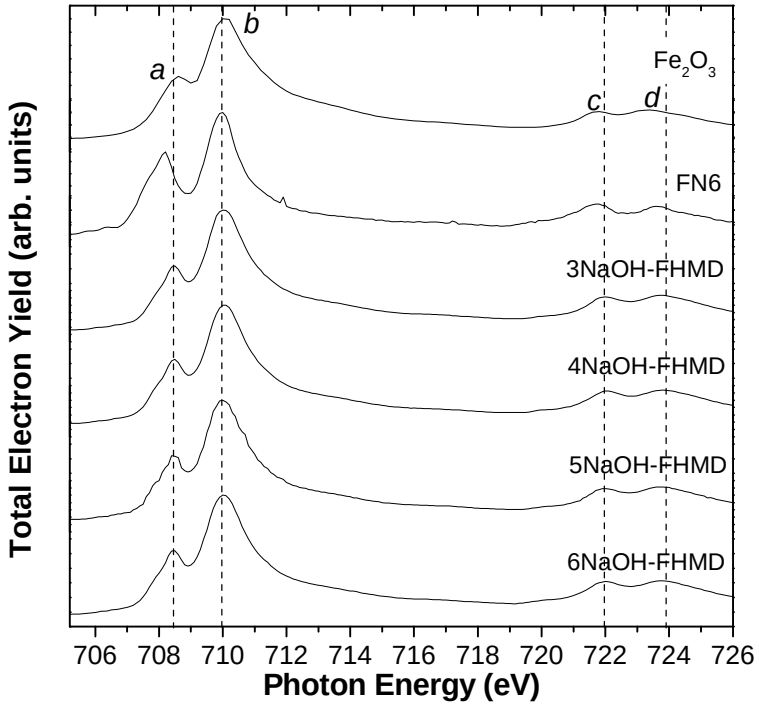
a
b
c
d
Fe2O3
FN6
3NaOH-FHMD
4NaOH-FHMD
5NaOH-FHMD
6NaOH-FHMD
Total Electron Yield (arb. units)
706 708 710 712 714 716 718 720 722 724 726
Photon Energy (eV)

(a)

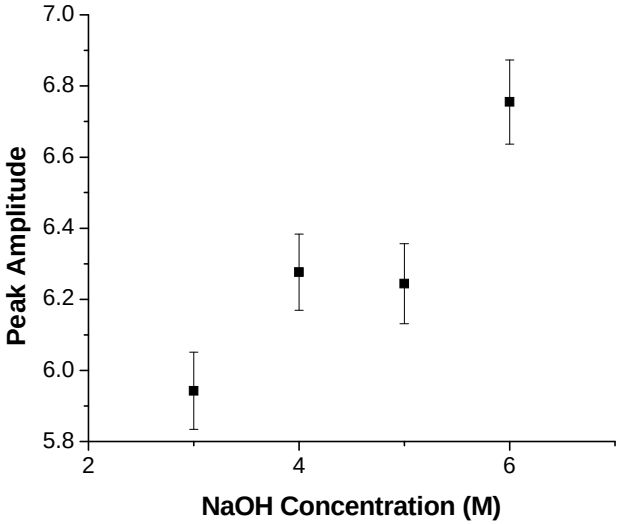
7.0
6.8
6.6
6.4
6.2
6.0
5.8
Peak Amplitude
2
4
6
NaOH Concentration (M)

(b)

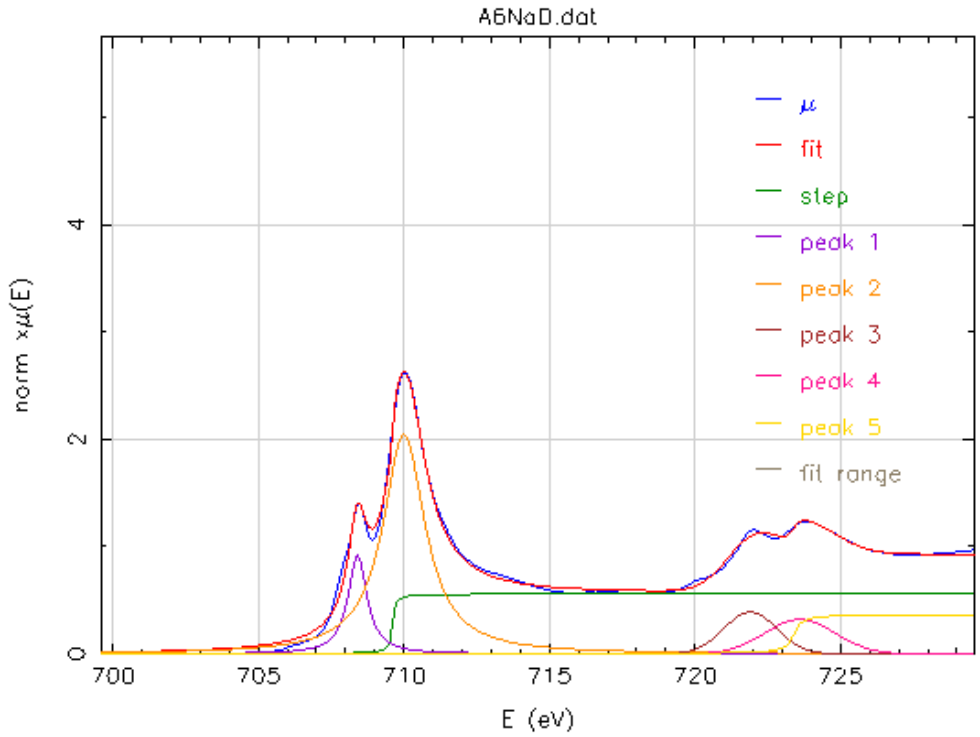

(c)

Figure 5.13 Fe TEY $L_{3,2}$-edge spectra of FHMDs with different NaOH concentrations (a), changes in peak amplitude with NaOH concentration (b) and peak fitting of 6NaOH-FHMD (c)

5.2.3 Effects of Temperature

To evaluate the effect of temperature on the chemical nature and the degree of crystallinity, 1-FHMD was calcined at temperatures of 50, 300, 500, and 900 °C. These FHMDs were named 1-FHMD, 1FHMD-300, 1FHMD-500, and 1FHMD-900, respectively.

Si $L_{3,2}$-edge TEY spectra of the above-mentioned ferrihydrite-modified diatomites are shown in Figure 5.14. In Figure 5.14, an energy shift of 0.8 eV in the peak positions (particularly peak *a*) in the spectra of 1FHMD-300, 500, and 900 to the high energy side compared with 1-FHMD is observed; however, 1FHMD-300, 500, and 900 peak positions are comparable. Glasauer et al. (2000) observed dehydroxylation when Si-containing ferrihydrite was calcined at high temperature. During the dehydroxylation, Si-OH groups of Si-containing ferrihydrite were replaced with Si-O bonds. The dehydroxylation results in a decrease of electron density on Si due to the high electronegativity of oxygen atom and thus results in the higher binding electron energy. The lack of identifiable shift among 1FHMD-300, -500, and -900 suggests that no further dehydroxylation reaction occurs when the calcination temperature is greater than 300 °C.

Glasauer et al. (2000) also reported that Si-containing ferrihydrite is stable even when heated to 600 °C. Thus, amorphous Si-containing ferrihydrite still exists on the surface of 1FHMD-300 and -500. The same relative height of peak *a* of 0.2 to the main peak *b* is observed in the TEY spectra of 1FHMD, 1FHMD-300, and 1FHMD-500 (Figure 5.14), due to similar Si contents of Si-containing ferrihydrite. However, height of peak *a* in 1FHMD-900 relative to the maximum peak *b* is 0.32. Glasauer et al. (2000) reported that a transformation of Si-containing ferrihydrite to a well-crystallized hematite occurred after heating at 850 °C. Campbell et al. (2002) found that the temperature of transformation for Si-containing ferrihydrite to hematite was 780 °C. Campbell et al. (2002) also reported that Si entered the structure of crystalline hematite formed by heating Si-containing ferrihydrite. This suggests that Si-containing

crystallized hematite is formed on the surface of 1FHMD-900. The crystallized phase has an intense XANES pre-edge peak relative to the amorphous phase (Politi et al. 2008), which explains why the relative pre-edge peak height in 1FHMD-900 TEY spectrum is higher than in the 1FHMD-300 and -500 spectra. Glasauer et al. (2000) demonstrated that thermal treatment of Si-containing ferrihydrite caused a substantial decrease in the specific surface area and an increase in average pore diameter.

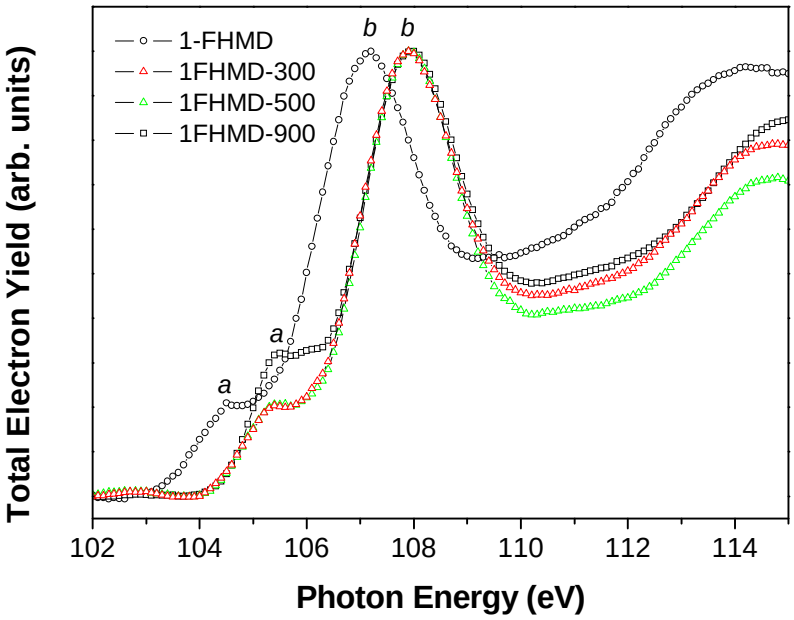

Figure 5.14 Si $L_{3,2}$-edge TEY spectra of FHMDs calcined at different temperatures

5.3 Phosphorus Adsorption onto Ferrihydrite-Modified Diatomite

5.3.1 Adsorption Isotherm

P adsorption isotherm can be described by the Langmuir, Freundlich, and Temkin equations. The isotherms of P adsorption onto raw diatomite and FHMD at both pH 4 and 8.5 are shown in Figure 5.15. Table 5.3 shows the maximum adsorption capacity (Q_0), the values of Langmuir constants, and the correlation coefficient (r_L^2) for the Langmuir equation. Correlation coefficients (r_F^2 and r_T^2) for the Freundlich and Temkin equations are provided in Table 5.3 for comparison. The Langmuir model best describes the P adsorption data for both raw diatomite and FHMD compared to Freundlich and Temkin models. The Langmuir isotherm is more applicable for chemisorption (Lowell et al. 2004). Chemisorption is an adsorption that results from chemical bonding formation (strong interaction) between the adsorbent and the adsorbate in a monolayer on the surface, in an often irreversible process. The Langmuir equation is expressed as:

$$q_e = \frac{K_L C_e}{1 + a_L C_e} \qquad [5.2]$$

where q_e is the amount of P adsorbed per gram of adsorbent at equilibrium (mg P/g), and K_L and a_L are the Langmuir adsorption equilibrium constants. The constant K_L is related to the adsorption free energy (Bayrak 2006); K_L / a_L gives the maximum adsorption capacity (theoretical monolayer saturation capacity), Q_0. The Langmuir constants can be used to determine the suitability of the adsorbent for the adsorbate, which is expressed in term of a dimensionless equilibrium parameter R_L as:

$$R_L = \frac{1}{1 + K_L C_0} \qquad [5.3]$$

The R_L value interprets the nature of the interaction between adsorbent and adsorbate and the adsorption type; the adsorption is considered not suitable when $R_L > 1$, linear

when $R_L = 1$, suitable when $0 < R_L < 1$, and irreversible when $R_L = 0$ (Al-Degs et al. 2001).

As seen in Figure 5.15, P adsorption by raw diatomite and FHMD increases with increasing P concentration until a maximum adsorption (Q_0) is established. The maximum adsorption capacities for FHMD at pH 4 and 8.5 are 37.3 and 13.6 mg P/g, respectively; those for raw diatomite are 10.2 and 1.7 mg P/g, respectively. The low P adsorption capacity of raw diatomite at pH 8.5 makes it a less suitable adsorbent for the Jackfish lake water sample (pH 8.48) than FHMD. The Q_0 values for FHMD are higher than for raw diatomite, and are consistent with the results from the BET and surface charge tests. The BET surface area of an adsorbent is an important factor determining the adsorption capacity (Hsieh and Teng 2000). The Q_0 value for FHMD at pH 8.5 is lower than at pH 4 due to a lower positive surface charge density (Section 5.1.6). The decrease in K_L from 12.89 to 1.16 L/g with increasing pH, as shown in Table 5.3, indicates that the adsorption free energy increases and adsorption is more difficult at higher pH values. The higher K_L values of FHMD as compared to raw diatomite may be attributed to the development of mesopores, micropores, and supermicropores that facilitate P adsorption onto some interior sites of FHMD having stronger binding energies. The much lower value of R_L (0.0019) for FHMD at pH 4 than for raw diatomite (0.0035) indicates FHMD is a more favorable adsorbent for the P in solution than raw diatomite.

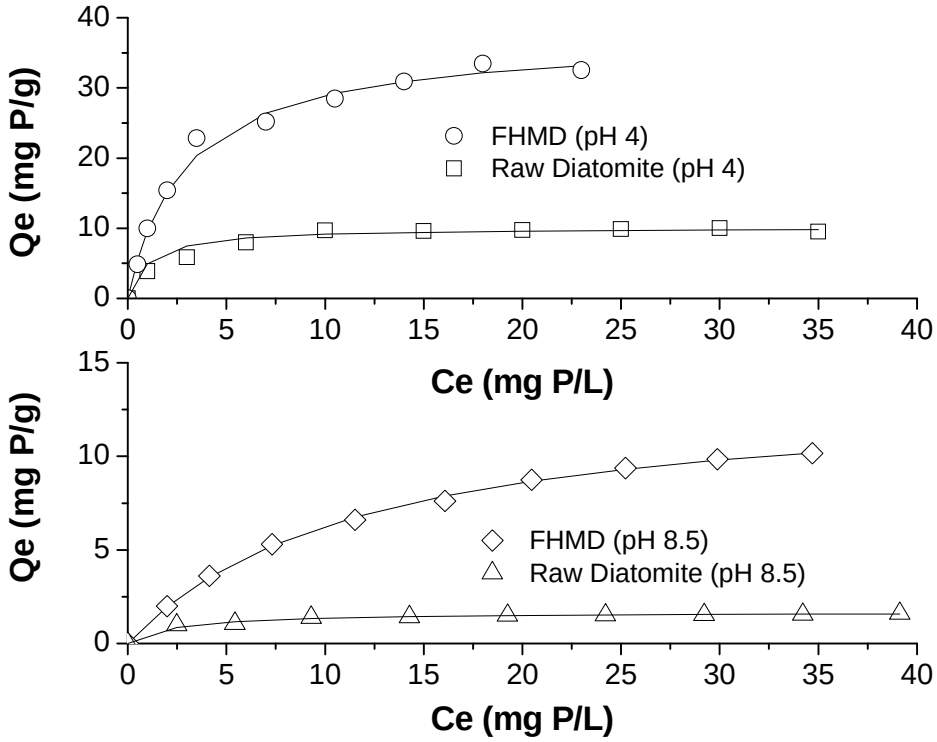

Figure 5.15 Phosphorus adsorption isotherms of raw diatomite and FHMD at pH 4 and pH 8.5

Table 5.3 Langmuir constants for phosphorus adsorption isotherms of raw diatomite and FHMD

	Q_0 (mg P/g)	a_L (L/mg)	K_L (L/g)	R_L ($C_0 = 40 mg/L$)	$r_L^{2\,a}$	$r_F^{2\,a}$	$r_T^{2\,a}$
Diatomite (pH 4)	10.2	0.7	7.19	0.0035	0.9964	0.8788	0.8979
FHMD (pH 4)	37.3	0.35	12.89	0.0019	0.9963	0.9127	0.9851
Diatomite (pH 8.5)	1.7	0.43	0.71	0.0338	0.9985	0.9194	0.9332
FHMD (pH 8.5)	13.6	0.085	1.16	0.0211	0.9986	0.976	0.9938

[a] r_L^2, r_F^2 and r_T^2: correlation coefficients for Langmuir, Freundlich, and Temkin isotherms, respectively.

5.3.2 Comparison of Phosphorus Adsorption Capacity with Common Low-Cost Adsorbents and Potential Application of Ferrihydrite-Modified Diatomite

Numerous adsorbents have been tested for their capacity to adsorb P. To illustrate the potential of FHMD in actual applications as a potential low-cost P adsorbent, a comparative evaluation of the adsorption capacities of various types of low-cost P adsorbents is provided in Table 5.4. This comparison clearly indicates that FHMD is an effective P adsorbent.

As an effective and environmentally safe P adsorbent, FHMD can be used for wastewater treatment and eutrophication control. FHMD, in fine powder form, can be applied to the effluent from biological treatment process, directly to the various biological treatment processes, and in physical-chemical treatment flow processes. If a granulated FHMD is produced, it could be applied to fixed-bed systems in the future. However, the adsorption behavior and the abrasion resistance of granular FHMD must be considered.

Direct addition of FHMD to a eutrophic lake would not only remove P from the water column but also improves the P binding capacity of the sediments.

Large-scale pilot tests using phosphate contaminated wastewater and/or large-scale enclosure experiments in eutrophic lakes should be conducted to optimize the adsorption process and estimate cost benefits of FHMD.

Table 5.4 Phosphorus adsorption capacity of different low-cost adsorbents

Adsorbent	Phosphorus Adsorption Capacity Q_0 (mgP/g)	Data Source
Sand	0.129	Arias et al. 2001
Synthesized iron oxide coated sand	1.5	Mezenner et al. 2008
Steel slag	5.3	Xiong et al. 2008
Activated alumina	17.5	Shin et al. 2004
Al_{10}SBA-15	26.7	Shin et al. 2004
Synthesized aluminum oxide	3.03	Wu et al. 2006
Zeolite	2.15	Sakadevan and Bavor 1998
Goethite	16.4	Oh et al. 1999
Hematite	2.2	Oh et al. 1999
Limestone	0.86	Drizo et al. 1999
Fly ash	0.86	Drizo et al. 1999
Red mud	0.23	Huang et al. 2008
Red mud with HCl treatment	0.58	Huang et al. 2008
FHMD	37.3	This research

5.3.3 Selective Phosphorus Adsorption onto Ferrihydrite-Modified Diatomite

Common anion species in lake water are HCO_3, CO_3, SO_4, and Cl, each typically present in concentrations greater than 1 mg/L (Kalff 2002). Remaining major anions such as phosphate and nitrate are utilized by biota as macronutrients. Anions compete for surface adsorption sites on adsorbents in lake water. The selective P adsorption onto FHMD among principal anions is shown in Figure 5.16. PO_{4s} and PO_{4c} in Figure 5.16 represent phosphate ion in a simple solution (containing only phosphate ions), and in a complex solution containing various anions at the same concentration respectively. As shown in Figure 5.16, the affinity of anion adsorption onto FHMD in the complex solution is in the order PO_4>SO_4>NO_3>CO_3>Cl. The amount of PO_{4c} adsorbed onto FHMD is more than four times that of SO_4. It is postulated that the strong affinity of P toward FHMD makes the amount of P adsorbed onto FHMD in the complex solution only slightly less than in the simple solution (Figure 5.16). These results indicate that FHMD preferentially adsorbs P and is a suitable adsorbent for P removal from lake water.

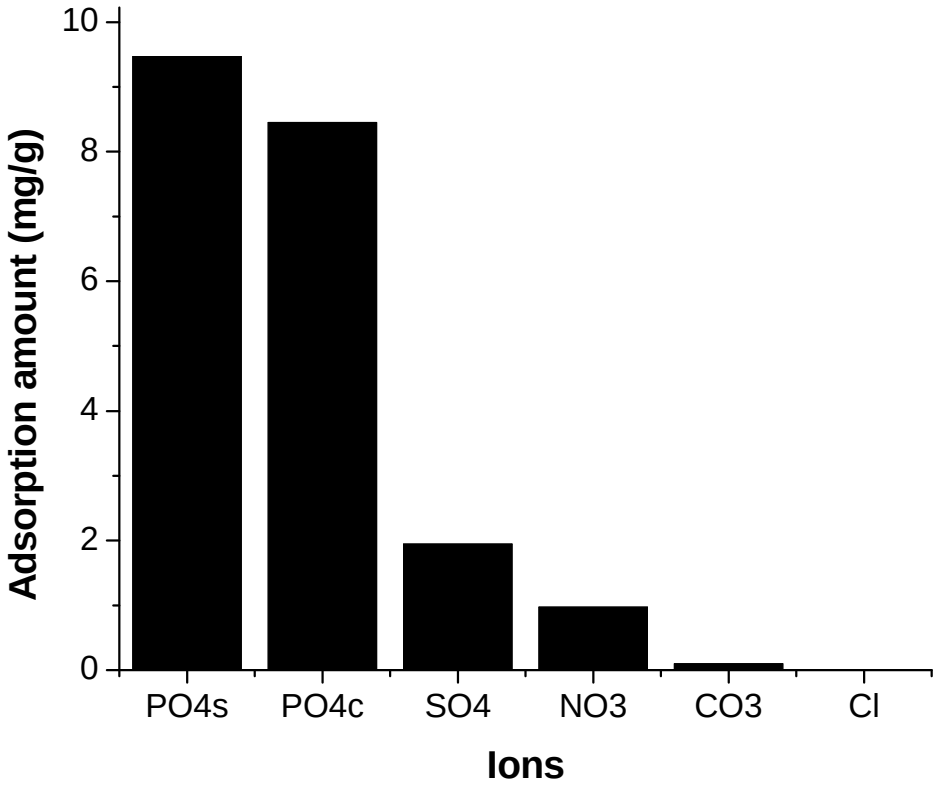

Figure 5.16 Selective phosphorus adsorption onto FHMD

5.3.4 XANES P L-Edge and K-Edge Spectra

Understanding how FHMD binds P during the process of P adsorption onto FHMD requires a molecular-scale spectroscopic technique. In contrast to the molecular-scale spectroscopic technique, the macroscopic adsorption kinetic studies cannot conclusively determine reaction mechanisms and resolve molecular and atomic information (Sparks 2003; O'Reilly et al. 2001). Among a number of molecular-scale spectroscopic techniques such as Fourier transform infrared (FTIR) and X-ray diffraction (XRD), XANES has some unique advantages. The main advantages of XANES are that it is element specific and nondestructure (no sample pretreatment required). Thus, *in situ* qualitative structural information about the average local chemical environment can be

elucidated by a fingerprinting technique of XANES spectroscopy. The fingerprinting technique means that unknown samples are compared with a library of reference compounds to find similarities.

In this research, XANES P analyses reveal that the resolution of the FY mode appears higher than TEY, and the reproducibility of FY mode is always better than TEY. Thus, all XANES P L-edge and K-edge spectra are recorded in the FY modes which are shown in Figure 5.17a and 5.17b, respectively. The first peak *a* in P L-edge spectra (Figure 5.17a) is due to the transition of P 2*p* electron to the 3*s*-like a_1^* molecular orbital; peak *b* is assigned to the transition of P 2*p* electrons to the 3*p*-like t_2^* orbital; and peak *c* is assigned to the transition of P 2*p* electrons to 3*d*-like e states (Li et al. 1995). Chemical bonding between atoms can be explained by the hybridization process in which a number of atomic orbitals are mixed to form the same number of hybrid orbitals. The hybridization of Fe-3*d*, O-2*p*, and P-3*p* valence orbitals of $FePO_4$ causes the first peak *a* to be split into peaks a_1 and a_2 in the P L-edge spectrum of $FePO_4$. As seen in Figure 5.17a, P L-edge spectra of FHMD-Ps (0.5FHMD-P to 2.5FHMD-P) resemble that of K_2HPO_4, which is the adsorbate to form FHMD-Ps. The spin-orbit coupling resulting from the hybridization of valence orbitals is not observed in the pre-edge region of the spectra of K_2HPO_4 or FHMD-Ps. The maximum analysis depth is about 50 nm for P L-edge FY spectra (Varlot et al. 2001). Thus, the P is not precipitated with Si-containing ferrihydrite of FHMD, but adsorbed onto the shallow surface layer of FHMD.

All P K-edge spectra consist of one sharp peak *a* (Figure 5.17b) arising from an electron transition from the 1*s* core level to the t_2^* (*p*-like) antibonding orbital, and one relatively weaker peak *b* that most likely corresponds to shape resonance or multiple scattering (Yin et al. 1995). A pre-edge peak *a* is observed in the P K-edge spectrum of $FePO_4$ in Figure 5.17b. This pre-edge peak is due to electron configurations and electron transitions at the X-ray absorption edge. This feature is one distinguishable characteristic of $FePO_4$ because the pre-edge peak is absent in the spectra of Al, K, Na,

and Ca phosphates (Hesterberg et al. 1999). The lack of a pre-edge peak in Al, K and Na phosphates is primarily due to the absence of *d* orbitals in Al, K, and Na (Khare et al. 2004). The P K-edge spectra of Ca phosphates exhibit a unique post-edge shoulder at the higher energy side of the white line peak (Hesterberg et al. 1999). In contrast to $FePO_4$, the pre-edge peak is very weak in the K-edge spectra of the FHMD-P (Figure 5.17b). The weak pre-edge feature indicates that P is adsorbed on FHMD, not precipitated with Fe (III), which is consistent with the results of phosphate adsorbed onto goethite reported by Hesterberg et al. (1999). The maximum analysis depth for P K-edge FY spectra is larger than 50 nm and calculated to reach 10 μm (Varlot et al. 2001). Thus, P is adsorbed onto the deeper surface layers of FHMD.

Therefore, Figure 5.17a and 5.17b demonstrate that P is adsorbed onto the surface of FHMD regardless of either shallow surface layer or deeper surface layer. P adsorption onto FHMD is expected not to reduce pH and buffering capacity of lake water.

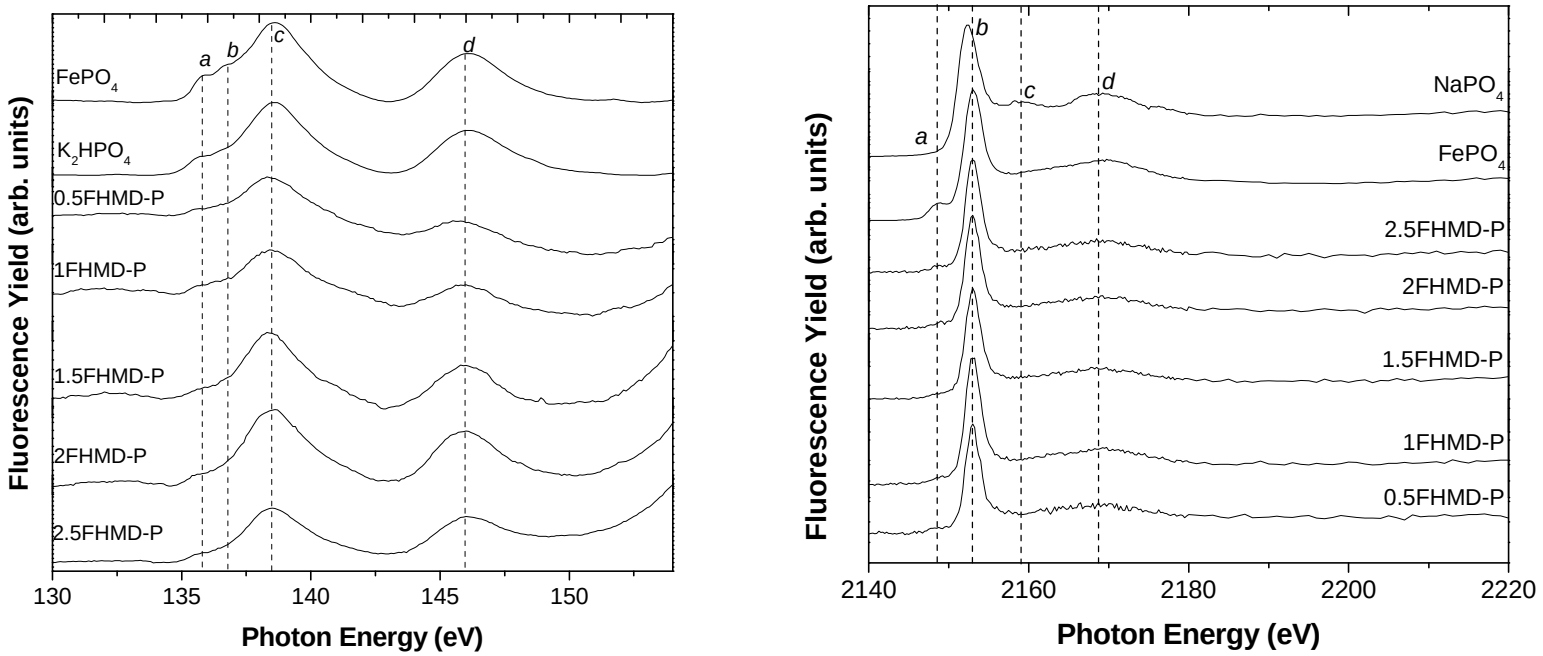

(a) (b)

Figure 5.17 Phosphorus XANES spectra for adsorbed phosphate onto FHMD and synthesized ferrihydrite, (a) L-edge spectra of FHMD-P; (b) K-edge spectra of FHMD-P

5.4 Application of Ferrihydrite-Modified Diatomite to Phosphorus Control

5.4.1 Removal of Phosphorus from Lake Water

The percent removal of total phosphorus (TP) from the Jackfish lake water using FHMD is shown in Figure 5.18a. The TP removal curve follows a saturation function. This suggests the removal of P proceeds through an adsorption process between the surface of FHMD and P; namely, the main mechanism of P removal from the lake water is P coprecipitation by FHMD. As shown in Figure 5.18a, increasing the FHMD dose increases the TP removal efficiency. An FHMD dose of 250 mg/L affords a TP removal efficiency of 88% and leaves a residual TP concentration of 17.0 µg/L, which falls within the oligotrophic TP range (3.0-17.7 µg/L) (Wetzel 2001). However, when the dose of FHMD is greater than 300 mg/L, the TP removal efficiency is consistently greater than 90% and the residual TP concentration is below 14.0 µg/L. Even if FHMD achieves TP removal efficiencies greater than 90%, it is expected that FHMD can further improve the P binding capacity of the sediment because the FHMD has not yet reached the adsorption equilibrium state.

Figure 5.18b shows that a linear increase ($Y = 2.59 + 0.00651X$) in dissolved Si is highly correlated with an increasing dose of FHMD (R^2=0.81, P<0.001). The increase in dissolved Si could be attributed to the partial dissolution of SiO_2 from the diatomite in the lake water. Silica-limited diatom production increases as a result of increased silica loading. In this study, the exponential growth of diatoms ($LogY = 5.68 + 0.00197X$, R^2=0.77 and P<0.001) due to the addition of FHMD is shown in Figure 5.18c. Diatom growth consumes more P and then further decreases P concentration in the lake water following P coprecipitation. More importantly, the stimulated diatom growth could contribute to the control of unwanted cyanobacteria blooms, favourably shifting the algae community from cyanobacteria- to diatom-dominant (Klapper 2003).

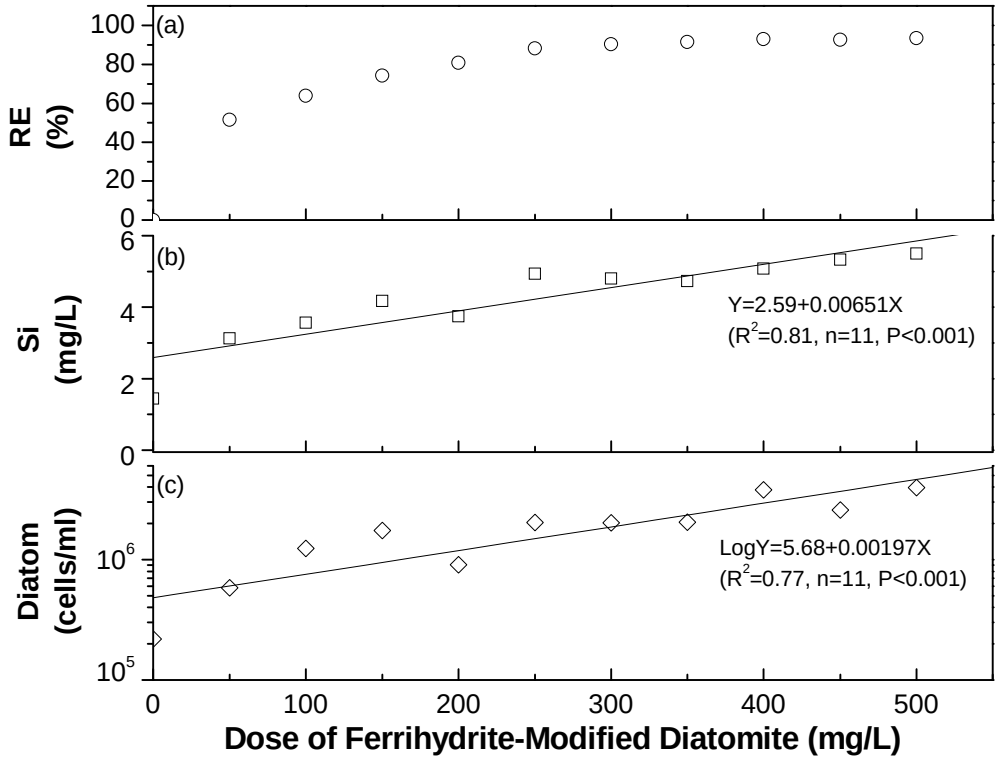

Figure 5.18 (a) Total dissolved phosphorus removal curve; (b) dissolved Si; (c) diatom growth

5.4.2 Sedimentation Rate

Phosphorus coprecipitation occurs when dissolved phosphorus is adsorbed onto the solid surface and even incorporated as a minor component in a solid phase, then that phase itself is settled (Drever 1988). FHMD has been demonstrated to be an effective adsorbent for P due to its adsorption capacity of 37.3 mgP/g and a high affinity for P (Xiong and Peng 2008b). Sufficient reaction time is required for the adsorption of dissolved P and the coagulation and flocculation of particulate P onto the surface of FHMD. Retention time and sedimentation rate of FHMD in lake water is critical for P removal through P adsorption onto FHMD. Sedimentation rate (SR) is the rate at which particles and colloids fall to the bottom of a tube over time. In this thesis, sedimentation rate is represented by the following equation:

$$SR = \frac{(Turbidity_1 - Turbidity_2)}{(t_2 - t_1)} \quad [5.4]$$

Figure 5.19a shows the turbidity of lake water treated by FHMD returns to original lake water values in 120 hours (5 days) (7.96 NTU for FHMD treated water vs. 7.57 for original lake water), and is further reduced to 1.42 NTU in 144 hours (6 days). FHMD's net positive surface charge at the lake water pH of 8.55 plays a significant role in the destabilization and aggregation of negatively charged colloids and sestons that contain particulate organic phosphorus (HDR Engineering 2001). This indicates the coagulation and flocculation of colloids and sestons initiated by the addition of FHMD contributes to increased lake water clarity.

As shown in Figure 5.19b, the SR in lake water treated by FHMD is greater than lake water treated by raw diatomite in the first 6 hours; both SRs are almost the same after 6 hours. FHMD is formed through ferrihydrite deposition into the diatomite pores. The specific density of ferrihydrite and raw diatomite are reported to be ~3.8 and ~0.19 g/cm^3, respectively. The higher specific density of FHMD results in its higher SR in the first 6 hours. The same SRs after 6 hours should not be the SR of either FHMD or diatomite, but may be the SR of natural colloids and sestons at 5 cm below the water surface. FHMD appears to completely settle through the 5 cm water layer within 6 hours. As a result, the low sedimentation rate of FHMD is capable of providing sufficient reaction time for P adsorption onto the surface of FHMD (72 hours are required to reach the adsorption equilibrium (Xiong and Peng 2008b)) in 5.5 m of Jackfish lake water column.

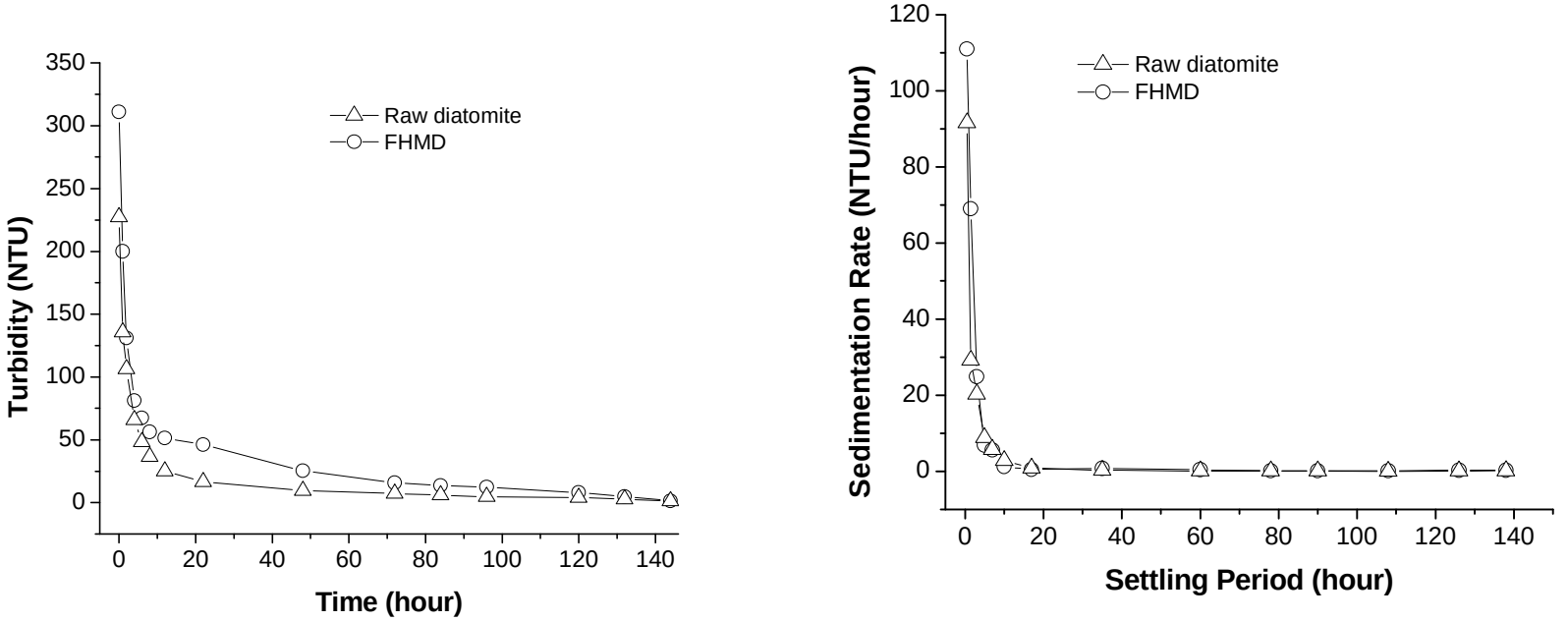

(a) (b)

Figure 5.19 Turbidity changes (a) and sedimentation rates (b) in lake water treated by raw diatomite and FHMD with time

5.4.3 Anoxic Incubation of Lake Water and Sediment Treated by Ferrihydrite-Modified Diatomite

Phosphorus release from sediments is very complicated, and is controlled by a series of abiotic and biotic processes (Khoshmanesh et al. 2002), with dissolved oxygen (DO) playing an important role. Under anoxic conditions, P stored in the surface sediment can potentially become mobile. $Fe_3(PO_4)_2$ dissolves following the reduction of Fe(III), and results in the simultaneous release of Fe^{2+} and PO_4^-. PO_4^- diffuses into the sediment porewater or upwards towards the overlying water. FeS and FeS_2 are the terminal sinks for Fe in anoxic sediments, thus excluding Fe as a reactive partner from the Fe-P-S system (Gächter and Müller 2003). Under anoxic conditions, degradation of aerobic bacteria leads to the mineralization of organic bound P where organic-P is degraded into poly-P then hydrolyzed into orthophosphate.

To evaluate the effects of anoxia on P release from sediments and determine the optimal dose of FHMD to remove P from lake water and bind P in sediments, lake water and sediments were incubated for 30 days under anoxic conditions. Changes in SRP and TP concentrations in the lake water without or with the addition of FHMD during this period are shown in Figures 5.20a and 5.20b, respectively. The SRP concentration in lake water without the addition of FHMD slightly decreases in the first two weeks from 24.6 to 19.6 µg/L; in the subsequent two weeks SRP concentration increases from 19.6 to 34.2 µg/L (Figure 5.20a). As shown in Figure 5.20b, the lake water TP concentration shows a pronounced increase from 78.9 to 101.5 µg/L. The slight decrease in SRP concentrations in the first two weeks is attributed to the seston sedimentation and the P binding capacity of the sediment. The large increases in SRP and TP might have been due to P release from sediments induced by the exhaustion of sediment P-binding capacity and the mineralization of organic bound P under anoxic conditions, which significantly influences P release from sediments.

As described in Section 5.4.1, TP removal efficiency achieved with a dose of FHMD greater than 300 mg/L is above 90%. FHMD doses ranging from 300 to 600 mg/L were

employed for the anoxic 30-day incubation. The maximum SRP and TP concentrations in lake water treated by 300 mg/L of FHMD were 14.5 and 26.9 µg/L, respectively (Figures 5.20a and b). The maximum SRP concentrations observed in the lake water following treatment with 400, 500, and 600 mg/L of FHMD were less than 10 µg/L (Figure 5.20a). In the lake water treated by 400, 500, or 600 mg/L of FHMD, the initial TP concentrations were the highest observed during the 30-day incubation period, at less than 15 µg/L (Figure 5.20b). Compared with the SRP and TP concentrations in untreated lake water, SRP and TP in lake water treated by FHMD are markedly lower during the anoxic 30-day incubation of lake water and sediment treated by FHMD. This suggests that FHMD can not only remove P from the water column but also improve the P binding capacity of sediment.

Figure 5.20a shows that SRP in lake water treated by 300 mg/L of FHMD increases with incubation time; no change in SRP in lake water treated by 400 mg/L of FHMD was observed, and SRP in lake water treated by 500 or 600 mg/L of FHMD decreased slightly with time. The slight decrease in the SRP achieved by the 500 and 600 mg/L FHMD doses might have been attributed to the extra binding capacity introduced by the addition of large amounts of FHMD; the increase in the SRP of lake water treated with 300 mg/L of FHMD would have been attributed to the insufficient P binding capacity at the low dose of FHMD. As seen in Figure 5.20b, TP concentration in lake water treated by 300 mg/L of FHMD increases from an initial concentration of 17.1 µg/L to 26.9 µg/L on day 30. The magnitude of this increase (9.8 µg/L) is much lower than the TP increase observed in the control sample (22.6 µg/L). P released from sediments under anoxic conditions is speculated to be bound by FHMD, so the magnitude of P release is greatly reduced compared with the untreated sample. The spontaneous binding of labile P by FHMD depends primarily on the adsorption and the total quantity of FHMD and on the mobile-P pool in sediments. After the capacity of the FHMD is exhausted, further labile P is released as demonstrated by the P release from the sediment treated by 300 mg/L of FHMD. During the 30-day incubation period, the TP concentration of lake water treated by 400, 500, and 600 mg/L of FHMD decreased slightly, suggesting that 400, 500, and 600 mg/L of FHMD are sufficient to bind mobile-P in sediments. Thus,

400 mg/L FHMD was determined to be the amount of FHMD required to remove P from lake water and inhibit P release from sediment.

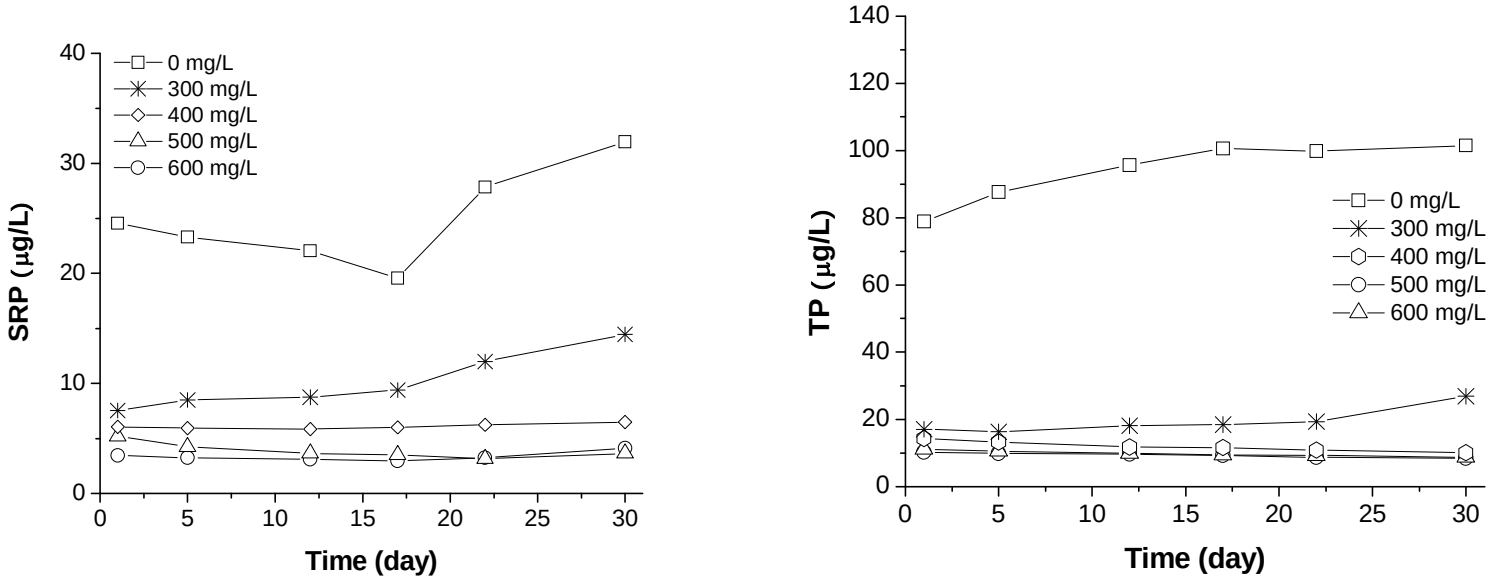

(a) (b)

Figure 5.20 Changes in soluble reactive phosphorus (SRP) concentrations (a) and total phosphorus (TP) concentrations (b) in the lake water treated by FHMD in the 30-day anoxic incubation

Fractional P composition of control and FHMD-treated sediments are shown in Figure 5.21. Interestingly, the addition of FHMD changes the sedimentary P pools. The labile-P fraction of sediments treated with FHMD is significantly lower than control sediment. The labile P fraction, also known as dissolved P in sediment pore water, is of particular interest as this P form may be immediately available for phytoplankton growth and is directly involved in P release from sediments. Dissolved P in sediment pore water is speculated to be adsorbed by FHMD, resulting in a decrease in labile P concentrations. The decreased labile P pools in sediments treated with FHMD decrease the extent of P release from sediments and the amount of bioavailable P in sediments. The labile P concentration in the sediment treated by 300 mg/L of FHMD is slightly higher than those of sediments treated with doses greater than 400 mg/L of FHMD, which is consistent with the above-mentioned finding that SRP and TP concentrations in lake water treated by 300 mg/L of FHMD is higher than at other doses.

The Fe-P fractions in sediments treated with FHMD are significantly higher than control sediments, which is consistent with a high amount of P adsorbed by FHMD from both the lake water and sediment. The Fe-P fractions of sediments treated with FHMD at concentrations of 400, 500, and 600 mg/L are higher than sediments treated with 300 mg/L of FHMD; however, Fe-P fractions in sediments treated with these doses of FHMD do not show a marked increase with dose. This is consistent with the above-described observation that a FHMD dose of 400 mg/L of FHMD yields comparable results to doses of 500 or 600 mg/L.

Al-P fractions in sediments treated with FHMD are comparable to the control sediment, except for a slight increase noted in sediments treated with 400, 500, and 600 mg/L of FHMD. Al-P fractions are not redox sensitive and are consequently relatively stable in lakes with anoxic hypolimnia, and are generally recognized as inert P (Rydin and Welch, 1998). Similar Al-P fractions indicate that aluminium (hydr)oxides may be exhausted with no further adsorption of P, or P is preferably adsorbed by FHMD.

Organic-P fractions are decreased in FHMD-treated sediments compared with control sediment. Organic-P is an important portion of P in sediments and is potentially bioavailable to algae (Zhou et al. 2008). Organic-P pools decrease with the addition of FHMD; FHMD is speculated to promote the mineralization of organic matter and further adsorbs the released P. Rydin and Welch (1998) report that organic-P, the largest pool in Lake Vallentuna sediments, did not decline after adding surplus alum.

Ca-P and residue-P fractions in FHMD-treated sediments are not significantly different than control sediments. The Ca-P fraction is generally recognized as a refractory P fraction because P is incorporated into the crystal structure of Ca minerals, forming Ca-P minerals such as hydroxyle apatite ($Ca_5(OH)(PO_4)_3$) and dicalcium phosphate ($CaHPO_4.2H_2O$) (Berg et al., 2004). Residue-P comprises mainly refractory organic P as well as an inert inorganic P fraction (Rydin 2000).

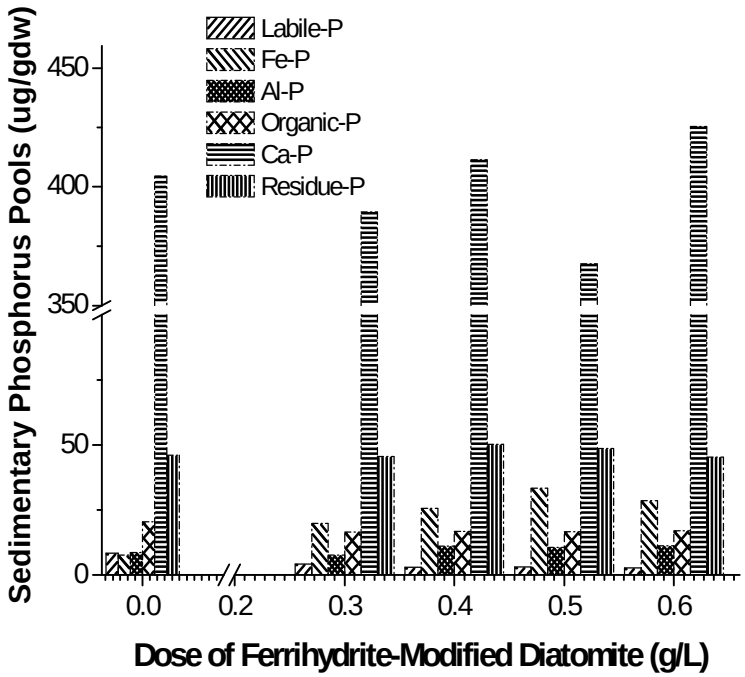

Figure 5.21 Phosphorus composition of control and FHMD-treated sediments

5.4.4 Anoxic Incubation of Lake Water and Sediment Treated by Ferrihydrite-Modified Diatomite and Alum

P inactivation by aluminium sulphate (alum) addition is a common chemical treatment for limiting P release from sediments (Hullebusch et al. 2002). P in sediments is adsorbed by flocs of aluminium (hydr)oxides that are formed through alum hydrolysis at pH 6 to 8 and have a high capacity to adsorb large amounts of inorganic P (Steinman et al. 2004). Al-P is generally recognized as a relatively inert P that is more stable than mobile P. The Al-P fraction increases markedly and becomes a major part of sedimentary P through the following processes associated with alum addition. Labile P including original labile P dissolves in interstitial water, P derived from mineralization of organic-P, and P produced from ferric phosphate reduction can be adsorbed onto the surface of aluminium hydroxide precipitates. Aluminium (hydr)oxides and ferric (hydr)oxides are two primary natural P adsorbents in lake sediments. Competition between these two adsorbents for P from sediments could occur especially when both are present in similar amounts. FHMD is an effective P adsorbent with a specific surface area of 211.1 m^2/g and a strong affinity for P (Xiong and Peng 2008b). FHMD has been demonstrated to have a high P-binding capability under anoxic conditions. Investigating the performance of FHMD on binding P in the presence of alum is essential for evaluating the stability of the P-binding ability of FHMD under anoxic conditions.

Alum solutions with logarithmic ratios of Al to mobile P + coprecipitated P of 0, 0.5, 0.8, 1.1, 1.4 and 1.7 were added to lake water and sediments treated with 400 mg/L of FHMD and incubated in the dark at room temperature under anoxic condition for 30 days. As shown in Figure 5.22a and 5.22b, SRP and TP show a similar decreasing trend over time during the incubation. SRP concentration decreased from a mean of 6.9 µg/L on day 1 to a mean of 1.9 µg/L on day 30; TP concentration decreased from a mean of 16.0 µg/L to a mean of 10.0 µg/L on day 30. Decreasing P concentrations in lake water indicate the effectiveness of both FHMD and alum in inactivating P and limiting P release from sediments. The magnitude of the P reduction over the entire incubation

period suggests the effect of FHMD on limiting P release is comparable to FHMD and alum solutions with logarithmic ratios of Al to mobile P of 0.5 and 0.8. Either the P-binding capacity of FHMD remains stable in the presence of alum or if P translocates from FHMD to alum should be further revealed by the analysis of the composition of sedimentary P. The combined treatment of FHMD and alum at logarithmic ratios of Al to mobile P of 1.1, 1.4, and 1.7 performed better with respect to P removal, and is attributed to surplus alum. The surplus Al^{3+} ions diffuse into the lake water and react with phosphate to form $AlPO_4$, or hydrolyze with hydroxyl ions (OH^-) to form $Al(OH)_3$, which can adsorb P from lake water (Rydin and Welch 1998).

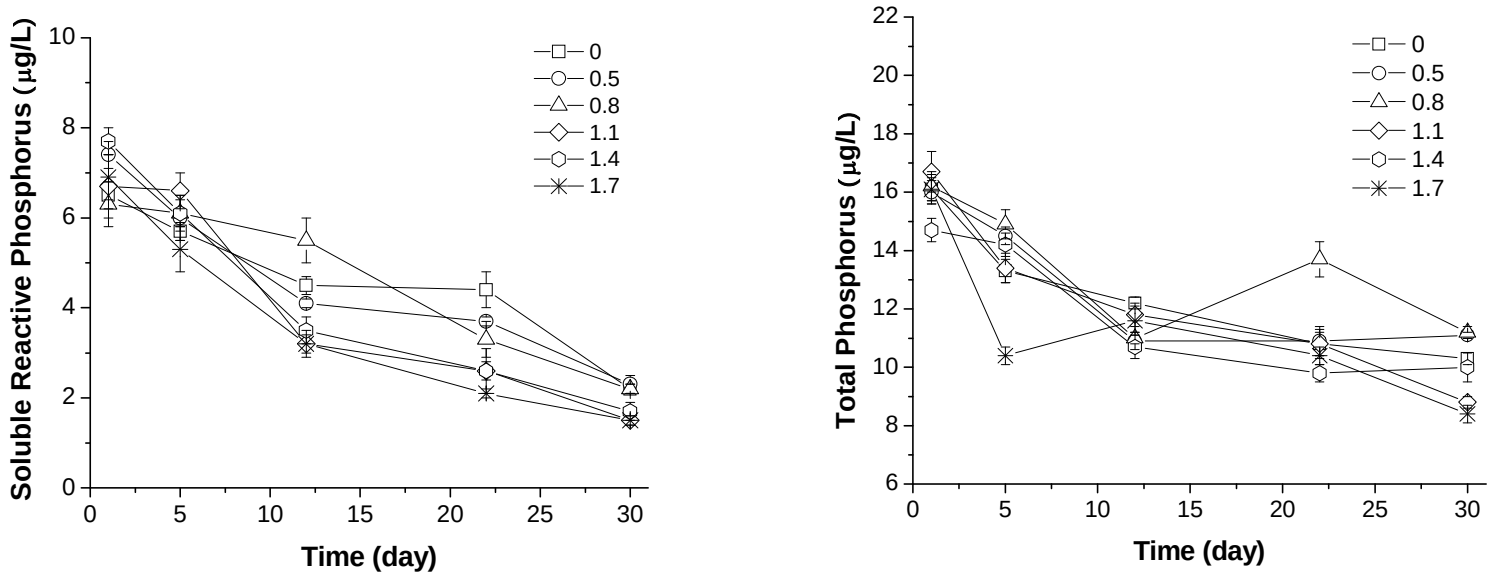

(a) (b)

Figure 5.22 Changes in soluble reactive phosphorus (SRP) concentrations (a) and total phosphorus (TP) concentrations (b) in lake water in the 30-day anoxic incubation of lake water and sediment treatment with FHMD and alum

P compositions of control sediment (400 mg/L FHMD only) and treated (400 mg/L FHMD and alum) sediments are shown in Figure 5.23. The labile-P fraction in sediments treated at logarithmic ratios of Al to mobile P of 0.5, 0.8, and 1.1 were low but comparable to controls; however, the labile-P fraction in sediments treated at logarithmic ratios of Al to mobile P of 1.4 and 1.7 are almost zero. This indicates that dissolved P in sediment pore water is preferably adsorbed by the high amounts of aluminum (hydr)oxides. As mentioned before, this labile P fraction is considered to be readily available to phytoplankton. Fe-P fractions in sediments treated at logarithmic ratios of Al to mobile P of 0.5 and 0.8 are comparable to control sediments. Fe-P fractions decrease with alum dose at logarithmic ratios of Al to mobile P of 1.1, 1.4, and 1.7. This suggests FHMD strongly binds P at alum doses less than or equal to logarithmic ratios of Al to mobile P of 0.8, but at higher logarithmic ratios P translocation from Fe-P to Al-P occurs. The strong P binding by FHMD at the lower logarithmic ratios agrees with the observation above that the ability of FHMD to limit P release is comparable to combined effects of FHMD and alum solutions at the lower logarithmic ratios of Al to mobile P of 0.5 or 0.8. Al-P fractions in treated sediments increase with the alum dose, which can be attributed to the increase of aluminium (hydr)oxides produced by the hydrolysis of alum. Organic-P fractions in treated sediments decrease with the alum dose, which suggests that the increased aluminium (hydr)oxides can promote the translocation of P from organic-P to Al-P under anoxic conditions. Comparison of control and treated sediments do not indicate clear trends with respect to Ca-P and residue-P fractions. As described before, Ca-P and residue-P fractions are recognized as refractory sedimentary P fractions, and remain stable during the sediment inactivation process.

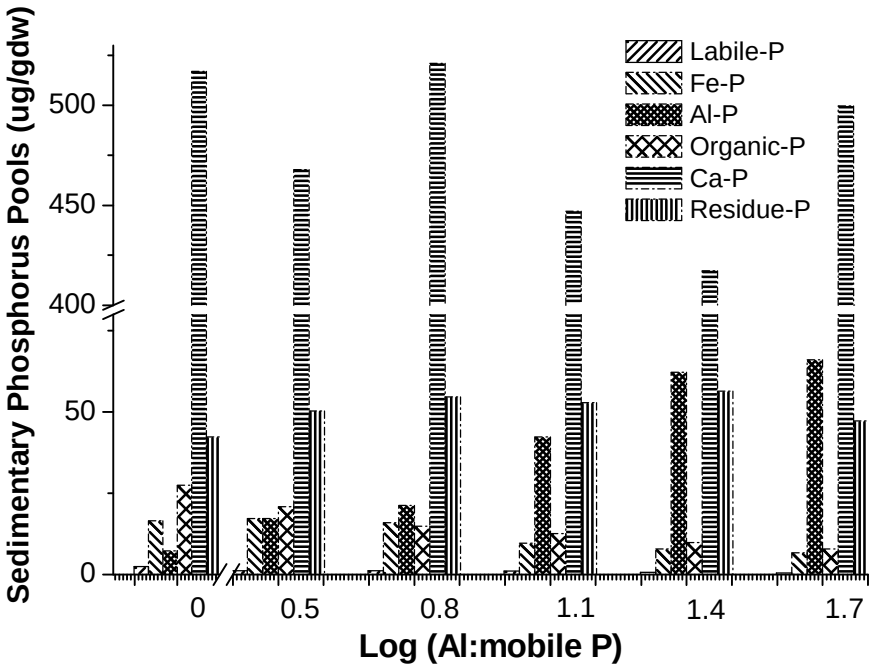

Figure 5.23 Sediment phosphorus compositions of control (400 mg/L FHMD only) and treated (400 mg/L FHMD and alum) sediments

5.4.5 Anoxic and Oxic Agitation

Under windy conditions, waves are produced and water currents move across the lake surface, resulting in the orbital movement of water particles at the surface. Wind produces not only the typical waves and currents observed at the surface of lakes but also induces much larger internal waves. When the height of an internal wave generated by wind-driven agitation is large enough, the orbital motion of water particles creates a shear stress on the lake sediment (Kalff 2002). When great enough, the shear stress moves the sediment particles and interstitial water to the water column (Laenen and LeTourneau 1996), leading to P release from sediments, turbidity increase, and inhibition of light penetration and primary production (Qin et al. 2004). Thus, sealing sediments to stabilize the sediment-water interface is essential for limiting the P release that results from bottom sediment resuspension. The addition of common sealing materials such as sand, clay, gravel, and silt can result in a large decrease in lake volume

and accelerates the lake aging process (Salonen and Varjo 2000). A more effective sealing material is therefore required to improve the success of *in situ* sediment sealing technologies. Gypsum was chosen to seal sediments in this study. Gypsum is a natural mineral with a specific gravity of approximately 2.3, and is expected to act as a sticky, low-density, physical barrier (Salonen and Varjo 2000). An *in vivo* experiemt was reported in Salonen and Varjo (2000) that gypsum was shovelled into the 5 m diameter test basins in Lake Enäjärvi located in southern Finland. This experiment found that the sticky gypsum layer not only prevents sediment resuspension and methanobacterial ebullition which are the main agents transporting P through the sediment/water interface but also improves the P-binding capacity of the sediment. Salonen and Varjo (2000) recommended the gypsum sealing as a promising lake sediment restoration technique. Negative effects of the gypsum sealing technique on benthic biota have not been reported yet. Thus, gypsum layers with different thicknesses (0.5, 0.8, 1, 1.2 cm) were tested.

The effects of agitation on turbidity of samples treated with FHMD and gypsum under anoxic and oxic conditions are shown in Figures 5.24a and 5.24b, respectively. Samples were agitated at 60 rpm from 0-12 hours, at 100 rpm from 24-36 hours, and 130 rpm from 48-60 hours. The samples were allowed to settle in the agitation intervals (i.e., 12-24 hours, 36-48 hours, and 60-72 hours). Lake water turbidity decreased slightly in the period from 0 to 48 hours. During the period from 0-48 hours, the agitation rates were 60 and 100 rpm. At agitation rates less than 100 rpm, no obvious sediment resuspension was observed, and particle sedimentation results in a decrease in water turbidity. In contrast, when the agitation rate was increased to 130 rpm, a distinct sediment resuspension was observed in the control sample without gypsum. The maximum turbidity observed in controls (sediment without gypsum layer) exceeds the maximum detection limit (1000 NTU) of the 2100 P Turbidimeter. However, Figures 5.24a and b show that gypsum effectively limits sediment resuspension resulting from agitation. The maximum turbidity in samples where sediments were sealed with a gypsum layer was 85.3 NTU under anoxic conditions and 104.3 NTU under oxic conditions. When the gypsum was added to the lake water, it settled to the bottom and accumulated on the

sediment to form a sticky layer. The sticky gypsum layer resists the force applied to the sediment by the agitating movement, thereby inhibiting sediment resuspension.

P exchange between the solid and solution phases is dependent on the P equilibrium between the phases (Koski-Vähälä et al. 2001). When a given amount of suspended sediment solids are mixed with an increasing volume of solution due to sediment resuspension, the P mobilization potential of the suspended material markedly increases, thereby increasing the P concentration in the solution. The effects of agitation on SRP of samples treated with FHMD and gypsum under anoxic and oxic conditions are shown in Figures 5.24c and 5.24d. As seen in Figure 5.24c, after agitation at less than 100 rpm in anoxic conditions, SRP values of samples treated with 0.8, 1, and 1.2 cm gypsum layers remained lower than samples treated with 0 (control) and 0.5 cm thick gypsum layers. After agitation at 130 rpm, the SRP of the control sample increased to 18.5 μg/L, far above values from samples treated with gypsum. SRP concentrations of samples with 0.8, 1, and 1.2 cm thick gypsum layers were substantially lower than samples with 0.5 cm thick gypsum layer. As seen in Figure 5.24d, after agitation at less than 100 rpm in oxic conditions, the SRP values of all samples continued to drop to below initial values. With agitation at 130 rpm, the SRP value for the control sample increased from 3.1 μg/L to 13 μg/L, a much larger increase than observed in samples treated with gypsum. The SRP of the sample with a 0.5 cm thick gypsum layer rose to 10.4 μg/L, higher than values of samples with 0.8, 1, and 1.2 cm thick gypsum layers (6.9, 6.4, and 6.5 μg/L), which remained below their initial values.

The agitation rate of 130 rpm had the most pronounced effect on sediment resuspension in samples without gypsum. However, even at this agitation speed, the turbidity and SRP concentration in samples treated with gypsum were much lower than controls. Thus, a sticky gypsum layer effectively stabilizes the sediment surface, prevents sediment resuspension, and consequently limits P release from sediments. Under both anoxic and oxic conditions, the turbidity and SRP concentration of the samples treated

with a 0.8 cm thick gypsum layer were the lowest, indicating 0.8 cm is the optimal gypsum layer thickness for stabilizing the sediment surface.

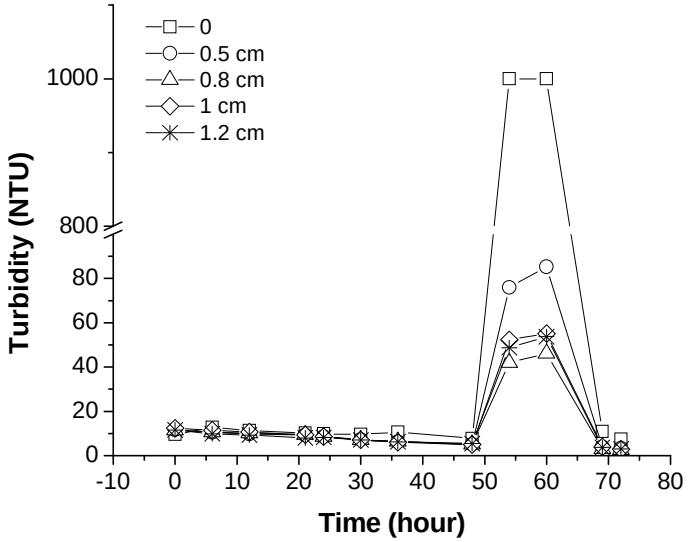
0
0.5 cm
0.8 cm
1 cm
1.2 cm
Turbidity (NTU)
1000
800
100
80
60
40
20
0
-10
0
10
20
30
40
50
60
70
80
Time (hour)

(a)

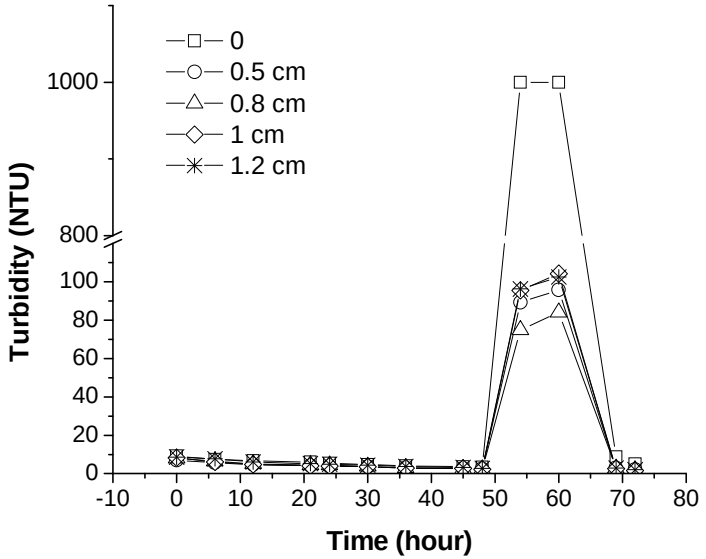
0
0.5 cm
0.8 cm
1 cm
1.2 cm
Turbidity (NTU)
1000
800
100
80
60
40
20
0
-10
0
10
20
30
40
50
60
70
80
Time (hour)

(b)

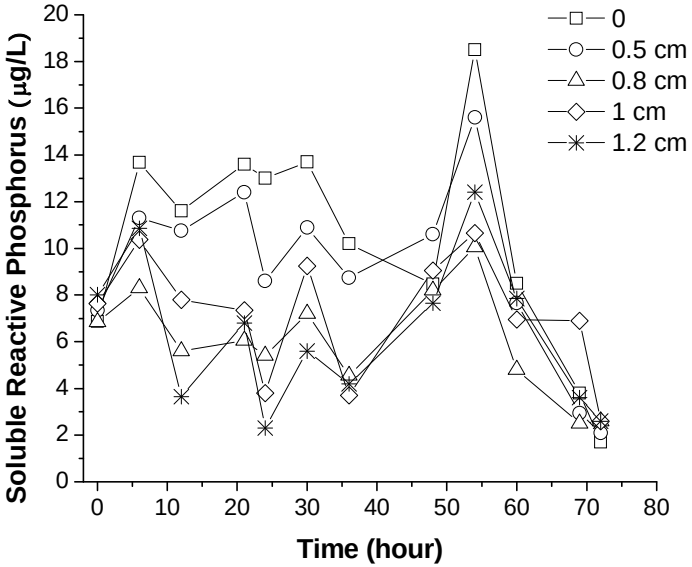

(c)

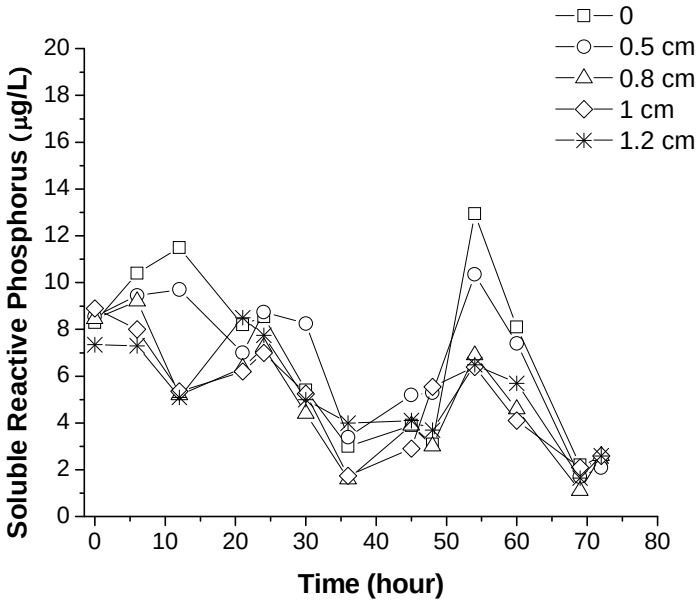

(d)

Figure 5.24 Effects of agitation on (a) turbidity under anoxic conditions; (b) turbidity under oxic conditions; (c) SRP under anoxic conditions; and (d) SRP under oxic conditions

5.4.6 Anoxic and Oxic Incubations

A lack of stable long-term thermal stratification is one of the features of shallow lakes (Cooke et al. 1986). Short lasting thermal stratification can form under calm, warm weather conditions, and can be readily disrupted by wind action. In temporary stratification, DO stored in the hypolimnion can be rapidly consumed by microbial activity because shallow lakes have a low oxygen storage capacity (Ruley and Rusch 2004). A subsequent breakdown of stratification due to wind-induced turbulence improves the diffusion rate of oxygen across the water surface and introduces DO into anoxic bottom waters through the water circulation (Kalff 2002). Changes between anoxic and oxic conditions frequently occur in shallow lakes in summer. As discussed previously, dissolved oxygen (DO) plays a significant role in P release from sediments. Thus, it is necessary to investigate P release from sediments treated with FHMD and gypsum under either anoxic or oxic conditions.

Experiments described above determined the optimal dose of FHMD for removal of P from lake water and improving the P binding capacity of sediments to be 400 mg/L. The optimal thickness of gypsum applied to stabilize the sediment was determined to be 0.8 cm. Thus, lake water and sediment treated with 400 mg/L of FHMD and a 0.8-cm-thick gypsum layer were incubated under either anoxic or oxic conditions for 30 days. Changes in TP in lake water during the incubation time under anoxic and oxic conditions are shown in Figures 5.25a and b, respectively. During the 30-day incubation period, TP concentration decreased with time in both oxic and anoxic conditions. The initial TP concentrations in the anoxic and oxic incubations were 14 and 15.8 µg/L, respectively. On day 30, final TP concentrations in the anoxic and oxic incubations were 10.8 and 9.5 µg/L, respectively. The more pronounced decrease in TP under oxic (6.3 µg/L) vs. anoxic (3.2 µg/L) conditions could be attributed to the formation of more Fe^{3+} particulate and subsequent precipitation of P, P uptake by sediment bacteria, and/or lower initial TP concentrations in the anoxic incubation. Under oxic conditions, more ferric iron ions are formed in lake water (Braun 1997). When P is present, P and Fe(III) particulates coprecipitate, either as $FePO_4$ or adsorb onto ferric oxides and ferric

hydroxides (Griffith et al. 1973). Under oxic conditions, poly-P accumulating organisms in sediment take up orthophosphate and store it as poly-P in cells (Khoshmanesh et al. 2002). For lake water and sediment treated with FHMD and gypsum, no P release seems to occur regardless of oxic or anoxic conditions. Oxic conditions are more favourable for P retention in sediments than anoxic conditions.

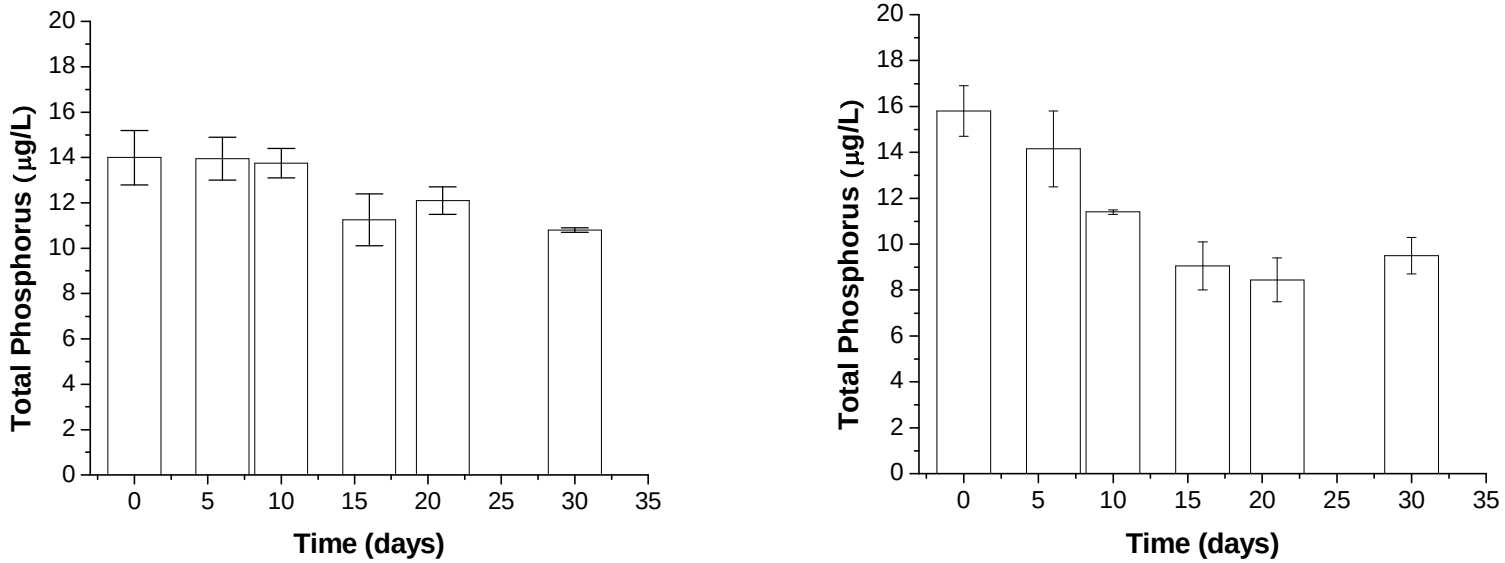

(a) (b)

Figure 5.25 Changes in total phosphorus (TP) concentrations in lake water with the incubation time under anoxic (a) and oxic (b) conditions

5.4.7 Phosphorus Control in an Artificial Aquarium

As described in Chapter 4, three artificial aquariums (one control, two treated with identical conditions) were established in an environmental chamber to investigate the effects of the application of FHMD and gypsum on P control. The aquariums did not receive any external nutrient input. Pure nitrogen was introduced at approximately 1 cm above the aquarium sediments to produce anoxic conditions. A metal grid oscillated vertically in the aquariums for 15 minutes every day to produce an internal wave. The aquariums were set up to simulate critical environmental conditions in shallow lakes, including oxygen depletion during periods of temporary thermal stratification and sediment resuspension associated with periods of overturn. These two environmental conditions are also critical for P release from the sediments. P release from the sediments can occur via two different mechanisms: 1) release at the sediment-water interface during periods of anoxia or hypoxia, and the subsequent diffusion of dissolved P into the water column; and 2) wind-induced resuspension at the sediment surface, whereby either the sediment pore water P can be released into the water column or the P adsorbed to sediment particles can desorb into the water column (Steinman et al. 2004).

5.4.7.1 Changes in dissolved oxygen in the aquariums

To simulate anoxic conditions caused by temporary thermal stratification in shallow lakes, pure nitrogen was introduced at a depth of 1 cm above the sediments of the three aquariums for five minutes to maintain anoxic conditions (DO < 1 mg/L; Ruane and Mobley 2002). As shown in Figure 5.26, DO levels in both the control and the treatment aquariums dropped to less than 1 mg/L after the 28^{th} day. DO levels in the treatment aquarium represented in Figure 5.26 are the average of DO levels in the two test aquariums. During the first 28 days, DO levels in the three aquariums dropped dramatically from 7.4 and 7.6 mg/L to 0.93 and 1 mg/L, respectively. During the period from 28-120 days, DO levels in the control aquarium and the treatment aquariums gradually decrease from 0.84 and 0.89 mg/L to 0.5 and 0.54 mg/L, respectively. The slow decrease in the DO level is ascribed to both the 5-minute addition of nitrogen and

the vertical oscillation of the metal grid in the aquariums. A rapid decrease in DO levels can lead to the mortality of lake biota. The water movement induced by the metal grid oscillation enhanced the rate of oxygen dissolution into the water from the air and facilitated the exchange of oxygen rich water at the surface with water from depth containing less oxygen. During the 120 day period, a decrease in DO in all three aquariums is representative of DO variation in a lake.

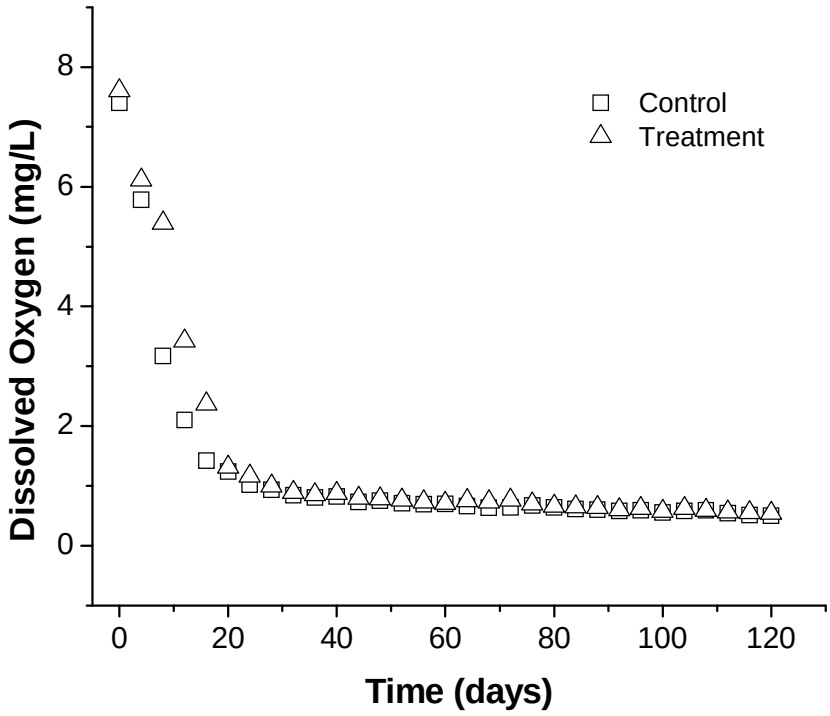

Figure 5.26 Changes in dissolved oxygen in control and treatment aquariums with the addition of nitrogen

5.4.7.2 Changes in the concentration of total suspended solids

Figure 5.27 illustrates that the oscillation occurring on day 1 caused a higher total suspended solids (TSS) concentration in the control aquarium (127 mg/L) than in the treatment aquariums (5 mg/L). The TSS concentration in the treatment aquarium represents the average of TSS concentrations in two treatment aquariums. The

oscillation of the metal grid had pronounced effects on sediment resuspension in the control aquarium. As a result of sediment resuspension, numerous sediment particulates were observed floating in the water column. Daily oscillation of the metal grid produced an accumulation of suspended solids and a consequent increase in the TSS concentration (Figure 5.27). The TSS concentration in the control aquarium increased from 127 to 725 mg/L over the 120 day incubation period. However, the TSS concentration in the treatment aquarium only rose from 5 to 25 mg/L, demonstrating that the 0.8 cm-thick gypsum layer effectively reduced the effect of the oscillation on sediment resuspension.

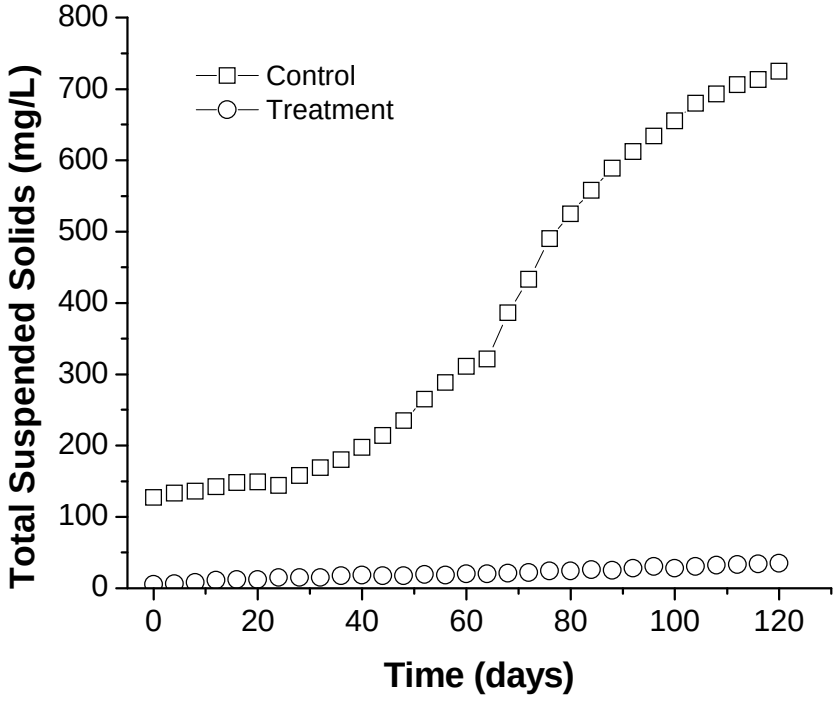

Figure 5.27 Changes of total suspended solids (TSS) concentration in the control and treatment aquariums

5.4.7.3 Changes in sulphate concentration

Figure 5.28 indicates that after 120 days of incubation, SO_4^{2-} concentrations in the lake water in the control aquarium decreased slightly from the 0.95 to 0.82 g/L; this was

attributed to sulphate ions acting as electron acceptors to oxidize organic matter under anoxic conditions. Products of SO_4^{2-} reduction, such as S^- and S^{2-}, can react with ferrous iron to form permanent sinks of iron, such as FeS_2 and FeS. This can stimulate ferric reduction, so more P bound by colloidal iron in the water and more Fe-P in the suspended sediment particles would be released to the water. The SO_4^{2-} concentration was relatively stable in the treatment aquariums during the 120 day incubation. The mean SO_4^{2-} concentration in the treatment aquarium (1.82 g/L) was 1 g/L higher than in the control aquarium, and was attributed to the partial dissolution of gypsum in the water. The relatively stable SO_4^{2-} concentration indicates that SO_4^{2-} ions in the sediment and water reach equilibrium. SO_4^{2-} ions diffusing into the water from the sediment could compensate for the consumption of SO_4^{2-} ions in the water as an electron acceptor under anoxic conditions and/or as a reactant contributing to particulate formation.

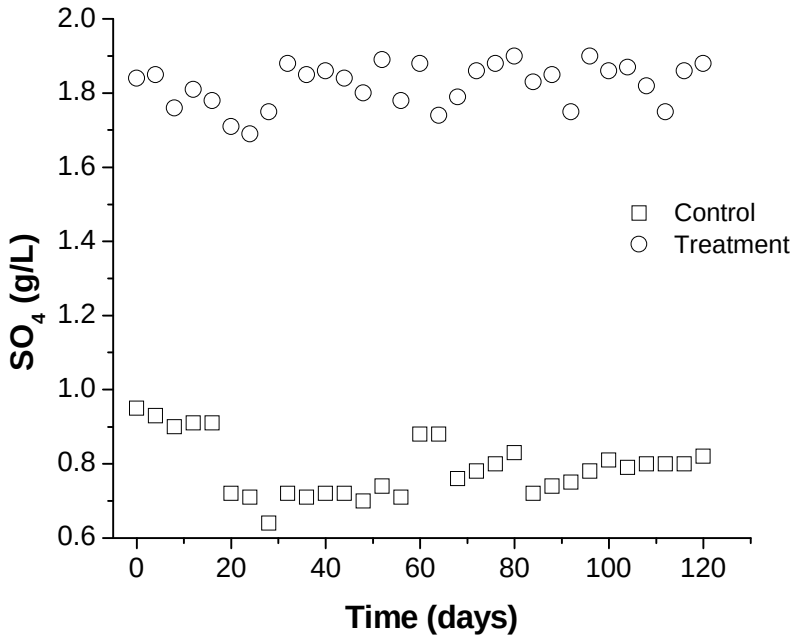

Figure 5.28 Changes in sulphate (SO_4^{2-}) concentrations in the control and treatment aquariums

5.4.7.4 Changes in total kjeldahl nitrogen concentration

As shown in Figure 5.29, total kjeldahl nitrogen (TKN) concentrations do not substantially differ between the control and treatment aquariums. TKN is a combination of organically bound nitrogen and ammonia. The similar TKN concentrations suggest that FHMD and gypsum cannot remove organically bound nitrogen and ammonia. Moreover, as discussed above (Section 5.3.3), FHMD shows a higher affinity for P than for nitrate (NO_3^-). Thus, FHMD does not seem to have a strong capacity to remove total nitrogen. This means that application of FHMD could result in an increase in the N:P ratio by removing P but not N, thereby reinforcing P limitations. N-fixing cyanobacteria are favoured under low-nitrogen conditions (Kalff 2002), which means that abundant N could limit the growth of N-fixing cyanobacteria. When FHMD and gypsum are applied to a eutrophic lake in spring, it is speculated that magnitude of the bloom of N-fixing cyanobacteria could be reduced in summer.

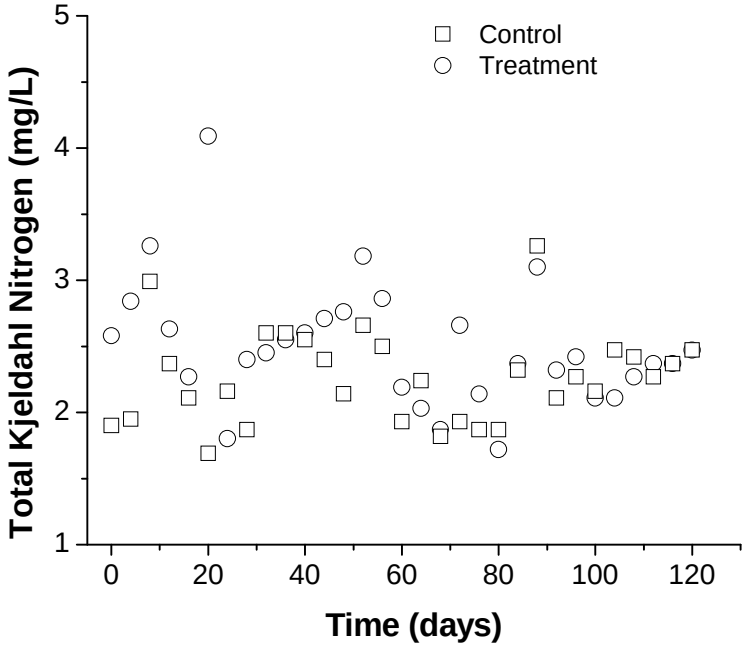

Figure 5.29 Changes in the total kjeldahl nitrogen (TKN) concentrations in the control and treatment aquariums

5.4.7.5 Changes in dissolved Si concentration

Dissolved Si concentrations in the treatment aquariums were stable (Fig. 5.30), and are attributed to the combined effect of reduced sediment resuspension and low diatom Si uptake. As discussed above, the sticky gypsum layer effectively limited sediment resuspension caused by the oscillation of the metal grid. Reduced sediment resuspension results in low Si release from the sediment and only small increases in dissolved Si concentrations in the lake water. The limited P level in the lake water due to P removal by FHMD, P inactivation by FHMD, and reduced sediment resuspension by gypsum (discussed in a later Section) hinders the growth of phytoplankton, including diatoms, and therefore reduces their Si uptake. Thus, when the supply of Si from the sediment and the uptake of Si by the diatoms reach equilibrium, the dissolved Si concentration in the lake water remains stable.

In contrast, dissolved Si concentration in the control aquarium increased over the first 32 days, remained stable during the period from 32-72 days, then decreased in the period from 72-120 days. The initial increase is ascribed to Si supplied from sediment due to resuspension. The increased Si concentration, optimum temperature for diatom growth, and increased P concentration (discussed in a later Section) then promoted the growth of diatoms which consumed some of the dissolved Si. When the Si supply from the sediment and the Si uptake by the diatoms reached equilibrium, the dissolved Si concentration remained stable (period from 32-72 days). When the Si uptake by the diatoms continued to increase, the dissolved Si concentration began to drop (period from 72-120 days). Although the dissolved Si concentration in the control aquarium fluctuated during the incubation period, the dissolved Si concentration in the treatment aquariums was markedly higher (Figure 5.30), and was attributed to the partial dissolution of diatomite of FHMD.

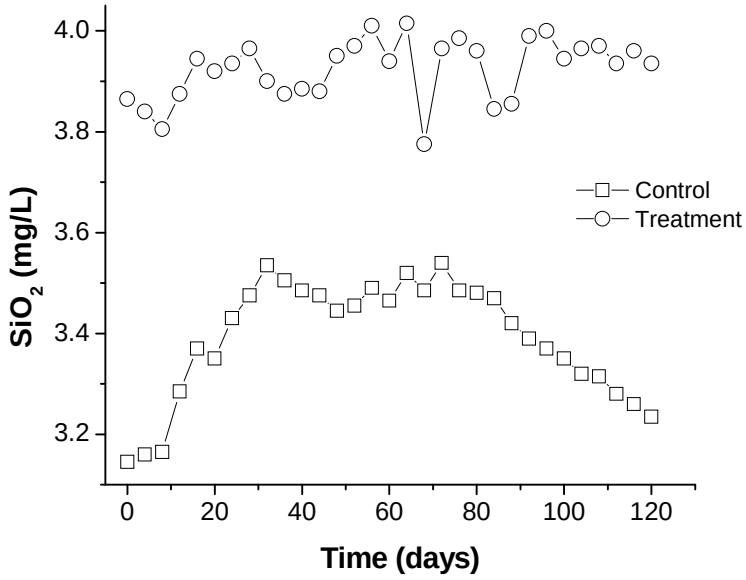

Figure 5.30 Changes in the dissolved Si concentrations in the control and treatment aquariums

5.4.7.6 Changes in diatom concentration

Figure 5.31 illustrates trends in diatom concentrations, which decreased in both the control and treatment aquariums over the 120-day incubation period. This decrease is mainly attributed to diatom sedimentation. To determine diatom concentrations in the lake water without interference from suspended sediment particles, water samples were collected three hours after the 15-minute oscillation of the metal grid. As the specific density of diatom frustules is nearly twice that of water, diatoms can be quickly lost through sedimentation under calm weather conditions (Kalff 2002).

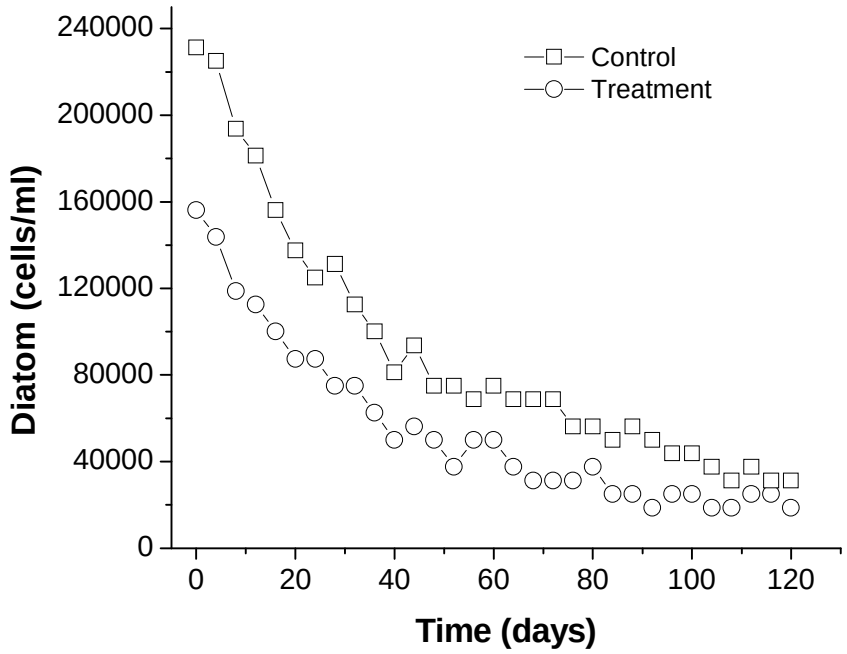

Figure 5.31 Changes in diatom concentration in the control and treatment aquariums

5.4.7.7 Changes in total alkalinity and pH

As shown in Figure 5.32a, total alkalinity in the treatment aquarium showed minor fluctuations around 344 mg$CaCO_3$/L. The relatively stable alkalinity in the treatment aquarium may be due to limited sediment resuspension. However, total alkalinity in the control aquarium increased over the first 28 days, and then decreased for the remaining incubation time. Changes in alkalinity in the control aquarium can be attributed to sediment resuspension. Salt ions contained in the surface sediment are released into the water with sediment resuspension, thereby increasing alkalinity in water. With the onset of anoxic conditions on the 28th day (see Section 5.4.7.1) was sediment acidification. When acidified surface sediment is introduced into the water column, total alkalinity in water will decrease. Moreover, higher alkalinity in the treatment aquarium is due to the addition of FHMD and gypsum.

Correspondingly, as seen in Figure 5.32b, higher pH in the treatment aquarium is attributed to the addition of FHMD and gypsum. As shown in Figure 5.32b, pH values in the control and treatment aquariums remain stable as a total alkalinity of more than 100 mg$CaCO_3$/L is able to stabilize the pH value in the water.

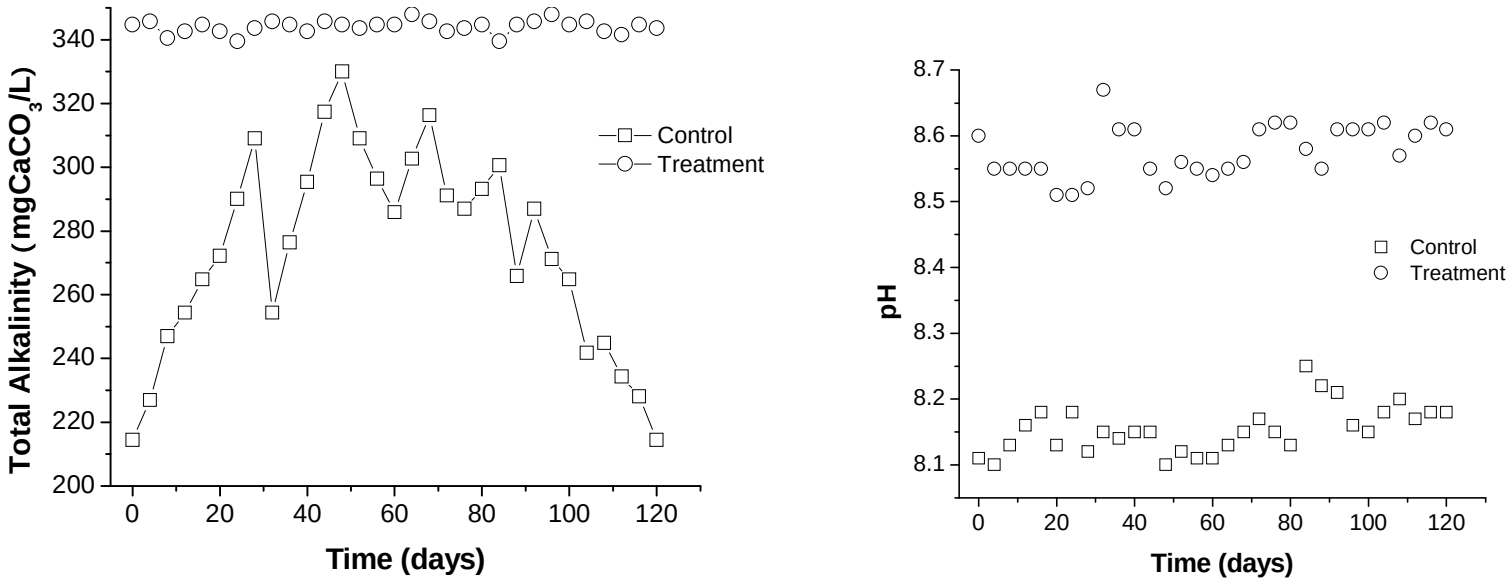

(a) (b)

Figure 5.32 Changes in the total alkalinity (a) and pH (b) in the control and treatment aquariums

5.4.7.8 Changes in total phosphorus concentration

TP levels in the control aquarium increased during the incubation period (Figure 5.33). The continuous increase in TP values is attributed to anoxic conditions and sediment resuspension. Under anoxic conditions, Fe-P complexes break down as the iron is reduced from ferric ions to ferrous ions, and P bound by iron is transformed into labile P. Organically bound P is also transformed into labile P due to the decomposition of organic matter under anoxic conditions. Under calm conditions, labile P dissolved in sediment pore water is diffused into the overlying water. Due to the internal wave caused by the metal grid oscillation, surface sediment is resuspended into the water. P bound to suspended sediment particles is desorbed because of the large ratio of water volume to particle mass.

TP levels in the control aquarium increased from an initial concentration of 108.3 µg/L to a final concentration of 174.2 µg/L. The final TP concentration is well above concentration needed to sustain hypereutrophic levels (Wetzel 2001). External nutrient sources were excluded from the aquariums, and therefore the internal P loading (P release from sediment into the overlying water) in the control aquarium was itself high enough to produce an increase in the TP concentration over the 120 day period. This finding further supports the notion before that, even if external P sources are completely excluded, lake recovery will not occur without controlling the internal P loading. No large cyanobacterial bloom was observed in the control aquarium despite TP levels rising from eutrophic to hypereutrophic. This is attributed to the low ambient temperature of 11 °C, which while optimal temperature for diatom growth is too cold for cyanobacterial growth (Konopka and Brock 1978). If the ambient temperature had been set to a more optimal temperature for cyanobacteria, the formation of a cyanobacterial bloom would have been expected.

In contrast to the continuous increase in TP concentrations in the control aquarium, TP levels in the treatment aquarium remained relatively stable and fluctuated within the range from 9.1-13.3 µg/L. This range is indicative of oligotrophic conditions and at a

limiting level for phytoplankton growth. Due to P removal by FHMD from the lake water, the P inactivation by FHMD in the sediment, and limited sediment resuspension by the sticky gypsum layer, the TP level in the lake water was reduced from an original value of 108.3 µg/L (eutrophic) to 12.9 µg/L (oligotrophic). Thus, the application of FHMD and gypsum is effective in the P control under anoxic conditions and in conditions favouring sediment resuspension. Anoxic conditions and sediment resuspension simulate environmental conditions in shallow lakes that result in self-accelerated eutrophication. As mentioned above, no external P source was employed in the aquarium experiments, demonstrating that FHMD and gypsum can be used for the control of eutrophication in shallow lakes without external nutrient sources.

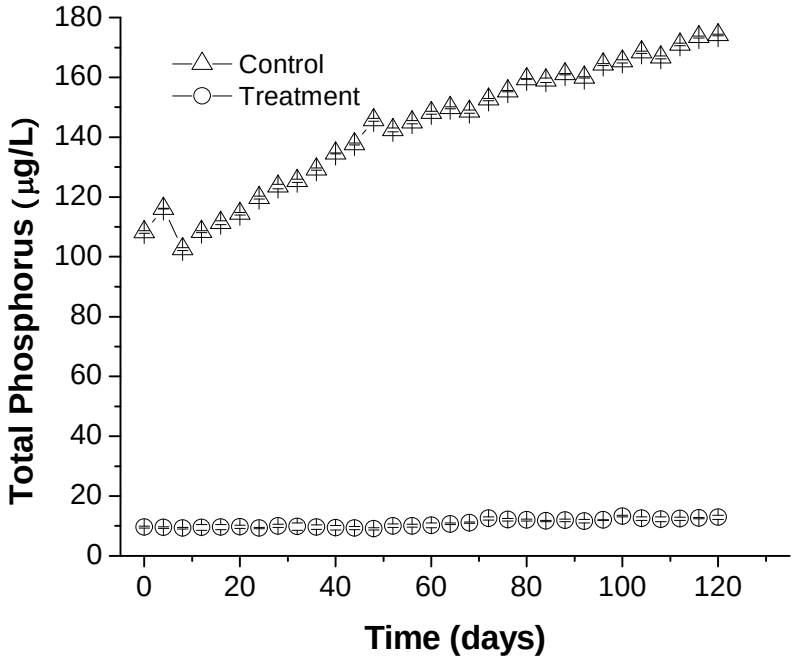

Figure 5.33 Changes in total phosphorus (TP) concentrations in the control and treatment aquariums

5.4.7.9 Changes in the depth profiles of sediment phosphorus fractions

The depth profiles of sediment P fractions in control sediment, and sediments from the treated aquarium at 60 and 120 days are shown in Figures 5.34a, b, and c, respectively.

As shown in Figure 5.34a, labile-P in the control aquarium sediment in general decreased with increasing depth. The water content of sediment usually decreases with sediment depth as a result of sediment compaction (Meadows et al. 2000). Thus, the concentration of dissolved P in deeper pore water is initially higher than in surficial pore water. The concentration gradient of labile P between the surface sediment layer and deeper sediment layers leads to labile-P diffusion from the bottom to the top of sediment and an absolute amount decrease as a function of depth. Accordingly, the Fe-P sediment fraction in the control aquarium displays a concentration decrease as a function of sediment depth. Sediment oxygen content decreases drastically with depth until it reaches depletion. Thus, the redox potential (Eh) values of sediment decrease with increasing sediment depth (Meadows et al. 2000). In the deeper sediments with low redox potential, Fe-P can be transformed into labile-P due to Fe(III) reduction, after which labile-P diffuses into the upper sediment layers. Compared to labile-P, and Fe-P, Al-P and organic-P are relatively stable. Al-P is a relatively refractory pool, which is supported by the finding of Rydin (2000) at Lake Erken where the Al-P concentration remained fairly constant throughout the sediment profile. Ca-P and residue-P increased with the sediment depth. Ca-P and residue-P are refractory pools and are diagenetic minerals, the precipitation of which is very common in nature.

As shown in Figure 5.34b, after 60 days, labile P in the treated sediments decreased with the sediment depth for the reasons described above. However, Fe-P was significantly elevated relative to control sediment. FHMD settling in the sediment not only adsorbs P from the water column but also continues to adsorb P from sediment, thereby causing the pronounced increase in Fe-P pools. The Fe-P sediment depth profile shows that the Fe-P concentration is the greatest at 2 cm depth due to the FHMD that settled on the near-surface sediment. Al-P is relatively stable; however, after 60 days, the Al-P in the treated sediment was lower than the control sediment. Lower Al-P can be attributed to a competition between FHMD and Al (hydr)oxides for P. As FHMD was present in significantly greater amounts than Al (hydr)oxides, P is preferentially adsorbed by FHMD. After 60 days, organic-P in the treated sediment had decreased as a function of sediment depth. The mineralization of organic matter is facilitated by anoxic conditions

and the activity of sulphate-reducing bacterial (SRB) stimulated by the presence of the gypsum. The mineralization of organic matter facilitates transformation from organic-P to labile-P, after which labile-P diffuses into the upper sediment layers. Ca-P and residue-P increase with the sediment depth for the reasons described above.

After 120 days, labile-P in the treated sediment was significantly lower than at 60 days or in the control sediment (Figure 5.34c). Fe-P was unchanged relative to values from 60 days. The highest Fe-P concentrations were still found in surface and near surface sediments, which demonstrates the strong P binding capacity of FHMD and the stability of FHMD under anoxic conditions. Al-P was also largely unchanged from 60 day values. Organic-P decreases as a function of the sediment depth as per the mechanism described above. Ca-P and residue-P continued to increase with the sediment depth throughout the 120 days.

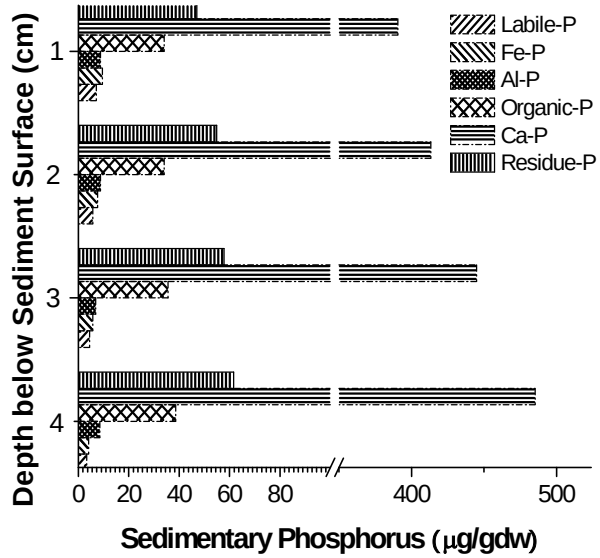
Depth below Sediment Surface (cm)
1
2
3
4
Labile-P
Fe-P
Al-P
Organic-P
Ca-P
Residue-P
0
20
40
60
80
400
500
Sedimentary Phosphorus (μg/gdw)

(a)

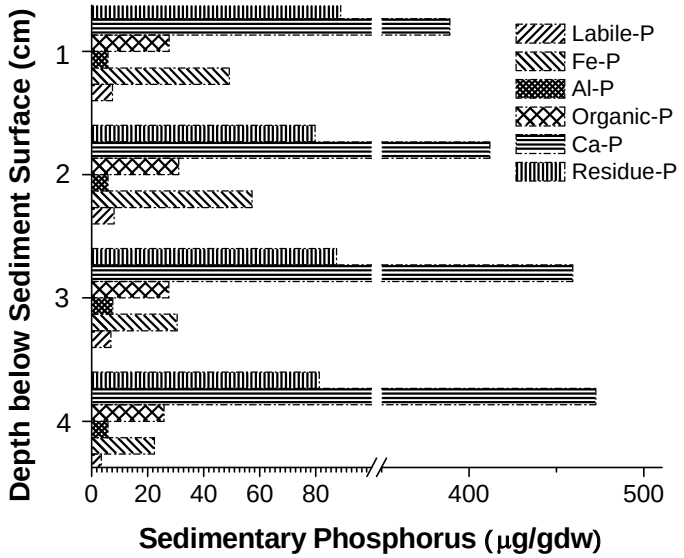
Depth below Sediment Surface (cm)
1
2
3
4
Labile-P
Fe-P
Al-P
Organic-P
Ca-P
Residue-P
0
20
40
60
80
400
500
Sedimentary Phosphorus (μg/gdw)

(b)

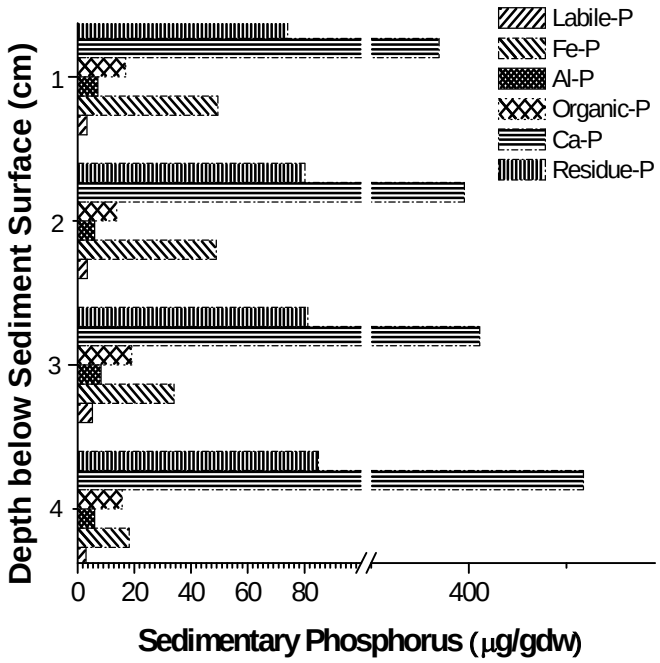

(c)

Figure 5.34 Sedimentary phosphorus depth profile in (a) control sediments, and treated sediments after (b) 60 and (c) 120 days

Chapter 6 – Conclusions and Recommendations

6.1 Conclusions

Eutrophication is often accompanied by cyanobacterial blooms and is a serious worldwide environmental problem. In-lake P control methods are commonly utilized to supplement removal of external nutrient sources and accelerate the reversal of the eutrophication process. Among a number of in-lake P control methods, P coprecipitation has been widely studied and tested since the 1970s. Until now, however, very few coprecipitants have been successfully developed. A new P coprecipitant, ferrihydrite-modified diatomite (FHMD), was developed in this research.

The primary objectives of this research were: to develop and characterize FHMD; to study the P adsorption behaviour and P adsorption mechanism of FHMD; to employ FHMD to remove P from lake water and limit P release from sediment under anoxic conditions; and to evaluate the effect of FHMD and gypsum on P control in a lab-scale simulation of a shallow lake. Strengths and unique advantages of this research are:

- Diatomite was creatively utilized in the development and application of FHMD. Diatomite provides dissolved Si for the formation of stabilized Si-containing ferrihydrite following a NaOH treatment of raw diatomite. Concurrently, porous diatomite acts as a carrier for ferrihydrite deposition. Furthermore, the mesopores and macropores of the diatomite provide the adsorbates with easy access to inner micropores, thereby increasing the rate of P adsorption onto FHMD.
- A new method to integrate a chemical P coprecipitation process with biological diatom P uptake was used for removal of P from lake water by FHMD. The high specific surface area and high P adsorption capacity of FHMD is capable of not only adsorbing a large amount of P from lake water but also stimulating diatom growth by

providing a supply of dissolved Si. Promoted diatom growth results in a larger scale spring diatom bloom and increased P consumption, thereby decreasing the strength of the subsequent summer cyanobacterial bloom. This can alter the algae community to a more suitable diatom-dominant vs. cyanobacteria-dominant.

- A new combination of FHMD and gypsum was used to limit P release from sediments under anoxic conditions and sediment resuspension in shallow lakes. FHMD was found capable of binding P in anoxic sediments, and gypsum was found effective in reducing sediment suspension. FHMD can be applied alone in deep lakes for P removal from the water column and to limit P release from anoxic sediments. However, in shallow lakes with associated wind-driven sediment resuspension, gypsum is required to stabilize the interface between the overlying water and the sediment.

The following conclusions can be drawn on the basis of the results of the research:

- Surface SiO_2 of diatomite is partially dissolved in the NaOH solution with stirring and heating. The dissolved Si contributes, through Si-O-Fe bonding, to the formation of stable 2-line Si-containing ferrihydrite that deposits into the larger macropores and mesopores of diatomite. The filling of the macropores and mesopores results in a significant increase in the specific surface area relative to unprocessed diatomite. Surface modification by 2-line ferrihydrite increases not only the specific surface area but also the surface charge.
- The higher crystallinity of ferrihydrite exerts a detrimental effect on the specific surface area of FHMD. The degree of crystallinity of ferrihydrite increases with increasing $FeCl_2$ amount, decreases with increasing NaOH amount, and increases greatly with higher calcination temperatures. Optimum formation parameters for the least crystalline ferrihydrite of FHMD are 0.5 M $FeCl_2$, 6 M NaOH solution, and a drying temperature of 50 °C.
- FHMD shows a high P adsorption capacity of 37.3 mgP/g at pH 4 as well as a significantly higher affinity for P compared with other anions. P is adsorbed onto

both shallow surface layer and deeper surface layer of FHMD. P is not precipitated with Fe(III) of ferrihydrite of FHMD.

- A dose of 400 mg/L of FHMD affords a P removal efficiency of 93% through P adsorption and stimulated diatom growth (by providing a supply of dissolved Si). Moreover, 400 mg/L of FHMD can effectively inactivate P in sediments and limit P release from anoxic sediments during a 30-day anoxic incubation period. The Fe-P pool in sediments treated with FHMD is significantly promoted and does not transform into Al-P because FHMD retains a strong P binding capacity under anoxic conditions.
- Gypsum can effectively reduce sediment resuspension; the optimum thickness of the gypsum layer was determined to be 0.8 cm. For lake water and sediment treated with FHMD and gypsum, no sediment P release seems to occur regardless of oxic or anoxic conditions.
- A lab-scale artificial aquarium was established to simulate temporary anoxic conditions and subsequent sediment resuspension in shallow lakes. After treatment with FHMD and gypsum combined, TP levels remained within the oligotrophic range. Regardless of high Si concentrations, diatom concentrations dropped during the 120-day incubation period due to the limiting level of P as well as diatom sedimentation. The combined application of FHMD and gypsum increased SO_4^{2-} concentrations and total alkalinity, but did not affect TKN concentrations. Labile P was much lower in the sediment of the treatment vs. control aquarium. However, Fe-P was markedly increased in the treatment aquarium sediment compared with the control.

6.2 Recommendations

A few recommendations for possible future studies are given as follows:

- Ecological effects on aquatic species must be considered in any program for eutrophication control. The ecological effects of the application of FHMD and gypsum in a real lake should be evaluated in a future study.

- Ferrihydrite-modified diatomite (FHMD) has been demonstrated to be an effective P adsorbent having a high P adsorption capacity. Although FHMD can be employed for P removal from the water column and P inactivation of sediments, FHMD can be also utilized for P removal from wastewater through P adsorption. Biological P removal, a common P removal method, is still limited; further improvement should aim to stabilize conditions as system performance is sensitive to biological conditions and wastewater composition. Adsorption after biological treatment has been also considered as an alternative to remove P effectively as adsorption processes operate simply, produce little sludge, and enable P recovery. Batch- and bench-scale P adsorption experiments using FHMD as a supplement for enhanced biological phosphate removal processes will be undertaken in a future study.
- FHMD is capable of binding P under anoxic conditions. This means that reduction of ferrihydrite in FHMD does not occur under anoxic conditions. The stability of the ferrihydrite in FHMD will be investigated in a future study.
- Dissolved organic P is a major portion of the total dissolved P in lake water. After the application of FHMD, the orthophosphate content of lake water is very low and orthophosphate-repressible alkaline phosphatase will be active in catalyzing the hydrolysis of dissolved organic P to support cyanobacterial growth. However, the high specific surface area and positive surface charge of FHMD can inhibit the alkaline phosphatase activity (APA) and prevent the supply of new orthophosphate via the transformation of dissolved organic phosphorus through APA. Thus, the effects of FHMD on the inhibition of APA will be investigated in a future study.
- The combined application of FHMD and gypsum can effectively remove P from lake water and limit P release from sediments. Sulfate (SO_4) ions provided by the addition of gypsum play an important role in ferric reduction under anoxic conditions; sulphide (S^{-1} and S^{2-}) ions produced by the sulphate reduction can reduce ferric ions, react with ferrous iron, and form a permanent sink for iron (FeS_2, FeS). The interactions between FHMD and gypsum will be investigated in a future study.
- A lab-scale artificial aquarium was established in the environmental chamber to simulate temporary anoxic conditions and subsequent sediment resuspension in shallow lakes. As complex physical, chemical, and hydraulic phenomena occur in

shallow lakes, field applications of the combination of FHMD and gypsum in either an enclosure or a entire lake to control eutrophication and cyanobacterial blooms are recommended.

- The artificial aquarium excluded all external nutrient sources. Phosphorus control by FHMD and gypsum in the presence of external nutrient sources should be investigated in a future study.
- When the trophic status of a lake changes from hypereutrophic or eutrophic to mesotrophic as a result of physical, chemical, or biological treatments, the addition of submerged aquatic vegetation (SAV) is a cost-effective way to improve the trophic level or maintain a mesotrophic level (Knight et al. 2003). The necessity for following FHMD and gypsum application with SAV or other control methods such as biomanipulation should be investigated in a future study.

References

Al-Degs, Y. S., Khraisheh, M. A. M., Tutunj, M. F. 2001. Sorption of lead ions on diatomite and manganese oxides modified diatomite. Water Res., **35**: 3724-3728.

American Public Health Association, American Water Works Association and Water Environmental Federation. 1992. Standard methods for the examination of water and wastewater. 18th ed., American Public Association, Washington, D.C.

Anderson, N. J., Jeppesen, E., Søndergaard, M. 2005. Ecological effects of reduced nutrient loading (oligotrophication) on lakes: an introduction. Freshwater Biol., **50**: 1589-1593.

Arias, C. A., Bubba Del, M., Brix, H. 2001. Phosphorus removal by sands for use as media in subsurface flow contructed reed beds. Water Res., **35**: 1159–1168.

Baker J., Olem H., Creager C., Marcus M., Parkhurst B. 1993. Fish and fisheries management in lakes and reservoirs. EPA 841-R-93-002. Terrene Institute and US Environmental Protection Agency, Washington, DC.

Banfield, J. F., Welch, S. A., Zhang, H., Ebert, T. T., Penn, R. L. 2000. Aggregation-based crystal growth and microstructure development in natural iron oxyhydroxide biomineralization products. Science, **289**: 751-754.

Barica, J. and Mur, L. R. 1980. Hypertrophic ecosystems. The Hague, W. Junk, Boston.

Bayrak, Y. 2006. Application of Langmuir isotherm to saturated fatty acid adsorption. Micropor. Mesopor. Mat., **87**: 203-206.

Beauchemin, S. D., Hesterberg, J., Chou, M., Beauchemin, R. R. S., Sayers, D. E. 2003. Speciation of phosphorus in P-enriched agricultural soils using XANES spectroscopy and chemical fractionation. J. Environ. Qual., **32**: 1809-1819.

Behrens, P. 1992. X-ray absorption spectroscopy in chemistry II. X-ray absorption near edge structure. Trends in analytical chemistry, **11**: 237-244.

Berg, U., Neumann, T., Donnert, D., Nüesch, R., Stüben, D. 2004. Sediment capping in eutrophic lakes- efficiency of undisturbed calcite barriers to immobilize phosphorus. Appl. Geochem., **19**: 1759-1771.

Bergmann, U., Glatzel, P., Cramer, S. P. 2002. Bulk-sensitive XAS characterization of light elements: from X-ray Raman Scattering to X-ray Raman Spectroscopy. Microchem. J., **71**: 221-230.

Bianconi, A. 1979. Core excitons and inner well resonances in surface soft x-ray absorption (SSXA) spectra. Surf. Sci., **89**: 41-50.

BjÖrkman, K. M. and Karl, D. M. 2003. Bioavailability of dissolved organic phosphorus in the euphotic zone at Station ALOHA, North Pacific Subtropical Gyre. Limnol. Oceanogr., **48**: 1049-1057.

Bostrom B., Persson G., Broberg B. 1988. Bioavailability of different phosphorus forms in freshwater systems. Hydrobiologia, **170**: 133-155.

Bowsher, C. G., Long, D. M., Oaks, A., Rothstein, S. J. 1991. Effect of light/dark cycles on expression of nitrate assimilatory genes in maize shoots and roots. Plant Physiol., **95**: 281-285.

Boyle, E. 1998. Pumping iron makes thinner diatoms. Nature, **393**: 733-734.

Braun, V. 1997. Avoidance of iron toxicity through regulation of bacterial iron transport. Biol. Chem., **378**: 779-786.

Campbell, A. S., Schwertmann, U., Stanjek, H., Friedl, J., Kyek, A., Campbell, P. A. 2002. Si incorporation into hematite by heating Si-ferrihydrite. Langmuir, **18**: 7804-7809.

Chaisena, A. and Rangsriwatananon, K. 2005. Synthesis of sodium zeolites from natural and modified diatomite. Mater. Lett., **59**: 1474-1479.

Chang, S. C. and Jackson, M. L. 1957. Fractionation of soil phosphorus. Soil Sci., **84**: 133-144.

Chang, W.Y.B. 1989. Estimates of hypolimnetic oxygen deficits in ponds. Aquaculture and Fishery Management, **20**: 167-172.

Chen, J., Yieconmi, S., Blaydes, T.G., 1996. Equilibrium and kinetic studies of copper adsorption by activated carbon. Separ. Technol. **6**: 133-146.

Chen, J. P. and Lin, M. 2001. Equilibrium and kinetics of metal adsorption onto a commercial H-type granular activated carbon: experimental and modeling studies. Water Res. **35**: 2385-2394.

Cooke G. 1980. Covering bottom sediments as a lake restoration technique. Water Res. Bull. **16**: 921-926.

Cooke G., Welch E., Peterson S., Newroth P. 1986. Lake and reservoir restoration. Butterworth Publisher, Stoneham, USA.

Cooke, G. D., Welch, E. B., Peterson, S. A., Nichols, S. A. 2005. Restoration and management of lakes and reservoirs (3rd edition). Taylor & Francis., New York.

Corbridge, D. E. C. 1985. Phosphorus, an outline of its chemistry, biochemistry and technology (3rd edition). Elsevier, New York.

Cramer, S. P., Wang, H., Bryant, C., Legros, M., Horne, C., Patel, D., Ralston, C., Wang, X. 1998. Soft X-ray absorption spectroscopy: Application to Bioinorganic Chemistry. In the Spectroscopic Methods in Bioinorganic Chemistry; Solomon, E. I.; Hodgson, K. O., American Chemical Society: Washington,

Crini, G. and Peindy, H. N. 2006. Adsorption of C. I. basic blue 9 on cyclodextrin-based material containing carboxylic groups. Dyes and Pigm., **70**: 204-211.

Crosby, S. E., Butler, E. I., Turner, D. R.,Whitfield, M.,Glasson, D. R., Millward, G. E. 1981. Phosphate adsorption onto iron hydroxides at natural concentrations. Environ. Technol. Lett., **2**: 371-378.

deGroot, F. M. F. 1993. X-ray absorption of transition metal oxides: an overview of the theoretical approaches. J. Electron Spectrosc. Relat. Phenom., **62**: 111-130.

Deppe T. and Benndorf J. 2002. Phosphorus reduction in a shallow hypereutrophic reservoir by in-lake dosage of ferrous iron. Water Res., **36**: 4525-4534.

Dittrich M., Dittrich T., Sieber I., Koschel R. 1997. A balance analysis of phosphorus elimination by artificial calcite precipitation in a stratified hardwater lake. Water Res., **31**: 237-248.

Drever, J. I. 1988. The geochemistry of natural waters. Prentice Hall, Eaglewood Cliffs, New Jersy.

Drizo, A., Frost, C.A., Grace, J., Smith, J.K. 1999. Physico-chemical screening of phosphate-removing substrates for use in constructed wetland systems. Water Res., **33**: 3595-3602.

Dunst R., Born S., Uttormark P., Smith S., Nichols S., Peterson J., Knauer D., Serns S., Winter, D., Wirth, T. 1974. Survey of lake rehabilitation technique and experiences. Tech. Bull., 75. Department of natural resources, Madison, Wisconsin.

Evans, M.S. 2005. Sedimentation rates and carbon, nitrogen and phosphorus fluxes in Jackfish and Murray Lakes. National Water Research Institute, Saskatoon, Canada.

Ford, R. G., Wilkin, R. T., Hernandez, G. 2006. Arsenic cycling within the water column of a small lake receiving contaminated ground-water discharge. Chem. Geol., **228**: 137-155.

Forti, P. 1997. Speleothems in gypsum caves. Int. J. Speleol. **25**: 91–104.

Franke, R. and Hormes, J. 1995. The P K-near edge absorption spectra of phosphates. Physica B, **216**: 85-95.

Gächter R. and Wehrli B. 1998. Ten years of artificial mixing and oxygenation: No effect on the internal phosphorus loading of two eutrophic lakes. Environ. Sci. Technol., **32**: 3659-3665.

Gächter, R. and Müller, B. 2003. Why the phosphorus retention of lakes does not necessarily depend on the oxygen supply to their sediment surface. Limnol. Oceanogr., **48**: 929-933.

Garvie, L. A. J. and Buseck, P. R. 1998. Ratios of ferrous to ferric iron from nanometer-sized areas in minerals. Nature, **396**: 667-670.

Gautier, J., Grosbois, C., Courtin-Normade, A., Floc'H, J. P., Martin, F. 2006. Transformation of natural As-associated ferrihydrite downstream of a remediated mining site. Eur. J. Miner., **18**: 187-195.

Glasauer, S. M., Hug, P., Weidler, P. G., Gehring, A. U. 2000. Inhibition of sintering by Si during the conversion of Si-rich ferrihydrite to hematatite. Clays. Clay. Miner., **48**: 51-56.

Göll, I. G., Schulze, Z. H.,Ludwig, R. G. 1989. Possibilities for dry preparation of low-grade diatomite raw materials. Miner. Proc., **30**: 144-151.

Goren R., Baykara T., Marsoglu M. 2002. Effects of purification and heat treatment on pore structure and composition of diatomite. British Ceramic Transactions, **101**: 177-180.

Griffith, E. J., Beeton A., Spencer, J. M., Mitchell, D. T. 1973. Environmental phosphorus handbook. Jon Wiley & Sons, New York.

Håkanson, L., and Jansson, M. 1983. Principles of lake sedimentology. Springer-Verlag, New York.

Hansen J., Reitzel K., Jensen, H. S., Andersen, F. Ø. 2003. Effects of aluminium, iron, oxygen and nitrate additions on phosphorus release from the sediment of a Danish softwater lake. Hydrobiologia, **492**:139-149.

Harp, G. R., Han, Z. L., Tonner, B. P. 1989. X-ray absorption near edge structures of intermediate oxidation states of silicon in silicon oxides during thermal desorption. J. Vac. Sci. Technol. A, **8**: 2566-2569.

Harper, D. 1992. Eutrophication of freshwaters, principles, problems and restoration. Chapman & Hall.

Hart, B. T., Roberts, S., James, R., O'Donohue, M., Taylor, J., Donnert, D., Furrer, R. 2003. Active barrier to reduce phosphorus release from sediments: effectiveness of three forms of $CaCO_3$. Aust. J. Chem., **56**: 207-217.

Hartley, A. M., House, W. A., Callow, M. E., Leadbeater, B. S. C. 1997. Coprecipitation of phosphate with calcite in the presence of photosynthesizing green algae. Water Res., **31**: 2261-2268.

Harwood, D. M. 1999. Diatomite. In the Diatoms, Applications for the Environmental and Earth Science. Stoermer, E. F., Smol, J. P., Ed., Cambridge University Press, Cambridge,

HDR Engineering Inc. 2001. Handbook of public water systems (2^{nd} edition). John Wiley & Sons, Inc., New York.

Herrera, F., Lopez, A., Mascolo, G., Albers, P., Kiwi, J. 2001. Catalytic combustion of Orange II on hematite surface species responsible for the dye degradation. Appl. Catal., B, **29**: 147-162.

Hesterberg, D., Zhou, W., Hutchison, K. J., Beauchemin, S., Sayers, D. E. 1999. XAFS study of adsorbed and mineral forms of phosphate. J. Synchrotron Rad., **6**: 636-638.

Hieltjes, A. H. M. and Lijklema, L. 1980. Fractionation of inorganic phosphates in calcareous sediments. J. Envir. Qual., **9**: 405-407.

Higgins, B. P. J., Mohleji, S. C., Irvine, B. L. 1976. Lake treatment with fly ash, lime, and gypsum. J. Water Pollut. Control, **48**: 2153-2164.

Horne, A. J. and Goldman, C. R. 1994. Limnology (2nd edition). McGraw-Hill Inc., New York.

Hsieh, C.-T. and Teng, H. 2000. Langmuir and Dubinin-Radushkevich analysis on equilibrium adsorption of activated carbon fabrics in aqueous solutions. J. Chem. Technol. Biotechnol., **75**: 1066-1072.

Hu, Y. F., Boukherroub, R., Sham, T. K. 2004. Near edge X-ray absorption fine structure spectroscopy of chemically modified porous silicon. J. Electron. Spectrosc., **135**: 143-147.

Hu Y. F., Zuin L., Wright G., Igarashi R., McKibben M., Wilson T., Chen S., Johnson T., Maxwell D., Sham T. K., Reininger R. 2007 Commissioning and performance of the VLS-PGM beamline at the Canadian Light Source. Rev Sci Instrum **78 083109**: 1-5.

Huang, W., Wang, S., Zhu, Z., Li, L., Yao, X., Rudolph, V., Haghseresht, F. 2008. Phosphate removal from wastewater using red mud. J. Hazard. Mater., **158**: 35-42.

Hullebusch, E. V., Deluchat V., Chazal, P. M., Bandu M. 2002. Environmental impact of two successive chemical treatments in a small shallow eutrophied lake: Part I. Case of aluminium sulphate. Environ. Pollut., **120**: 617-626.

Janney, D. E., Cowley, J. M., Buseck, P. R. 2000. Transmission electron microscopy of synthetic 2- and 6- line ferrihydrite. Clay. Clay. Miner., **48**: 111-119.

Jensen, H. S. and Thamdrup, B. 1993. Iron-bound phosphorus in marine sediments as measured by bicarbonate-dithionite extraction. Hydrobiologia, **253**: 47-59.

Jeunesse, I. La., Deslous-Paoli, J. M., Ximénés, M. C., Cheylan, J. P., Mende, C., Borrero, C., Scheyer, L. 2002. Changes in point and non-point sources phosphorus loads in the Thau catchment over 25 years (Mediterranean Sea – France). Hydrobiologia, **475/476**: 403-411.

Kagalou, I., Papastergiadou, E., Tsimarakis, G., Petridis, O. 2003. Evaluation of the trophic state of Lake Pamvotis Greece, a shallow urban lake. Hydrobiologia, **506-509**: 745-752.

Kalff, J. 2002. Limnology inland water ecosystems. Prentice Hall, New Jersey.

Karim, Z. 1984. Characteristics of ferrihydrite formed by oxidation of $FeCl_2$ solutions containing different amounts of silica. Clays Clay Miner. **32**: 181-184.

Kasrai, M., Yin, Z., Bancroft, G. M., Tan, K. H. 1993. X-ray fluorescence measurements of x-ray absorption near edge structure at the Si, P, and S L edges. J. Vac. Sci. Technol. A, **11**: 2694-2699.

Kawai, J., Mizutani, Y., Sugimura, T., Sai, M., Hignchi, T., Harada, Y., Ishiwata, Y., Fukushima, A., Fujisawa, M., Watanabe, M., Maeda, K., Shiu, S., Gohshi, Y. 2000. High resolution soft x-ray absorption spectroscopy for the chemical state analysis of Mn. Spectrochim. Acta. B, **55**: 1385-1395.

Kendelewicz, T., Liu, P., Doyle, C. S., Brown Jr, G. E. 2000. Spectroscopic study of the reaction of aqueous Cr(VI) with Fe_3O_4 (111) surfaces. Surf. Sci., **469**: 144-163.

Khare, N. Hesterberg, D., Beauchemin, S., Wang, S.-L. 2004. XANES determination of adsorbed phosphate distribution between ferrihydrite and boechmite in mixtures. Soil Sci. Soc. Am., **68**: 460-469.

Khoshmanesh, A., Hart, B. T., Duncen, A., Beckett, R. 2002. Luxury uptake of phosphorus by sediment bacteria. Water Res., **36**: 774-778.

Khraisheh, M. A. M., Al-degs, Y. S., Mcminn, W. A. M. 2004. Remediation of wastewatercontaining heavy metals using raw and modified diatomite. Chem. Eng. J., **99**: 177-184.

Khraisheh, M. A. M., Al-Ghouti, M. A., Allen, S. J., Ahmad, M. N. 2005. Effect of OH and silanol groups in the removal of dyes from aqueous solution using diatomite. Water Res. **39**: 922-932.

Kirpichtchikova, T., Manceau, A., Spadini, L., Panfili, F., Marcus, M. A., Jacquet, T. 2006. Speciation and solubility of heavy metals in contaminated soil using X-ray microfluorescence, EXAFS spectroscopy, chemical extraction, and thermal dynamic modeling. Geochim. Cosmochim. Ac., **70**: 2163-2190.

Klapper H. 2003. Technologies for lake restoration. J. Limnol., **62**: 73-90.

Knight, R. L., Gu, B., Clarke, R. A., Newman, J. M. 2003. Long-term phosphorus removal in Florida aquatic systems dominated by submerged aquatic vegetation. Ecol. Eng., **20**: 45-63.

Kogel, J. E., Trivedi, N. C., Barker, J. M., Krukowski, S. T. 2006. Industrial minerals & rocks: commodities, markets, and uses (7^{th} edition). SME, Littleton.

Koningsberger, D. C. and Prins, R. 1998. X-ray absorption. Principles, applications, techniques of EXAFS, SEXAFS and XANES. John Wiley & Sons, New York.

Konopka, A., Brock, T. D. 1978. Effect of temperature on blue-green algae (cyanobacteria) in Lake Mendota. Appl. Environ. Microbiol., 36, 572-576.

Koski-Vähälä, J., Hartikainen, H., Tallberg, P. 2001. Phosphorus mobilization from various sediment pools in response to increased pH and silicate concentration. J. Environ. Qual., **30**: 546-552.

Krivstov, V., Bellinger, E., Sigee, D., Corliss, J. 2000. Interrelations between Si and P biogeochemical cycles – a new approach to the solution of eutrophication problem. Hydrol. Process, **14**: 283-295.

Kuiper, P., Searle, B. G., Rudolf, P., Tjeng, L. H., Chen, C. T. 1993. X-ray magnetic dichroism of antiferromagnet Fe_2O_3: The orientation of magnetic moments observed by Fe 2*p* X-ray absorption spectroscopy. Phys. Rev. Lett., **70**: 1549-1552.

Kukkadapu, R. K., Zachara, J. M., Fredrickson, J. K., Smith, S. C., Dohnalkova, A. C., Russell, C. K. 2003. Transformation of 2-line ferrihydrite to 6-line ferrihydrite under oxic and anoxic conditions. Am. Mineral., **88**: 1903-1914.

Kumar, S., Alimuddin, K. K., Kumor, R., Thakur, P., Chae, K. H., Augadi, B., Choi W. K. 2007. Electron transport, magnetic and electronic structure studies of $Mg_{0.95}Mn_{0.05}Fe_{2-2x}Ti_{2x}O_{4\pm\delta}$ ($0 \leq x \leq 0.5$) ferrites. J Phys: Condens Matter., **19**: 476210-476224.

Laenen, A. and LeTourneau, A. P. 1996. Estimate of wind-induce resuspension of bed sediment during periods of low lake elevation. Upper Klamath Basin nutrient loading study. U. S. geological Survey., Portland, Oregon.

Lewandowski, J., Schauser, I., Hupfer, M. 2003. Long term effects of phosphorus precipitations with alum in hypereutrophic Lake Süsser See (Germany). Water Res., **37**: 3194-3204.

Li, D., Fleet, M. E., Bancroft, G. M., Kasrai, M., Pan, Y. 1995. Local structure of Si and P in SiO_2-P_2O_5 and Na_2O-SiO_2-P_2O_5 glasses: a XANES study., J. Non-Cryst. Solids., **188**: 181-189.

Li, Y.-R., Pereira, G., Lachenwitzer, A., Kasrai, M., Norton, P. R. 2007. X-Ray Absorption Spectroscopy and Morphology Study on Antiwear Films Derived from ZDDP Under Different Sliding Frequencies. Tribol. Lett. **27**: 245–253.

Loan, M., Pierre, T. G. St., Parkinson, G. M., Newman, O. G. M., Farrow, J. B. 2002. Identifying nanoscale ferrihydrite in hydrometallurgical residues. JOM., **December**, 40-43.

Lowell, S., Shields, E. J., Thomas, M. A., Thommes, M. 2004. Characterization of porous solids and powders: surface area, pore size and density., Kluwer Academic Publishers, Boston.

Lynch, J. 2003. Physical-chemical analysis of industrial catalysts: a practical guide to characterisation. Editions Technip, Paris.

Margeritondo, G. 1988. Introduction to synchrotron radiation. Oxford University Press, New York.

Matsunaga, K., Nishioka, J., Kuma, K., Toya, K., Suzuki, Y. 1998. Riverine input of bioavailable iron supporting phytoplankton growth in Kesennuma Bay (Japan). Water Res., **32**: 3436-3442.

Mayer, T. D. and Jarrell, W. M. 1996. Formation and stability of iron (II) oxidation products under natural concentrations of dissolved silica. Water Res., **30**: 1208-1214.

Mayer, T. D. and Jarrell, W. M. 2000. Phosphorus sorption during iron (II) oxidation in the presence of dissolved silica. Water Res., **34**: 3949-3956.

Matijevic, E. and Borkovec M. 2004. Surface and colloid surface. Springer, Boston.

Meadows, A., Meadows., P. S., West, F. J. C., Murray, J. M. H. 2000. bioturbation, geochemistry and geotechnics of sediments affected by the oxygen minimum zone on the Oman continental slope and abyssal plain, Arabian Sea. Deep-Sea Res. Part II, **47**: 259-280.

Mezenner, N. Y., Bensmaili, A. 2008. Kinetic and thermodynamic study of phosphate adsorption on iron hydroxide-eggshell waste. Chem. Eng. J., **in press**.

Mo S. D., Ching, W. Y. 2001. X-ray Absorption Near-edge Structure in alpha-quartz and Stishoite: ab *initio* Calculation with Core-hole Interaction. Appl. Phys. Lett., **78**: 3809-3811.

Mondal, K. and Lalvani, S. B. 2000. Modelling of mass transfer controlled adsorption rate based on the Langmuir adsorption isotherm. Sep. Sci. Technol., **35**: 2583-2599.

Nürnberg, G. K. 1984. The prediction of internal phosphorus load in lakes with anoxic hypolimnia. Limnol. Oceanogr., **29**: 111-124.

Oh, Y.-M., Hesterberg, D.L., Nelson, P.V. 1999. Comparison of phosphate adsorption on clay minerals for soilless root media. Commun. Soil Sci. Plant Anal., **30**: 747-756.

O'Reilly, S. E., Strawn, D. G., Sparks, D. L. 2001. Residence Time Effects on Arsenate Adsorption/Desorption Mechanisms on Goethite. Soil Sci. Soc. Am. J., **65**: 67–77.

Pan, Y., Brown, A., Brydson, R. 2006. Electron beam damage studies on 6-line ferrihydrite. J. Phys.: Conference Series, **26**: 46-49.

Parfitt, R. L., Van der Gaast, S. J., Childs, C. W. 1992. A structural model for natural siliceous ferrihydrite. Clays Clay Miner., **40**: 675–681.

Peters, N. E. and Meybeck, M. 2000. Water quality degradation effects on freshwater availability: impacts of human activities. Water Int., **25**: 185-193.

Petterson, K., Bostrom, B., Jacobsen, O. - S. 1988. Phosphorus in sediments – speciation and analysis. Hydrobiologia, **170**: 91-101.

Politi, Y., Metzler, R. A., Abrecht, M., Gilbert, B., Wilt, F. H., Sagi, I., Addadi, L., Weiner, S., Gilbert, P. U. P. A. 2008. Transformation mechanism of amorphous calcium carbonate into calcite in the sea urchin larval spicule. PNAS, **105**: 17362-17366.

Psenner, R., Boström, B., Dinka, M., Petterson, K., Pucsko, R., Sager, M. 1988. Fractionation of phosphorus in suspended matter and sediment. Arch. Hydrobiol. Beih. **30**: 98-110.

Qin, B., Hu, W., Chen, W. 2004. Process and mechanism of environmental changes in Taihu Lake. Science Publisher., Beijing, China.

Reale, P. and Scrosati, B. 2003. Synthesis and thermal behavior of crystalline hydrated iron (III) phosphate of interest as positive electrodes in Li batteries. Chem. Mater., **15**: 5051-5058.

Regier T., Krochak J., Sham T. K., Hu Y. F., Blyth R. I. R. 2007 Performance and capabilities of the Canadian Dragon: The SGM beamline at the Canadian Light Source. Nucl Instrum Methods Phys Res Sect A, **582**: 93-95.

Rhoton, F. E. and Bigham, J. M. 2005. Phosphate adsorption by ferrihydrite-amended soils. Environ. Qual., **34**: 890-896.

Round, F. E., Crawford, R. M., Mann, D. G. 1990. The Diatoms. Cambridge University Press: Cambridge.

Ruane, R. J. and Mobley, M. H. 2002. Water quality design requirements for a line diffuser oxygen injection systems at J. Percy Priest Reservoir. CE workshop on hydrogen sulfide, Nashville.

Ruban V. and Demare D. 1998. Sediment phosphorus and internal phosphorus flux in the hydroelectric reservoir of Bort-Ies-Orgues, France. Hydrobiologia., **373/3374**: 349-359.

Ruloy, J. E. and Rusch, K. A. 2004. Development of a simplified phosphorus management model for a shallow, subtropical, urban hypereutrophic lake. Ecol. Eng., **22**: 77-98.

Rydin E. 2000. Potentially mobile phosphorus in lake Erken sediment. Water Res., **34**: 2037-2042.

Rydin E. and Welch E. B. 1998. Aluminum dose required to inactivate phosphate in lake sediments. Water Res., **32**: 2969-2976.

Ryding, S.-O., Rast W. (Editors). 1989. The control of eutrophication of lakes and reservoirs. The Parthenon Publishing Group, Paris.

Sakadevan, K. and Bavor, H. J. 1998. Phosphate adsorption characteristics of soils, slags and zeolite to be used as substrates in constructed wetland systems. Water Res., **32**: 393-396.

Salonen, V.-P. and Varjo, E. 2000. Gypsum treatment as a restoration method for sediments of eutrophic lakes−experiments from southern Finland. Environ. Geol., **39**: 353-359.

Scarlatos, P. D. 1997. Experiments on water-sediment nutrient partitioning under turbulent, shear and diffusive conditions. Water, Air Soil Pollut., **99**: 411-425.

Schwertmann, U., Friedl, J., Stanjek, H. 1999. From Fe(III) Ions to Ferrihydrite and then to Hematite. J. Colloid Interface Sci., **209**: 215–223.

Schwertmann, U. and Cornell, R. M. 2000. Iron Oxides in the Laboratory: Preparation and Characterization. Wiley-VCH, New York.

Seehra, M. S., Roy, P., Raman, A., Manivannan, A. 2004. Structural investigation of synthetic ferrihydrite nanoparticles doped with Si. Solid State Commun., **130**: 597-601.

Sharma, H. D. and Reddy, K. R. 2004. Geoenvironmental engineering: site remediation, waste containment, and emerging waste management technologies. Hoboken Inc., New Jersey.

Sherwood, L. J. and Qualls, R. G. 2001. Stability of P within a wetland soil following ferric chloride treatment to control eutrophication. Environ. Sci. Technol., **35**: 4126-4131

Shin, E. W., Han, J. S., Jang, M., Min, S.-H., Park, J. K., Rowell, R. M. 2004. Phosphate adsorption on aluminum-impregnated mesoporous silicates: surface structure and behaviour of adsorbents. Environ. Sci. Technol., **38**: 912-917.

Smith, V. H. 1979. Nutrient dependence of primary productivity in lakes. Limnol. Oceanogr., **24**: 1051-1064.

Smith, V. H., Tilman, G. D., Nekola, J. C. 1999. Eutrophication: impacts of excess nutrient input on freshwater, marine, and terrestrial ecosystem. Environ. Pollut., **100**: 179- 196

Soldatov, A. V., Kasrai, M., Bancroft, G. M. 2000. Unoccupied Electronic States of Stishovite: X-ray Absorption Fine Structure Theoretical Analysis. Solid State Commun., **115**: 687-692.

Sparks, D. L. 2003. Environmental soil chemistry. Academic Press: San Diego, CA.

Steinman, A., Rediske, R., Reddy, K. R. 2004. The reduction of internal phosphorus loading using alum in Spring Lake, Michigan. J. Environ. Qual., **30**: 2040-2048.

Stoylar, S. V., Bayukov, O. A., Gurevich, Y. L., Ladygina, V. P., Iskhakov, R. S., Pustoshilov, P. P. 2007. Mössbauer Study of Bacterial Ferrihydrite. Inorg. Mater. **43**: 638-641.

Sutton, A. P. 1993. Electronic structure of materials. Clarendon Press, Oxford.

Takeda, S. 1998. Influence of iron availability on nutrient consumption ratio of diatoms in oceanic waters. Nature, **393**: 774-777.

Tchobanoglous, G., Burton, F. L., Stensel, H. D. 2003. Wastewater engineering treatment and reuse (4^{th} edition). McGraw-Hill, New York.

Thomann, R. V. and Mueller, J. A. 1987. Principles of Surface Water Quality Modelling and Control. Harper Collins Publishers Inc., New York.

Tsai H. M., Ray, S. C., Pao, C. W., Chiou, J. W., Huang, C. L., Du, C. H., Pong, W. F., Tsai, M. H., Fukano, A., Oyanagi, H. 2008. Enhancement of Si-O Hybridization in Low-temperature Grown Ultraviolet Photo-oxidized SiO_2 Film Observed by X-ray Absorption and Photoemission Spectroscopy. J. Appl. Phys., **103**: 013704.

Tuhela, L., Carlson, L., Tuovinen, O. H. 1992. Ferrihydrite in water cells and bacterial enrichment cultures. Water Res., **26**: 1159-1162.

Van Der Molen, D. T., Portielje, R., Boers, P. C. M., Lijklema, L. 1998. Changes in sediment phosphorus as a result of eutrophication and oligotrophication in Lake Veluwe, the Netherlands. Water Res., **32**: 3281-3285.

Varlot, K., Kasrai, M., Bancroft, G. M., Yamaguchi, E. S., Ryason, P.R., Igarashi, J. 2001. X-ray absorption study of antiwear films generated from ZDDP and borate micelles. Wear, **249**: 1029-1035.

Vempati, R. K. and Loeppert, R. H. 1989. Influence of structural and adsorbed Si on the transformation of synthetic ferrihydrite. Clays Clay Miner., **37**: 273-279.

Wachtman, J. B. 1993. Characterization of materials. Butterworth-Heinemann, Boston.

Wadpersdolf, E., Neumann, T., Stuben, D. 2004. Efficiency of natural calcite precipitation compared to lake marl application used for water quality improvement in an eutrophic lake. Appl. Geochem., **19**: 1687-1698.

Wang, H., Appan, A., Gulliver, J. S. 2003. Modelling of phosphorus dynamics in aquatic sediments: I−model development. Water Res., **37**: 3928-3938.

Weidler, P. G. 1997. BET sample pretreatment of synthetic ferrihydrite and its influence on the determination of surface area and porosity. J. Porous Mater., **4**: 165-169.

Welch, E. B. and Patmont, C. R. 1980. Lake restoration by dilution; Mose Lake, Washington. Water Res., **14**: 1317-1325.

Welch, E. B., Michand, t. P., Perkins, M. A. 1982. Alum control of internal phosphorus loading in a shallow lake. Water Resour. Bullet., **18**: 929-936.

Wetzel, R. G. 2001. Limnology lake and reservoir ecosystems (3^{rd} edition). Academic Press, London.

Wilks, R. g., MacNaughton, J. B., Kraatz, H. – B., Regier, T., Moewes, A. 2006. Combined X-ray absorption spectroscopy and density functional theory examination of ferrocene-labelled reptides. J. Phys. Chem.. B, **110**: 5955-5965.

Wu, Z. Y., Jollet F., Seifert F. 1998. Electronic Structure Analysis of alpha-SiO_2 via X-ray Absorption Near-edge Structure at the Si K, $L_{2,3}$ and O K-edges. J. Phys. Condens. Matter., **10**: 8083-8092.

Wu, D., Zhang, B., Li, C., Zhang, Z., Kong, H. 2006. Simultaneous removal of ammonium and phosphate by Zeolite synthesized from fly ash as influenced by salt treatment. J. Colloid Interface Sci., **304**: 300-306.

Xiong, J., He, Z., Mahmood, Q., Liu, D., Yang, X., Islam. 2008. Phosphate removal from solution using steel slag through magnetic separation. J. Hazard. Mater., **152**: 211-215.

Xiong, W., Peng, J. 2008a. Phosphorus removal from lake water by combined dosage of ferrous iron and diatomite. ASCE World Environmental & Water Resources Congress, Honolulu, Hawaii, USA, May 12-16.

Xiong, W. and Peng, J. 2008b. Development and characterization of ferrihydrite-modified diatomite as a new phosphorus adsorbent. Water Res., **42**: 4869-4877.

Xiong, W., Peng, J., Hu, Y. 2009. Chemical analysis for optimal synthesis of ferrihydrite-modified diatomite using soft X-ray absorption near-edge structure spectroscopy. Phys. Chem. Minerals, **DOI 10**.1007/s00269-009-0301-7.

Yin, Z., Kasrai, M., Bancroft, G. M. 1995. X-ray-absorption spectroscopic studies of sodium polyphosphate glasses. Phys. Rev. B, **51**: 742-750.

Zhang Y. and Prepas, E. E. 1996. Short-term effects of $Ca(OH)_2$ additions on phytoplankton biomass: a comparison of laboratory and *in situ* experiments. Water Res., **30**: 1285-1294.

Zhao, J., Huggins, F. E., Feng, Z., Huffman, G. P. 1994. Ferrihydrite: surface structure and its effects on phase transformation. Clays. Clay. Miner., **42**: 737-746.

Zhou, Y., Song, C., Cao, X., Li, J., Chen, G., Xia, Z., Jiang, P. 2008. Phosphorus fractions and alkaline phosphatise activity in sediments of a large eutrophic Chinese lake (Lake Taihu). Hydrobiologia, **599**: 119-125.

APPENDIX A: EXPERIMENTAL RESULTS

Table A.1 Surface charge density of FHMD changes with pH values

Volume, mL	pH_1	pH_2	pH_{avg}	Surface charge, C/m^2
0	3.26	3.34	3.30	0.59
1	3.40	3.56	3.48	0.55
2	3.59	3.76	3.68	0.52
3.5	3.95	4.16	4.06	0.46
4.5	4.33	4.57	4.45	0.42
5.5	4.80	5.09	4.95	0.38
6.5	5.35	5.65	5.50	0.34
7.5	5.92	6.21	6.07	0.30
8.5	6.49	6.75	6.62	0.26
9.5	6.97	7.29	7.13	0.22
10	7.16	7.51	7.34	0.20
11	7.78	8.11	7.95	0.16
12	8.14	8.42	8.28	0.13
13	8.82	8.90	8.86	0.09
14	9.37	9.46	9.42	0.054
15	9.84	9.88	9.86	0.021
16	10.13	10.13	10.13	-0.011
17	10.41	10.37	10.39	-0.041
18	10.61	10.59	10.60	-0.067
19	10.78	10.76	10.77	-0.092
20	10.93	10.90	10.92	-0.11
21	11.03	11.02	11.03	-0.14
22	11.14	11.13	11.14	-0.15
23.1	11.23	11.22	11.23	-0.17
24	11.29	11.29	11.29	-0.19
25	11.35	11.35	11.35	-0.21
26	11.41	11.41	11.41	-0.22
27	11.46	11.46	11.46	-0.24
28	11.50	11.51	11.51	-0.25
29	11.55	11.56	11.56	-0.26
30	11.59	11.60	11.60	-0.28
31	11.62	11.63	11.63	-0.29
32	11.65	11.67	11.66	-0.30
33	11.68	11.70	11.69	-0.31
34	11.71	11.72	11.72	-0.33
35	11.74	11.75	11.75	-0.34
36	11.76	11.77	11.77	-0.35
37	11.78	11.79	11.79	-0.37
38	11.80	11.82	11.81	-0.37
39.1	11.82	11.84	11.83	-0.39
40	11.84	11.86	11.85	-0.40
41	11.86	11.88	11.87	-0.41
42	11.88	11.89	11.89	-0.42

43	11.89	11.91	11.90	-0.43
44	11.91	11.92	11.92	-0.44
45	11.93	11.94	11.94	-0.45
46	11.94	11.95	11.95	-0.46
47	11.95	11.97	11.96	-0.47
48	11.97	11.98	11.98	-0.48
49	11.98	11.99	11.99	-0.49
50	11.99	12.00	12.00	-0.50

Table A.2 Surface charge density of raw diatomite changes with pH values

Volume, mL	pH_1	pH_2	pH_{avg}	Surface charge, C/m^2
0	2.72	2.70	2.71	0.048
1	2.94	2.90	2.92	0.037
2.1	3.38	3.46	3.42	0.026
3	4.81	6.17	5.49	0.0042
4	9.65	9.99	9.82	-0.035
4.5	9.99	10.31	10.15	-0.053
5	10.32	10.53	10.43	-0.068
5.5	10.55	10.72	10.64	-0.081
6	10.71	10.84	10.78	-0.094
6.5	10.84	10.97	10.91	-0.11
7	10.95	11.06	11.01	-0.12
7.5	11.03	11.13	11.08	-0.13
8	11.12	11.21	11.17	-0.13
8.5	11.21	11.28	11.25	-0.14
9	11.27	11.34	11.31	-0.15
9.5	11.33	11.40	11.37	-0.15
10	11.38	11.45	11.42	-0.16
10.5	11.44	11.49	11.47	-0.16
11	11.46	11.53	11.50	-0.17
11.5	11.50	11.56	11.53	-0.18
12	11.54	11.59	11.57	-0.19
12.5	11.57	11.62	11.60	-0.19
13	11.61	11.65	11.63	-0.19
13.5	11.63	11.68	11.66	-0.20
14	11.66	11.70	11.68	-0.21
14.5	11.69	11.72	11.71	-0.21
15	11.71	11.75	11.73	-0.22
15.5	11.74	11.76	11.75	-0.22
16	11.75	11.78	11.77	-0.23
16.5	11.78	11.80	11.79	-0.23
17	11.79	11.82	11.81	-0.24
17.5	11.81	11.84	11.83	-0.24
18	11.83	11.85	11.84	-0.25
18.5	11.85	11.87	11.86	-0.25
19	11.86	11.88	11.87	-0.26
20	11.89	11.91	11.90	-0.26
21	11.92	11.94	11.93	-0.27
22	11.94	11.95	11.95	-0.29
23	11.97	11.97	11.97	-0.29
24	11.99	12.00	12.00	-0.30

Table A.3 Phosphorus adsorption data of raw diatomite obtained at different pH values: pH4 and pH8.5

pH=4	C_0, mg/L	C_e, mg/L	M, g	Q_e, mgP/g
	3	1	0.0516	3.88
	6	3	0.0512	5.86
	10	6	0.0503	7.95
	15	10	0.0517	9.67
	20	15	0.0520	9.62
	25	20	0.0515	9.71
	30	25	0.0506	9.88
	35	30	0.0501	9.98
	40	35	0.0527	9.49
pH=8.5	C_0, mg/L	C_e, mg/L	M, g	Q_e, mgP/g
	3	2.48	0.0528	0.98
	6	5.44	0.0526	1.06
	10	9.29	0.051	1.39
	15	14.28	0.0509	1.41
	20	19.24	0.0506	1.50
	25	24.22	0.0513	1.52
	30	29.22	0.0509	1.53
	35	34.22	0.0504	1.55
	40	39.14	0.0536	1.60

Table A.4 Phosphorus adsorption data of FHMD obtained at different pH values: pH4 and pH8.5

pH=4	C_0, mg/L	C_e, mg/L	M, g	Q_e, mgP/g
	3	0.5	0.0515	4.85
	6	1	0.0502	9.96
	10	2	0.0520	15.38
	15	3.5	0.0504	22.82
	20	7	0.0516	25.19
	25	10.5	0.0509	28.49
	30	14	0.0518	30.89
	35	18	0.0508	33.46
	40	23	0.0523	32.50
pH=8.5	C_0, mg/L	C_e, mg/L	M, g	Q_e, mgP/g
	3	1.98	0.0513	1.99
	6	4.14	0.0514	3.62
	10	7.31	0.0507	5.31
	15	11.53	0.0525	6.61
	20	16.08	0.0514	7.63
	25	20.46	0.0519	8.75
	30	25.22	0.051	9.37
	35	29.89	0.0519	9.85
	40	34.69	0.0522	10.17

Table A.5 Adsorption of anions onto FHMD

Adsorbate	C_0, mg/L	Ce_1, mg/L	Ce_2, mg/L	Ce_3, mg/L	Ce_{avg}, mg/L	m, g	Q, mgP/g
PO_4s	31.02	26	26.5	26	26.17	0.1013	9.47
PO_4c	31.07	26.5	26.5	27	26.67	0.1027	8.45
SO_4	96	98	92	-	95	0.1027	1.95
NO_3	14	14	13.5	13	13.5	0.1027	0.97
CO_3	60	59.95	59.95	-	59.95	0.1027	0.10
Cl	35.5	36.7	35.5	36	36.07	0.1027	0

Table A.7 Phosphorus removal from lake water by FHMD

Dose, mg/L	TP, μg/L	RE, %	Si, mg/L	Fe, mg/L	Diatom, cells/ml
0	143.3	0	1.44	0.16	218750
50	69.4	51.59	3.13	0.20	581250
100	51.6	63.88	3.56	0.22	1243750
150	37.0	74.18	4.17	0.19	1743750
200	27.6	80.76	3.75	0.22	906250
250	17.0	88.12	4.93	0.19	2031250
300	13.8	90.35	4.80	0.26	2018750
350	12.3	91.41	4.73	0.27	2043750
400	10.2	92.88	5.08	0.24	3793750
450	10.6	92.59	5.33	0.23	2587500
500	9.5	93.35	5.50	0.26	3962500

Table A.8 Turbidity in lake water treated with FHMD changes with settling time and during settling period

Time, h	Period, h	Turbidity, NTU	Turbidity difference, NTU
0		311.00	
1	0.5	200.00	111.00
2	1.5	131.00	69.00
4	3	81.30	24.85
6	5	67.50	6.90
8	7	56.30	5.60
12	10	51.40	1.23
22	17	46.30	0.51
48	35	25.40	0.80
72	60	15.80	0.40
84	78	13.70	0.18
96	90	12.30	0.12
120	108	7.96	0.18
132	126	4.88	0.26
144	138	1.42	0.29

Table A.9 Turbidity in lake water treated with raw diatomite changes with settling time and during settling period

Time, h	Period, h	Turbidity, NTU	Turbidity difference, NTU
0		227.30	
1	0.5	135.70	91.60
2	1.5	106.50	29.20
4	3	65.90	20.30
6	5	48.20	8.85
8	7	36.70	5.75
12	10	25.20	2.88
22	17	16.50	0.87
48	35	9.65	0.26
72	60	7.27	0.099
84	78	5.98	0.11
96	90	4.69	0.11
120	108	4.13	0.023
132	126	2.85	0.11
144	138	1.11	0.15

Table A.10 Changes in SRP concentrations in lake water treated by FHMD during the period of 30-day incubation

Time, day	SRP, mg/L at 0 mg/L	SRP, mg/L at 300 mg/L	SRP, mg/L at 400mg/L	SRP, mg/L at 500 mg/L	SRP, mg/L at 600 mg/L
1	24.55	7.55	6.05	5.20	3.45
5	23.30	8.50	5.95	4.25	3.25
12	22.05	8.75	5.85	3.65	3.10
17	19.55	9.40	6.00	3.50	2.95
22	27.85	12.00	6.25	3.15	3.25
30	31.95	14.45	6.50	3.65	4.10

Table A.11 Changes in TP concentrations in lake water treated by FHMD during the period of 30-day incubation

Time, day	TP, μg/L at 0 mg/L	TP, μg/L at 300 mg/L	TP, μg/L at 400mg/L	TP, μg/L at 500 mg/L	TP, μg/L at 600 mg/L
1	78.85	17.05	14.30	11.15	10.25
5	87.60	16.35	13.20	10.55	9.90
12	95.70	18.10	11.80	9.90	9.70
17	100.60	18.40	11.65	9.45	9.25
22	99.80	19.30	10.85	9.25	8.65
30	101.50	26.90	10.10	8.80	8.45

Table A.12 Sedimentary phosphorus compositions of sediments treated by FHMD at different doses under anoxic conditions

FHMD dose	Labile-P, ug/gdw	Fe-P, ug/gdw	Al-P, ug/gdw	Organic-P, ug/gdw	Ca-P, ug/gdw	Residue-P, ug/gdw
0	8.36	7.73	8.58	20.37	404.57	46.1
0.3	4.21	19.79	7.71	16.48	389.40	45.60
0.4	2.99	25.62	11.13	16.78	411.47	50.16
0.5	3.02	33.47	10.64	16.68	367.65	48.60
0.6	2.69	28.53	11.17	16.98	425.38	45.38

Table A.13 Changes in SRP concentrations in lake water treated with 400 mg/L of FHMD and alum at different doses during the period of anoxic incubation

Time, day	Alum dose, 0 mg/L			Log(Al:P) = 0.5			Log(Al:P) = 0.8			Log(Al:P) = 1.1			Log(Al:P) = 1.4			Log(Al:P) = 1.7		
	SRP_1, μg/L	SRP_2, μg/L	SRP_{avg}, μg/L	SRP_1, μg/L	SRP_2, μg/L	SRP_{avg}, μg/L	SRP_1, μg/L	SRP_2, μg/L	SRP_{avg}, μg/L	SRP_1, μg/L	SRP_2, μg/L	SRP_{avg}, μg/L	SRP_1, μg/L	SRP_2, μg/L	SRP_{avg}, μg/L	SRP_1, μg/L	SRP_2, μg/L	SRP_{avg}, μg/L
1	6.2	6.8	6.5	7.7	7.1	7.4	6.8	5.8	6.3	7.4	6.0	6.7	7.4	8.0	7.7	6.4	7.4	6.9
5	5.9	5.5	5.7	6.5	5.5	6.0	5.7	6.5	6.1	6.2	7.0	6.6	6.4	5.8	6.1	5.8	4.8	5.3
12	4.7	4.3	4.5	4.0	4.2	4.1	6.0	5.0	5.5	2.9	3.5	3.2	3.2	3.8	3.5	3.4	3.0	3.2
22	4.8	4	4.4	3.6	3.8	3.7	2.9	3.7	3.3	2.4	2.8	2.6	3.1	2.1	2.6	2.0	2.2	2.1
30	2.1	2.3	2.2	2.1	2.5	2.3	2.1	2.3	2.2	1.4	1.6	1.5	1.9	1.5	1.7	1.4	1.6	1.5

Table A.14 Changes in TP concentrations in lake water treated with 400 mg/L of FHMD and alum at different doses during the period of anoxic incubation

Time, day	Alum dose, 0 mg/L			Log(Al:P) = 0.5			Log(Al:P) = 0.8			Log(Al:P) = 1.1			Log(Al:P) = 1.4			Log(Al:P) = 1.7		
	TP_1, μg/L	TP_2, μg/L	TP_{avg}, μg/L	TP_1, μg/L	TP_2, μg/L	TP_{avg}, μg/L	TP_1, μg/L	TP_2, μg/L	TP_{avg}, μg/L	TP_1, μg/L	TP_2, μg/L	TP_{avg}, μg/L	TP_1, μg/L	TP_2, μg/L	TP_{avg}, μg/L	TP_1, μg/L	TP_2, μg/L	TP_{avg}, μg/L
1	16.6	15.6	16.1	15.6	16.4	16.0	15.7	16.7	16.2	16.0	17.4	16.7	14.3	15.1	14.7	15.7	16.5	16.1
5	13.7	12.9	13.3	14.2	14.8	14.5	14.4	15.4	14.9	12.9	13.9	13.4	13.8	14.6	14.2	10.1	10.7	10.4
12	12.4	12.0	12.2	11.2	10.6	10.9	10.8	11.2	11.0	11.4	12.2	11.8	11.1	10.3	10.7	12.1	11.1	11.6
22	11.3	10.3	10.8	10.4	11.4	10.9	13.1	14.3	13.7	10.4	11.2	10.8	11.1	9.5	9.8	10.7	10.1	10.4
30	10.1	10.5	10.3	11.0	11.2	11.1	11.4	11.0	11.2	9.0	8.6	8.8	10.5	9.5	10.0	8.7	8.1	8.4

Table A.15 Sedimentary phosphorus compositions of sediments treated by 400 mg/L of FHMD and alum at different doses during the period of anoxic incubation

Log (Al:P)	Labile-P, ug/gdw	Fe-P, ug/gdw	Al-P, ug/gdw	Organic-P, ug/gdw	Ca-P, ug/gdw	Residue-P, ug/gdw
0	2.42	16.52	7.28	27.47	517.01	42.32
0.5	1.19	17.18	17.21	20.89	467.69	50.38
0.8	1.24	15.98	21.25	14.83	520.93	54.72
1.1	1.17	9.59	42.31	12.55	447.04	52.88
1.4	0.68	7.81	62.23	9.79	417.25	56.43
1.7	0.43	6.71	66.00	7.81	499.73	47.23

Table A.16 Effects of agitation on turbidity in lake water with different thickness of gypsum under anoxic conditions

Time, h \ Turbidity, NTU	Turbidity, NTU at 0 cm	Turbidity, NTU at 0.5 cm	Turbidity, NTU at 0.8 cm	Turbidity, NTU at 1 cm	Turbidity, NTU at 1.2 cm
0	9.55	11.70	11.50	11.65	12.40
6	12.80	10.40	10.70	9.82	11.50
12	11.35	9.70	10.19	9.27	10.72
21	10.23	9.24	9.43	8.03	9.35
24	9.90	8.58	8.54	8.18	8.59
30	9.66	7.27	7.12	7.09	7.11
36	10.70	6.29	6.35	6.31	6.09
48	7.73	5.13	5.09	5.45	5.00
54	1000	76.00	41.95	48.70	52.30
60	1000	85.30	46.20	53.70	55.10
69	10.90	3.93	3.14	3.76	3.97
72	7.44	3.37	2.65	2.98	2.86

Table A.17 Effects of agitation on turbidity in lake water with different thickness of gypsum under oxic conditions

Time, h \ Turbidity, NTU	Turbidity, NTU at 0 cm	Turbidity, NTU at 0.5 cm	Turbidity, NTU at 0.8 cm	Turbidity, NTU at 1 cm	Turbidity, NTU at 1.2 cm
0	9.23	7.09	7.93	8.24	8.68
6	7.50	5.77	6.48	6.13	7.79
12	6.63	4.60	5.12	4.74	6.14
21	5.98	4.17	4.56	4.15	5.17
24	5.44	3.92	4.34	4.01	4.95
30	4.82	3.56	3.70	3.55	4.33
36	4.09	2.89	2.95	2.94	3.73
45	3.55	2.67	2.59	2.62	3.18
48	3.32	2.55	2.38	2.28	2.74
54	1000	89.30	74.80	95.50	96.30
60	1000	95.80	84.10	104.30	102.60
69	8.79	2.87	2.68	2.51	2.96

Table A.18 Effects of agitation in SRP concentrations with different thickness of gypsum under anoxic conditions

Time, h \ SRP at Thickness, cm	SRP, mg/L at 0 cm	SRP, mg/L at 0.5 cm	SRP, mg/L at 0.8 cm	SRP, mg/L at 1 cm	SRP, mg/L at 1.2 cm
0	6.87	7.34	6.85	7.63	8.01
6	13.68	11.30	8.30	10.37	10.86
12	11.60	10.75	5.60	7.80	3.65
21	13.60	12.40	6.05	7.35	6.80
24	13.00	8.60	5.40	3.80	2.30
30	13.70	10.90	7.20	9.25	5.60
36	10.20	8.75	4.55	3.70	4.19
48	8.47	10.60	8.20	9.05	7.65
54	18.50	15.60	10.05	10.65	12.40
60	8.50	7.65	4.80	6.95	7.85
69	3.80	2.95	2.50	6.90	3.60
72	1.70	2.10	2.60	2.60	2.60

Table A.19 Effects of agitation in SRP concentrations with different thickness of gypsum under oxic conditions

Time, h \ SRP at Thickness, cm	SRP, mg/L at 0 cm	SRP, mg/L at 0.5 cm	SRP, mg/L at 0.8 cm	SRP, mg/L at 1 cm	SRP, mg/L at 1.2 cm
0	8.30	8.55	8.45	8.90	7.35
6	10.40	9.45	9.20	8.00	7.30
12	11.50	9.70	5.20	5.35	5.10
21	8.20	7.00	6.35	6.20	8.50
24	8.55	8.75	7.25	7.00	7.75
30	5.40	8.25	4.40	5.25	5.00
36	3.00	3.40	1.60	1.75	4.00
45	3.90	5.20	3.90	2.90	4.10
48	3.10	5.30	3.00	5.55	3.70
54	12.95	10.35	6.90	6.40	6.50
60	8.10	7.40	4.60	4.10	5.70
69	2.20	1.70	1.10	2.10	1.65

Table A.20 Changes in total phosphorus (TP) concentrations in lake water with the incubation time under anoxic conditions and oxic conditions

Time, days	TP, μg/L (anoxic)	Error Bar, μg/L	TP, μg/L (oxic)	Error Bar, μg/L
0	14.0	1.2	15.8	1.1
6	14.0	1.0	14.2	1.7
10	13.8	0.7	11.4	0.1
16	11.3	1.2	9.1	1.1
21	12.1	0.6	8. 5	1.0
30	10.8	0.1	9.5	0.8

Table A.21 Dissolved oxygen (DO) concentrations change with time in control aquarium and 120-day aquarium

Time, day	DO in control aquarium, mg/L	DO in 120-day aquarium, mg/L
0	7.40	7.60
4	5.78	6.11
8	3.17	5.39
12	2.10	3.42
16	1.42	2.37
20	1.24	1.31
24	1.02	1.16
28	0.93	1.00
32	0.84	0.89
36	0.80	0.85
40	0.82	0.87
44	0.73	0.79
48	0.75	0.78
52	0.71	0.76
56	0.69	0.73
60	0.70	0.71
64	0.66	0.75
68	0.63	0.73
72	0.64	0.76
76	0.67	0.70
80	0.64	0.66
84	0.61	0.65
88	0.60	0.64
92	0.58	0.60
96	0.59	0.62
100	0.55	0.57
104	0.58	0.62
108	0.59	0.59
112	0.54	0.56
116	0.51	0.55
120	0.50	0.54

Table A.22 Total suspended solid (TSS) concentrations change with time in control aquarium and 120-day aquarium

Time, day	TSS in control aquarium, mg/L	TSS in 120-day aquarium, mg/L
0	127	5
4	133	6
8	136	8
12	142	11
16	148	12
20	149	12
24	144	15
28	158	15
32	169	15
36	180	17
40	197	18
44	214	17
48	235	17
52	265	19
56	288	18
60	311	20
64	321	20
68	386	21
72	433	22
76	490	24
80	525	24
84	558	26
88	589	25
92	612	28
96	634	30
100	655	28
104	680	30
108	693	32
112	706	33
116	713	34
120	725	35

Table A.23 Dissolved sulfate (SO_4) concentrations change with time in control aquarium and 120-day aquarium

Time, day	SO_4 in control aquarium, mg/L	SO_4 in 120-day aquarium, mg/L
0	0.95	1.84
4	0.93	1.85
8	0.90	1.76
12	0.91	1.81
16	0.91	1.78
20	0.72	1.71
24	0.71	1.69
28	0.64	1.75
32	0.72	1.88
36	0.71	1.85
40	0.72	1.86
44	0.72	1.84
48	0.70	1.80
52	0.74	1.89
56	0.71	1.78
60	0.88	1.88
64	0.88	1.74
68	0.76	1.79
72	0.78	1.86
76	0.80	1.88
80	0.83	1.9
84	0.72	1.83
88	0.74	1.85
92	0.75	1.75
96	0.78	1.90
100	0.81	1.86
104	0.79	1.87
108	0.80	1.82
112	0.80	1.75
116	0.80	1.86
120	0.82	1.88

Table A.24 Total kjeldahl nitrogen (TKN) concentrations change with time in control aquarium and 120-day aquarium

Time, day	TKN in control aquarium, mg/L	TKN in 120-day aquarium, mg/L
0	1.90	2.58
4	1.95	2.84
8	2.99	3.26
12	2.37	2.63
16	2.11	2.27
20	1.69	4.09
24	2.16	1.80
28	1.87	2.40
32	2.60	2.45
36	2.60	2.55
40	2.55	2.60
44	2.40	2.71
48	2.14	2.76
52	2.66	3.18
56	2.50	2.86
60	1.93	2.19
64	2.24	2.03
68	1.82	1.87
72	1.93	2.66
76	1.87	2.14
80	1.87	1.72
84	2.32	2.37
88	3.26	3.10
92	2.11	2.32
96	2.27	2.42
100	2.16	2.11
104	2.47	2.11
108	2.42	2.27
112	2.27	2.37
116	2.37	2.37
120	2.47	2.47

Table A.25 Dissolved silicon (Si) concentrations change with time in control aquarium and 120-day aquarium

Time, day	Si in control aquarium, mg/L	Si in 120-day aquarium, mg/L
0	3.15	3.87
4	3.16	3.84
8	3.17	3.81
12	3.29	3.88
16	3.37	3.95
20	3.35	3.92
24	3.43	3.94
28	3.48	3.97
32	3.54	3.90
36	3.51	3.88
40	3.49	3.89
44	3.48	3.88
48	3.45	3.95
52	3.46	3.97
56	3.49	4.01
60	3.47	3.94
64	3.52	4.02
68	3.49	3.78
72	3.54	3.97
76	3.49	3.99
80	3.48	3.96
84	3.47	3.85
88	3.42	3.86
92	3.39	3.99
96	3.37	4.00
100	3.35	3.95
104	3.32	3.97
108	3.32	3.97
112	3.28	3.94
116	3.26	3.96
120	3.24	3.94

Table A.26 Diatom concentrations change with time in control aquarium and 120-day aquarium

Time, day	Diatom in control aquarium, cells/mL	Diatom in 120-day aquarium, cells/mL
0	231250	156250
4	225000	143750
8	193750	118750
12	181250	112500
16	156250	100000
20	137500	87500
24	125000	87500
28	131250	75000
32	112500	75000
36	100000	62500
40	81250	50000
44	93750	56250
48	75000	50000
52	75000	37500
56	68750	50000
60	75000	50000
64	68750	37500
68	68750	31250
72	68750	31250
76	56250	31250
80	56250	37500
84	50000	25000
88	56250	25000
92	50000	18750
96	43750	25000
100	43750	25000
104	37500	18750
108	31250	18750
112	37500	25000
116	31250	25000
120	31250	18750

Table A.27 Total alkalinity concentrations change with time in control aquarium and 120-day aquarium

Time, day	Alkalinity in control aquarium, $mgCaCO_3/L$	Alkalinity in 120-day aquarium, $mgCaCO_3/L$
0	214.40	344.72
4	227.01	345.77
8	246.98	340.51
12	254.34	342.62
16	264.84	344.72
20	272.20	342.62
24	290.07	339.46
28	308.99	343.67
32	254.34	345.77
36	276.41	344.72
40	295.32	342.62
44	317.39	345.77
48	330.01	344.72
52	308.99	343.67
56	296.37	344.72
60	285.86	344.72
64	302.68	347.87
68	316.34	345.77
72	291.12	342.62
76	286.92	343.67
80	293.22	344.72
84	300.58	339.46
88	265.90	344.72
92	286.92	345.77
96	271.15	347.87
100	264.84	344.72
104	241.72	345.77
108	244.88	342.62
112	234.37	341.57
116	228.06	344.72
120	214.40	343.67

Table A.28 pH values change with time in control aquarium and 120-day aquarium

Time, day	pH in control aquarium	pH in 120-day aquarium
0	8.11	8.60
4	8.10	8.55
8	8.13	8.55
12	8.16	8.55
16	8.18	8.55
20	8.13	8.51
24	8.18	8.51
28	8.12	8.52
32	8.15	8.67
36	8.14	8.61
40	8.15	8.61
44	8.15	8.55
48	8.10	8.52
52	8.12	8.56
56	8.11	8.55
60	8.11	8.54
64	8.13	8.55
68	8.15	8.56
72	8.17	8.61
76	8.15	8.62
80	8.13	8.62
84	8.25	8.58
88	8.22	8.55
92	8.21	8.61
96	8.16	8.61
100	8.15	8.61
104	8.18	8.62
108	8.20	8.57
112	8.17	8.60
116	8.18	8.62
120	8.18	8.61

Table A.29 Total phosphorus (TP) concentrations change with time in control aquarium and 120-day aquarium

Time, day	TP in control aquarium, μg/L	TP in 120-day aquarium, μg/L
0	73.3	9.6
4	81.1	9.5
8	67.6	9.3
12	73.4	9.5
16	76.4	9.6
20	79.4	9.7
24	84.8	9.3
28	88.5	10.0
32	90.4	9.8
36	94.3	9.6
40	99.6	9.4
44	102.7	9.3
48	110.8	9.1
52	107.4	10.1
56	110.0	10.1
60	113.2	10.2
64	114.8	10.7
68	113.6	11.1
72	117.6	12.5
76	120.4	12.1
80	124.4	12.0
84	124.0	11.7
88	126.1	11.9
92	125.0	11.6
96	129.3	12.0
100	130.4	13.3
104	133.4	12.5
108	131.7	12.2
112	136.0	12.4
116	138.5	12.6
120	139.2	12.9

Table A.30 Sedimentary phosphorus depth profile in control sediment

Depth, cm	Labile-P, ug/gdw	Fe-P, ug/gdw	Al-P, ug/gdw	Organic-P, ug/gdw	Ca-P, ug/gdw	Residue-P, ug/gdw
1	3.39	4.13	8.50	38.58	485.17	61.60
2	4.38	5.74	6.93	35.62	444.98	57.81
3	5.77	7.68	8.79	34.07	413.44	54.90
4	7.07	9.45	8.67	34.06	390.57	46.94

Table A.31 Sedimentary phosphorus depth profile in 60-day sediment

Depth, cm	Labile-P, ug/gdw	Fe-P, ug/gdw	Al-P, ug/gdw	Organic-P, ug/gdw	Ca-P, ug/gdw	Residue-P, ug/gdw
1	3.33	22.43	5.85	25.80	472.63	81.23
2	6.80	30.47	7.47	27.46	459.33	87.34
3	7.91	57.20	5.86	31.07	411.96	79.69
4	7.38	49.12	5.83	27.61	389.13	88.86

Table A.32 Sedimentary phosphorus depth profile in 120-day sediment

Depth, cm	Labile-P, ug/gdw	Fe-P, ug/gdw	Al-P, ug/gdw	Organic-P, ug/gdw	Ca-P, ug/gdw	Residue-P, ug/gdw
1	2.96	18.23	6.10	15.76	458.69	84.87
2	5.24	34.06	8.25	19.12	405.59	81.18
3	3.41	48.83	5.93	13.8	397.75	80.14
4	3.25	49.41	7.11	17.00	384.72	74.03